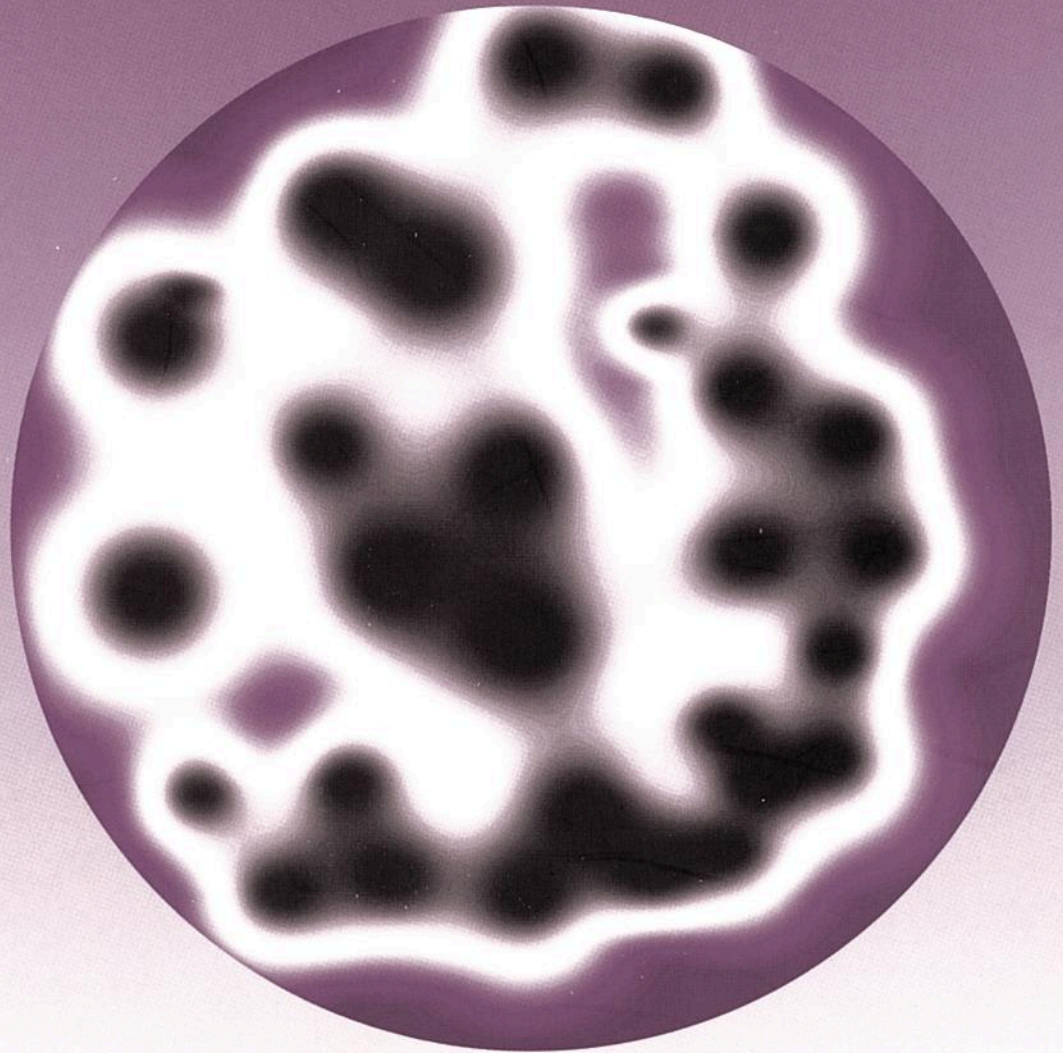


# Spatio-temporal pattern formation in a semiconductor-gas-discharge system



Danijela Šijačić

# Stellingen

bij het proefschrift

## Spatio-temporal pattern formation in a semiconductor-gas-discharge system

door

Danijela Šijačić

1. Recent textbooks focus on the subcritical transition from Townsend to glow discharge, i.e., on a falling current-voltage characteristics. However, in short gaps, the transition can also be supercritical or even show some intermediate mixed behavior.

[See Chapter 5 in this thesis.]

2. The current-voltage characteristics of a gas discharge is typically presented in a semi-log plot; and it is very interesting (but not at all true) that a load line in a semi-log plot stays just a line!

[See Fig. 1.2 in this thesis.]

3. The semiconductor-gas-discharge system exposed to a DC voltage can spontaneously attain a mode of temporal oscillations while staying spatially homogeneous and a bifurcation diagram for this transition can be calculated.

[See Chapters 3 and 6 in this thesis.]

4. Despite expectations based on simplified reaction-diffusion models, oscillations are possible even when the current-voltage characteristics has a positive differential conductivity.

5. By increasing one of the control parameters (e.g., applied voltage) the period of oscillations can double. Further increase of the voltage leads to the well known route to chaos through a cascade of period doubling events. This shows again that a simplification to a two-component reaction-diffusion model is not possible.

[For stellingen 4 and 5 see Chapter 7 in this thesis.]

6. Our system can make a transition from spatially homogeneous to spatially structured oscillating patterns on the mere increase of the width of the semiconductor layer while its resistance and capacitance stay unchanged.

[See Chapter 8 in this thesis.]

7. 'Justice for all' exists only in theory. The truth is that justice may exist only among equals. Should we call this justice?

8. Science is certainly capable of answering many questions. The question is how many scientists are asking the right questions!

9. Animals and nature are suffering from mankind. Also, people closest to nature are suffering. The solution might be to help those people first.

10. The mathematics of string theory requires at least 11 dimensions. Although we can experience only 4 out of 11, the others are said to be curled up, but our incapability to experience them doesn't necessarily mean that they are not developed. They might be as well wide open and very important, but we as 3D beings do not have the means to see, feel or explain them.

Inspired by the book of Brian Greene - 'The Elegant Universe'

11. When it comes to everyday relations and the matters of heart, scientific methods and concepts are pretty much inapplicable.

12. The cruel and severe conditions of life in regions of eternal ice make you respect and appreciate the miracle of life the most!

13. The ability to learn Dutch is closely related to the ability to cope with the pain felt when actually trying to speak it.

---

Spatio-temporal pattern formation in a  
semiconductor-gas-discharge system

---

Danijela Šijačić

Copyright © 2004 by Danijela Šijačić

Printed and bound by Ponsen & Looijen bv.

Cover design by Simona Orzan.

Picture on the cover is an artistic impression resembling some experimental observations.

CIP-DATA LIBRARY TECHNISCHE UNIVERSITEIT EINDHOVEN

Šijačić, Danijela

Spatio-temporal pattern formation in a semiconductor-gas-discharge system /  
by Danijela Šijačić.-

Eindhoven : Technische Universiteit Eindhoven, 2004. -

Proefschrift.

ISBN 90-386-2035-7

NUR 925

Trefwoorden : Townsend-ontladingen / patroonvorming /  
reactie-diffusievergelijkingen / bifurcatietheorie

Subject headings : Townsend discharges / Glow discharges / pattern  
formation / bifurcation diagrams / reaction-diffusion equations

# **Spatio-temporal pattern formation in a semiconductor-gas-discharge system**

PROEFSCHRIFT

ter verkrijging van de graad van doctor aan de  
Technische Universiteit Eindhoven, op gezag van de  
Rector Magnificus, prof.dr. R.A. van Santen, voor een  
commissie aangewezen door het College voor  
Promoties in het openbaar te verdedigen  
op donderdag 2 december 2004 om 16.00 uur

door

**Danijela Šijačić**

geboren te Novi Sad, Servië

Dit proefschrift is goedgekeurd door de promotoren:

prof.dr. U.M. Ebert  
en  
prof.dr.ir. W. van Saarloos

Copromotor:  
dr. W.H. Hundsdorfer

Het onderzoek dat tot dit proefschrift heeft geleid werd mede mogelijk  
gemaakt door Stichting voor Fundamenteel Onderzoek der Materie (FOM).

# Preface

This thesis is based on more than four years of research that I have carried out at the Center for Mathematics and Computer Science (CWI) in Amsterdam. So far, this research has resulted in four publications which served as a base for some of the chapters. However, these chapters are not meant to be read separately, since the thesis is made as one compact story with the model and its notation fixed in Chapter 4. The papers and corresponding chapters are listed as follows:

**Chapter 5** D.D. Šijačić and U. Ebert, *Transition from Townsend to glow discharge: Subcritical, mixed, or supercritical characteristics*, Phys. Rev. E **66**, 066410 (2002).

Yu.P. Raizer, U. Ebert and D.D. Šijačić, *Dependence of the transition from Townsend to glow discharge on secondary emission*, Phys. Rev. E **70**, 017401 (2004).

**Chapter 6** D.D. Šijačić, U. Ebert and I. Rafatov, *Oscillations in DC driven ‘barrier’ discharges: Numerical solutions, stability analysis and phase diagram*, submitted to Phys. Rev. E

**Chapter 7** D.D. Šijačić, U. Ebert and I. Rafatov, *Period doubling cascade in glow discharges: local versus global differential conductivity*, Phys. Rev. E **70** (2004) [to appear].

There are two more papers in preparation:

*Oscillations despite local and global positive differential conductivity* based on Subsection 7.4.1 and,

*Spatio-temporal patterns in DC driven ‘barrier’ discharges: Numerical solutions and stability analysis* based on Chapter 8.

Furthermore, this thesis has an extensive introduction which consists of three chapters. That seemed necessary since:

The problem comes from gas discharge physics (Chapter 1);

It is investigated by applying methods from nonlinear dynamics and pattern formation theory (Chapter 2);

Chapter 3 reviews particular experiments on whose explanation we focus in later chapters.



*O God, I could be bounded in a nutshell and count myself a King of infinite space.*

Hamlet, II, 2

*So far as theories of mathematics are about reality, they are not certain; So far as they are certain, they are not about reality.*

Albert Einstein

# Contents

<b>Preface</b>	<b>i</b>
<b>Introduction</b>	<b>1</b>
<b>1 Introduction to gas discharge physics</b>	<b>7</b>
1.1 Classification of discharges . . . . .	7
1.2 Current-voltage characteristics of DC discharge . . . . .	9
1.3 Townsend breakdown . . . . .	12
1.4 Production and loss of charges in a gas . . . . .	15
<b>2 A pattern formation primer</b>	<b>17</b>
2.1 General introduction . . . . .	17
2.2 Stability analysis and bifurcations . . . . .	18
<b>3 Experiments</b>	<b>23</b>
3.1 Experimental setup and parameters . . . . .	23
3.2 Overview over experimental results . . . . .	25
3.3 Homogeneous oscillations . . . . .	26
3.4 Spatial patterns . . . . .	31
3.A Appendix A . . . . .	32
<b>4 Derivation of the model</b>	<b>35</b>
4.1 Gas gap . . . . .	35
4.1.1 Boundary conditions . . . . .	37
4.2 Semiconductor layer . . . . .	37
4.2.1 1D reduction . . . . .	40
4.3 Complete model in dimensionless form . . . . .	41
4.3.1 1D representation of the full model . . . . .	43
<b>5 Stationary solutions</b>	<b>45</b>
5.1 Introduction . . . . .	45
5.2 The stationary problem . . . . .	48
5.2.1 A global conservation law . . . . .	49
5.3 Analytical small current expansion . . . . .	49
5.3.1 The Townsend limit . . . . .	49

5.3.2	The argument of Engel and Steenbeck . . . . .	50
5.3.3	A systematic expansion in small $j$ . . . . .	51
5.3.4	Discussion of the result . . . . .	54
5.4	Numerical solutions . . . . .	57
5.4.1	The numerical method . . . . .	57
5.4.2	Parameters $L$ , $\gamma$ and $\mu$ , and $j/\mu$ -scaling . . . . .	57
5.4.3	General features of the current-voltage-characteristics . . . . .	58
5.4.4	Spatial profiles . . . . .	60
5.4.5	Comparison of numerical and analytical results . . . . .	61
5.4.6	Corrections to $j/\mu$ -scaling . . . . .	61
5.4.7	Discussion of bifurcation structures . . . . .	62
5.5	Summary and Outlook . . . . .	66
5.A	Appendix A . . . . .	67
5.B	Appendix B . . . . .	68
<b>6</b>	<b>Oscillatory solutions</b> . . . . .	<b>69</b>
6.1	Numerical solutions of the dynamics . . . . .	70
6.1.1	Physical parameters . . . . .	70
6.1.2	Numerical solution strategy . . . . .	72
6.1.3	Qualitative features of experimental and numerical oscillations: Hysteresis and limit cycles . . . . .	73
6.1.4	Quantitative comparison: Amplitude and frequency of oscillations . . . . .	77
6.1.5	Mechanism of the oscillations, reaction-diffusion models and surface charge . . . . .	79
6.2	Stability analysis: Method . . . . .	80
6.2.1	Problem setting and stationary solutions . . . . .	80
6.2.2	Linear perturbations . . . . .	81
6.2.3	Rescaling with $\mu$ and numerical calculation . . . . .	83
6.3	Stability Analysis: Results . . . . .	83
6.3.1	The structure of the results . . . . .	84
6.3.2	Comparison with solutions of the full PDE's . . . . .	84
6.3.3	Calculation of phase diagrams . . . . .	86
6.4	Conclusion . . . . .	88
<b>7</b>	<b>Period doubling cascade and relation to reaction diffusion models</b> . . . . .	<b>89</b>
7.1	Introduction . . . . .	89
7.2	Predictions of a reaction-diffusion model . . . . .	90
7.3	A period doubling cascade . . . . .	93
7.4	Local versus global differential conductivity and the validity of a reaction-diffusion approximation . . . . .	94
7.4.1	Oscillations despite local and global positive differential conductivity . . . . .	96
7.5	A systematic model reduction . . . . .	98
7.5.1	Adiabatic elimination of the electrons . . . . .	99

---

7.5.2	Comparison with a two-component reaction-diffusion system . . . . .	101
7.5.3	Summary of the derivation . . . . .	102
<b>8</b>	<b>2D solutions: Spatio-temporal patterns</b>	<b>103</b>
8.1	Stability analysis . . . . .	104
8.1.1	Formulation of the problem . . . . .	104
8.1.2	Linear perturbation analysis for transversal Fourier modes	104
8.1.3	Formal solution and numerical implementation . . . . .	107
8.1.4	Results: dispersion relations . . . . .	110
8.2	2D computations: the numerical procedure . . . . .	115
8.2.1	Initial and boundary conditions . . . . .	115
8.2.2	The numerical procedure . . . . .	116
8.2.3	Testing the 2D program . . . . .	119
8.3	Preliminary results of the simulations . . . . .	120
8.3.1	Dependence on the numerical resolution . . . . .	120
8.3.2	A limitation of the numerical algorithm . . . . .	122
8.3.3	Analysis of numerical results and comparison with stability analysis . . . . .	123
8.3.4	Spatio-temporal patterns . . . . .	125
8.3.5	Outlook . . . . .	130
	<b>Bibliography</b>	<b>131</b>
	<b>Summary</b>	<b>137</b>
	<b>Samenvatting</b>	<b>141</b>
	<b>Rezime</b>	<b>145</b>
	<b>Acknowledgments</b>	<b>149</b>



# Introduction

## A survey

We encounter nonequilibrium plasmas in traditional neon tubes, in modern plasma screens as well as in sparks or lightning — to name only a few of these natural or technical phenomena. In contrast to plasma in stars or fusion, in all these cases the plasmas are formed not thermally; In such low temperature plasmas the ionization is generated by strong electrical or electromagnetic fields. Therefore they carry currents and are far from equilibrium like for example liquid crystals in electric fields. In applications, such nonequilibrium plasmas are typically tamed, i.e., they have a homogeneous and stationary, controllable behavior. Looking at natural processes, it is clear that this is nontrivial: most natural processes do form complex spatial and temporal structures. This is generic for nonlinear nonequilibrium systems.

This thesis is concerned with such pattern forming processes in a nonequilibrium plasma system that is as simple as possible, and therefore generic: two thin parallel layers are sandwiched between planar electrodes to which a DC voltage is applied, see Fig. 3.1. One layer is a semiconductor layer with high linear resistivity, the other layer is a simple gas like pure nitrogen or pure argon in which a discharge takes place. The discharge is the nonlinear element of the setup: it acts in the transition region between the Townsend regime where the interaction of charged and ionized particles in the gas is negligible, and the glow regime where space charge effects make the process nonlinear.

The spatially homogeneous two-layer system with stationary DC drive can spontaneously form a variety of spatial, temporal and spatio-temporal structures depending on the parameters of operation. The aim of this thesis is to understand these patterns by applying concepts from pattern formation and nonlinear analysis.

So far, two basically different theoretical approaches have been developed:

1. On the one hand, one can try to catch all specific properties of a particular system and solve it numerically. The result is a specific answer for this particular system, but
  - (i) the result can depend on numerical solution strategies, so either some physical understanding or very careful numerical testing is required to be sure of the results,

- (ii) typically, one will not investigate many different parameter sets, therefore it is difficult to say whether the observed results are generic.  
 (iii) Numerical solutions only give limited insight into the physical mechanisms underlying the observed phenomena.

2. On the other hand, one can have a completely different approach guided by the patterns observed in other physical systems. Since very different systems can form similar patterns, researchers have searched for a general principle to explain the phenomenon. For example, the hydrodynamic Rayleigh-Benard-convection, the chemical Belousov-Zhabotinsky-reaction, the migration pattern of Dictyostelium cells, the excitation waves of nervous tissue and our gas discharge system all can form rotating spiral waves. It is well known that a reaction-diffusion model with two components in two spatial dimensions can exhibit this and many other observed patterns, and indeed in many of the above examples, it is a valid way to describe system. It therefore, has been proposed by a number of researchers that reaction-diffusion models might be a valid approximation for the gas discharge system as well. Hence, the following questions arise:

- (i) Can such a model actually be derived from the underlying gas discharge physics?  
 (ii) Can this approach actually lead to specific predictions for phase diagrams of spatio-temporal structures formed in the gas discharge system?

In this thesis, an intermediate approach is chosen:

- An explicit gas discharge model is investigated, but it is a minimal one, i.e., it has as few parameters and mechanisms as possible. This model has been described by many previous authors and textbooks.
- New results for the stationary, temporal and spatio-temporal solutions of this classical model are derived
  - by full numerical solution and also
  - by stability analysis which allows the derivation of phase diagrams.
 A comparison of both approaches with each other and with experiments is performed.
- On the conceptual side, it is discussed
  - whether a two-component-reaction-diffusion model can be derived from the gas discharge model, and
  - whether negative differential conductivity (or equivalently a falling current-voltage-characteristics) is necessary for pattern formation.
 The thesis shows that the answer to both questions is negative.

## Organization of the thesis

Chapter 1 contains an introduction to gas discharge physics. Relevant processes of creation (and annihilation) of charges are discussed as an illustration for the possible complexity of discharges. Out of this variety, our model takes only two essential processes into account, namely ionization processes by electron impact in the bulk of the gas and secondary ionization by ion impact on the cathode. Also the whole current-voltage characteristics from Townsend through glow up to arc discharge is discussed whereas we later only need the regime between Townsend and glow discharge.

In Chapter 2, a few examples of pattern forming systems are given. In comparison with other systems, our gas discharge system has the advantage of particular convenient experimental handling and time scales. Furthermore, a few concepts and methods are explained that will be used later in the thesis. These include dimensional analysis and adiabatic elimination. Different bifurcation structures are classified and related to the observed patterns. Linear stability analysis is discussed in detail.

In Chapter 3, the specific experimental system is reviewed. In general, gas discharges on the transition from Townsend to glow regime exhibit a wealth of spatio-temporal structures. Long discharge columns [1–3] can form striations, i.e., spatial structures along the current direction. Short discharges with wide lateral aspect ratio, on the other hand, can exhibit rich spatio-temporal structures in the transversal direction as reported by a number of authors [4–10]. This is even the case when the externally applied voltage is stationary and the gas is pure, as long as the system is sandwiched between planar electrodes and at least one Ohmic layer. An interesting sequence of experiments has been performed in Münster [11, 12] where the bifurcations between different spatio-temporal states in parameter space were investigated very systematically. Their theoretical understanding is the main subject of the thesis.

Chapter 4 can be considered as an introductory chapter as well, since it introduces the simple classical model that is subsequently used to describe the experiments from Chapter 3. Based on the processes and mechanisms explained in Chapter 1 and introducing a number of assumptions and simplifications, the minimal model is derived. In the gas discharge, two ionization mechanisms cooperate to maintain conductivity: the so-called  $\alpha$  process of impact ionization in the bulk of the discharge, and the  $\gamma$  process of secondary emission at the cathode. The classical ‘fluid’ approximation consists of continuity equations for electron density and positive ion density, coupled to the Poisson equation for the electric field. Substantial densities of charged particles change the electric field according to the Poisson equation; in turn the electric field determines drift and ionization rates of the particles. Therefore the process is nonlinear as soon as space charges become relevant. It causes the transition from the linear Townsend discharge to the nonlinear glow discharge.

The transition from Townsend to glow discharge with growing current density is discussed in Chapter 5. The one-dimensional stationary solutions are derived in complete parameter space with numerical and analytical means. In



contrast to the textbook case of a subcritical bifurcation as shown in Chapter 1, this transition can also be supercritical or even exhibit some unexpected ‘mixed’ behavior for sufficiently short discharge gaps. This means that at the transition from Townsend to glow discharge, the voltage does not necessarily decrease with an increase of the current density. According to many authors [13–19], a negative differential conductivity of the current-voltage-characteristics is expected to play a central role in the spontaneous formation of patterns, quite like in nonlinear semiconductor devices [20]. Therefore, the observation that the characteristics can have a positive differential conductivity through the whole transition, is quite important. However, in Chapter 7 it will be shown that the differential conductivity does not play such a decisive role, in contrast to the claims above.

After solving the one-dimensional stationary solutions, in Chapter 6 the one-dimensional time-dependent problem including the semiconductor layer is considered. In fact, due to the lateral homogeneity of the experimental discharge in some parameter regime, this one-dimensional approximation is very good. The investigation serves two purposes: first, understanding the temporal structures is a first systematic step towards understanding the full spatio-temporal structures; second, there are numerous observations of temporal oscillations in comparable parameter regimes [16–18, 21–25]. Indeed, for the oscillations, the setup need not contain an Ohmic layer as in [11, 12], a serial resistor with capacitance in the circuit will have the same effect on the gas discharge. The qualitative and quantitative results of numerical solutions and experiments are discussed and compared. In particular, the hysteresis between stationary and oscillating solutions observed in experiments is demonstrated numerically, amplitude and frequency of the limit cycle oscillations as a function of applied voltage and conductivity of the semiconductor are compared with experimental results, and the physical mechanism of the oscillation is discussed. Furthermore, a stability analysis about a stationary solution of the complete system is performed. First a convincing agreement between numerical solutions of the full PDE’s and these stability analysis results is found. Then the stability analysis is used to calculate bifurcation diagrams for the transition from stationary to oscillating states which are then compared with the experiment.

Chapter 7 continues the investigation of one-dimensional time-dependent solutions, but with a different focus. Rather than predicting experiments, here model reductions are examined that were suggested previously. We concentrate on the question whether a simple two-component reaction-diffusion model for current and voltage in the gas discharge layer [5, 9, 15, 18, 19, 22, 26–28] is sufficient to describe the oscillations. Such a model is suggested through similarities with patterns formed in a number of physical, chemical or biological systems as already stated in the survey above. However, the actual results of a realistic gas discharge model are in conflict with a simple two-component reaction diffusion approximation that neglects the height and subsequent memory of the system. This can be seen, in particular, from the occurrence of a period doubling cascade of the oscillations. Furthermore, a reduced analytical model is derived systematically by adiabatic elimination of the electron dynamics. It does not

have the form of a reaction-diffusion-model. Finally, the concept of negative differential conductivity as a driving force for pattern formation is investigated. We actually find a counterexample where positive differential conductivity of the discharge coexists with a linear instability of the stationary solution. This unstable mode eventually evolves into a limit cycle.

Finally, in Chapter 8, spatio-temporal structures are analyzed. The computations are extended by one transversal direction which allows the general study of linear perturbations of the stationary state. These perturbations are studied in computations as well as through stability analysis. Stability analysis shows that spatial modes with non-vanishing wave number can have the fastest positive growth rate; these modes always are temporally oscillating. In such a parameter regime, spatially structured, oscillating patterns will form. Such patterns are indeed observed in the corresponding experiments, however, with a larger wave number than in our theory. This question is unresolved. Furthermore, the computations are extended into the nonlinear regime and show phenomena such as the approach to a limit cycle of spatially structured patterns.



# Chapter 1

## Introduction to gas discharge physics

Historically, the term gas discharge refers to the discharge of a plate capacitor through the air gap. Generally, air is a rather good insulator but if the electric field in the gap is high enough, the gas becomes ionized and short-circuits the capacitor gap. Nowadays, any current flow through ionized gas is called ‘gas discharge’. The ionized gas is usually luminous, therefore expressions like ‘the discharge ignites’ or ‘burns’ are very often in use. Electric discharges can create a low temperature plasma locally. In contrast to high temperature plasmas as in stars or fusion reactors that exist due to heating and magnetic confinement, low temperature plasmas exist under nonequilibrium conditions, e.g., due to an externally applied electric field. They generically are inhomogeneous in space and time and form a variety of a spatio-temporal patterns.

Gas discharge (plasma) physics is a wilderness. Nevertheless, we made an attempt to classify discharges using (and introducing) the terminology typical for this field. As a next step of this introductory chapter, we concentrate on a DC driven gas discharge explaining its current-voltage characteristics and different discharge modes. Furthermore, we discuss the mechanism of the Townsend breakdown in general form to illustrate how two ionization mechanisms together can create a stationary discharge. These two mechanisms also underlie the experiments discussed in Chapter 3. Finally at the end of this chapter, an overview of the microscopic processes responsible for the generation and annihilation of charge carriers is presented. The accent is put only on the processes which we actually use in our modeling of the experiments.

### 1.1 Classification of discharges

Gas discharge physics is an interesting and very complex field with a huge amount of experimental data and theoretical models. There is a variety of known discharge types. Among the parameters characterizing the gas discharge

are the gas type, its pressure and temperature, spatial dimensions and the shape of the discharge region, presence and composition of electrodes and boundaries, and the kind of energy supply. Internally, a gas discharge is characterized by the electric field and its homogeneity, the ionization rate, energy distribution of particles, spatial distribution of charge carriers, and dominant processes in the plasma. The variety of discharge properties makes a complete and strict classification of gas discharges on the basis of one or two parameters impossible. Though, multiple classifications based on specific points of view coexist. First of all, a discharge can be classified according to its temporal characteristics (steady or transient) and dominant processes like space charge effects or heating. The glow discharge is an example of a stationary type where space charge effects are essential (while in a Townsend discharge they can be neglected). If heating starts to play a dominant role, the stationary discharge that will develop is an arc and the transient is lightning.

The dominant mechanism of electron reproduction can also characterize the discharge. One can distinguish between either an external ionization source for a non-self-sustaining discharge or gamma and alpha modes for a self-sustaining discharge.

On the other hand, the frequency range of the applied fields can serve as a classification:

- DC, low-frequency, and pulsed fields (excluding very short pulses)
- radio-frequency fields ( $f \sim 10^5 - 10^8 \text{ Hz}$ )
- microwave fields ( $f \sim 10^9 - 10^{11} \text{ Hz}$ )
- optical fields.

We have seen that the frequency of the externally imposed electric field can be varied over a huge range giving rise to (pulsed) DC, AC, capacitively coupled plasmas (CCP), inductively coupled plasmas (ICP), plasmas induced by micro waves (MIPs) and (laser) light produced plasmas (LIP). Basically all technological plasmas (gas discharges) are created by an electric field which primarily affects the electrons resulting in different charge and currents distributions. By increasing the frequency of the applied electric field the role of the electrodes is reduced since the electrons are basically bounced forward and backward, not having the time to enter a (electrode) wall. In this thesis we focus on a DC situation, thus we are devoted to phenomena where electrodes play an important role. It is always instructive to start with a DC treatment, since space charge-, glow- and arc-like conditions can be found in ICP, MIP etc. as well.

## 1.2 Current-voltage characteristics of DC discharge

DC discharges are commonly classified on the basis of the current-voltage characteristic of the gas discharge of which a typical example is given in Fig. 1.2. The presented situation corresponds to a discharge in a long tube at relatively low values of the pressure. The tube can be filled with various gases. Two metal electrodes are inserted at the ends of the tube and connected to DC power supply via a series resistor as can be seen in Fig. 1.1. This is classical experimental setup which serves well to study many different types of discharges.

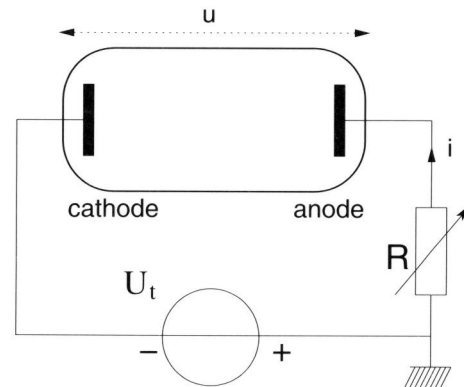


Figure 1.1: Classical experimental setup for the investigation of different modes of a DC discharge.

The steady state of the discharge is defined as the crossing point of the current-voltage characteristics and the load line of the external circuit, which consist of a power supply and a resistor in series. Depending on the applied voltage  $U_t$  and the resistance  $R$ , the load line can intersect the current-voltage characteristic in different regimes therefore defining which mode of the discharge will develop. In this thesis, we will operate in the regime of Townsend to glow discharge and corresponding current-voltage characteristics can have different shape than the one presented here (Fig. 1.2), as will be discussed later in Chapter 5.

### Non-self-sustaining discharge

If the applied voltage is below the breakdown threshold, no visible effects are produced though a very small current can be measured. The gas is practically an insulator and current is carried by charged particles which are always present due to cosmic rays or other ionizing agents (like the natural radioactivity). This discharge is not self-sustaining which means that it would extinguish if all ionizing agents were removed. Non-self-sustaining discharge corresponds to the

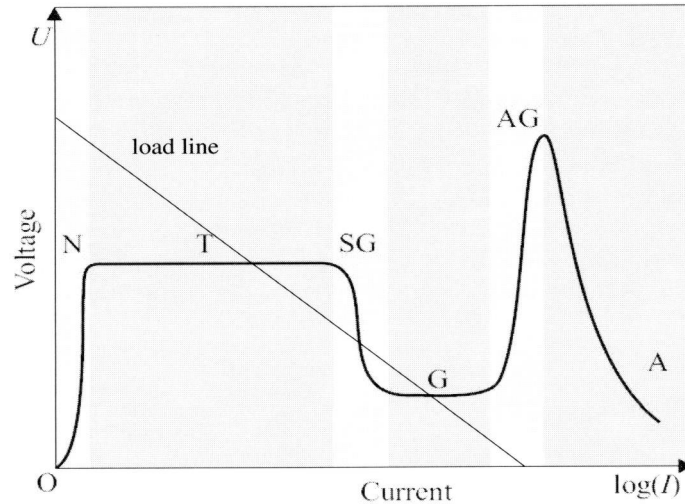


Figure 1.2: A semi-log plot of a gas discharge current-voltage characteristics. Different discharge modes are marked with gray vertical bands and denoted with abbreviations: N for Non-self-sustaining discharge; T for Townsend discharge; SG, G, and AG for Subnormal glow discharge, Glow discharge, and Abnormal glow discharge, respectively; A for Arc discharge. Load line defines the operating mode studied in this thesis. (This figure follows the style of [11, 12, 29], but should be considered only as an instructive artist's impression. For details, see 'Stellingen').

region at the very beginning, of extremely steep voltage growth in the current range denoted as N in Fig. 1.2. One can see that the current density saturates quickly while the voltage increases. Saturation corresponds to the situation where all electrons and ions generated in the gas volume are collected by the electrodes, therefore the current is limited by the rate of ionization.

### Townsend discharge

With further increase of the voltage, after the threshold of simple charge reproduction (1.2) is reached, stationary state of gas discharge is broken and the current grows exponentially several orders of magnitude at nearly constant voltage. The limiting factor for this growth is the resistance of the external circuit. If the external impedance is high enough, the load line of the external circuit crosses the current-voltage characteristics in region T (Fig. 1.2). This discharge regime is known as the Townsend discharge. Avalanches develop in the entire volume of the gas and leave behind traces with positive ions which drift slowly due to a low mobility, towards the cathode. Electrons have a high mobility and

move very fast to the anode. Thus, non-compensated positive space charge is formed in the gas volume. However, the current in Townsend discharge is so small that the space charge is negligible and does not distort the electric field in the gap. The Townsend discharge, also called dark discharge, is characterized by a weak luminosity and a low ionization rate of the gas.

### **Glow discharge**

Increasing the external voltage or reducing the load resistance, the current increase and the crossing point can be located in the region of glow discharge G (Fig. 1.2). The charge density in glow discharge is substantially higher than in Townsend discharge and the field of space charge cannot be neglected. The electric field distribution along the gas gap is strongly inhomogeneous and the discharge may have a complex longitudinal structure.

Due to higher current than in the Townsend mode, the positive space charge becomes larger. It partially screens the cathode so that the field near the cathode becomes stronger and that far from the cathode weaker than in the case of a homogeneous breakdown field. The drop of avalanche amplification in the rest of the gas gap behind the cathode region is easily compensated by amplification growth in the cathode region of the strong field. In the steady state, the field is concentrated near the cathode and avalanches develop there. In the rest of the gap between the electrodes the field is very weak and practically no ionization occurs. The electrons born in avalanches near the cathode drift slowly through this region gradually gaining energy from the field and exciting the neutral particles of gas. Due to the glow of excited atoms, the discharge is referred to as a 'glow discharge'. The existence of the cathode layer with a strong field, where the charge multiplication and reproduction, necessary for self-sustaining discharge occurs, is the essential attribute of a glow discharge.

The region of constant weak electric field is referred to as the positive column. There, electrons with a low mean energy are drifting slowly to the anode. However, some of them have a high energy and they are responsible for the ionization in the column, which compensates the electron losses. Weak luminosity of the positive column is produced by a small amount of these highly energetic electrons, which are present in the electron energy spectrum. Sometimes, the emitted light is not homogeneous, but has a periodic layered structure composed of striations [1–3, 29]. The positive column may have a different length and becomes shorter or disappears completely if the electrodes are shifted towards each other.

The efficiency of ionization depends strongly on the electric field. The field concentration near the cathode can make the ionization so effective that the total voltage (including the voltage drop on the positive column) required for a self-sustaining glow discharge can be lower than that for Townsend discharge with a homogeneous field and ionization in the entire gas volume. This explains the falling of the current-voltage characteristic by the transition from Townsend to the glow discharge (Fig. 1.2). However, in some other range of parameters (much smaller  $pd$  for instance), transition from Townsend to glow discharge has



monotonically increasing current-voltage characteristics. In Chapter 5, we show that this transition can have some intermediate, nonmonotonical form to which we refer as to ‘mix<sub>I</sub>’ or ‘mix<sub>II</sub>’ depending on whether the ‘glow’ voltage is lower or higher to the Townsend breakdown voltage.

The current range of glow discharge can be orders of magnitude wide, whereas the required voltage remains nearly constant. The remarkable property of glow discharge to keep a so-called ‘normal’ current density is responsible for this adaptivity. As the discharge current varies, the normal current density at the cathode is preserved and the occupied area at the cathode is changed. If the current is decreased (for instance, by an increased ohmic load in series with gas), the current spot at the cathode contracts until its size becomes comparable with the thickness of the cathode layer. The electron losses from the current channel become larger, and a higher voltage is necessary to support the discharge: the subnormal glow discharge (region SG in Fig. 1.2) takes place.

If the current of a normal glow discharge keeps growing, the entire cathode area will be covered with the discharge of the normal current density. This is a 3D explanation for a plateau in the normal glow discharge region, which is naturally missing in our 1D investigation of the current-voltage characteristics performed in Chapter 5. Further increase of the current by increasing the voltage results in the growing of the current density. This is the transition to abnormal glow discharge (region AG in Fig. 1.2).

### Transition to arc discharge

In the abnormal glow discharge, the required voltage grows rapidly with the current density, and becomes high enough to produce substantial heating of the cathode. The thermionic emission from the cathode grows, resulting in more electron avalanches. This leads to a higher density of charge carriers, i.e., to lower resistance, and, consequently to higher currents. When the current reaches approximately a value of 1 A glow discharge cascades down to an arc discharge. The current-voltage characteristics falls (see the region A in Fig. 1.1) and the arc needs only tens of volts for support. The arc releases large thermal power and can destroy the glass tube.

Since this thesis focus on the transition from Townsend to glow discharge, the arc discharge is not discussed further.

## 1.3 Townsend breakdown

The primary element of the often very complicated breakdown process is the electron avalanche, which develops in gas when an electric field of sufficient strength is applied. An avalanche begins with a small number of seed electrons that appear accidentally, e.g., due to cosmic rays. An electron picks up energy in the electric field. Having reached an energy higher than the ionization potential, the electron ionizes an atom or a molecule, thereby losing its energy. The two slow electrons resulting from this process are in turn accelerated in the field

and ionize two atoms or molecules. Thus, an exponential growth of the number of electrons and ions takes place. The breakdown is essentially a threshold process. It occurs only when the field exceeds a certain critical value. By a gradual increase of the field under the threshold value, no noticeable changes in the state of the gas can be observed. By reaching the breakdown field, ionization rises dramatically, a current through the gas can be detected, and a light emission can be seen. Such a behavior is a consequence of the steep dependence of the rate of atomic ionization by electron impact on the field strength. But, on the other side, avalanche is slowed down by electron energy losses and by the loss of electrons themselves. Electrons lose energy to excite electron states of atoms and molecules, and molecular vibration and rotation. Electrons also lose energy in the electric field if they move against the drift direction after elastic collisions. These will lead to an obstruction of the accumulation of electron energy. Diffusion leads to the removal of electrons from the field (e.g., precipitation on the walls), attachment in electronegative gases leads to direct electron losses, and the drift of electrons to the anode also removes them from the discharge. Because of the low electron density, the recombination rate at this stage is low as well, and practically does not contribute in the removal of electrons. The electron losses are breaking chains in the multiplication chain reaction. The breakdown threshold is determined by the relation between creation and removal of electrons. The electronic current at the anode can be calculated as an exponentially amplified electronic current at the cathode:

$$i_{1a} = i_{0c} e^{\alpha d} ,$$

where  $\alpha$  is Townsend's ionization coefficient,  $d$  the distance between electrodes and  $i_{0c}$  the electron current at the cathode. The first Townsend coefficient  $\alpha$  describes the multiplication rate and represents the number of ionization events performed by an electron in a 1 cm path along the field. It can be defined as a function of the reduced field ( $E/N$ ) or, in the case of a constant temperature, ( $E/p$ ), where  $E$  is the electric field,  $N$  is the concentration of neutral gas particles, and  $p$  is the pressure. Strictly speaking, the first Townsend coefficient depends on the mean energy of the electrons, and not on the electric field. However, for a field with small gradients, i.e., for a field which can be considered as constant on the mean ionization length of electrons, the assumption  $\alpha = f(E/N)$  is valid.

Electron avalanche leaves behind positive ions, which drift slowly to the cathode. The ion current at the cathode includes all ions generated in the avalanche:

$$i_c = i_{1a} - i_{0c} = i_{0c}(e^{\alpha d} - 1) .$$

This is the primary process in the volume of the discharge. The secondary process is the generation of secondary electrons at the cathode with the help of the particles generated in the primary gas ionization process. Especially important is the generation of secondary electrons by ion bombardment of the cathode.

The ratio of the emitted electrons and impacting ions is called  $\gamma$  - the secondary emission coefficient.

The secondary electrons are then multiplied in the gas gap and the electron current at the anode is

$$i_{2a} = \gamma i_c e^{\alpha d} = \gamma (e^{\alpha d} - 1) \cdot i_{0c} e^{\alpha d} .$$

Each electron avalanche is amplified by the factor

$$b = \frac{i_{2a}}{i_{1a}} = \gamma (e^{\alpha d} - 1) .$$

The stationary current is then determined by the limit of geometric progression:

$$i = \frac{i_{0c} e^{\alpha d}}{1 - \gamma (e^{\alpha d} - 1)} . \quad (1.1)$$

An equation of this type was first derived by Townsend in 1902. For a non-self-sustaining current, the denominator in (1.1) is positive and less than one.

With a voltage increase,  $\alpha$  grows until the denominator in (1.1) becomes equal to zero and then negative. The current cannot be stationary at this point and the formula becomes meaningless.

In the case of  $\gamma (e^{\alpha d} - 1) > 1$ , the number of secondary electrons is larger than that of primary electrons. The exponential growth of their number is then guaranteed. The external source of electrons is no longer necessary and the discharge becomes self-sustaining.

The condition for initiating a self-sustaining discharge

$$\gamma (e^{\alpha d} - 1) = 1 \quad \text{or} \quad \alpha d = \ln(1/\gamma + 1) , \quad (1.2)$$

describes the simple reproduction of electrons. The transition of non-self-sustaining to self-sustaining discharge can be interpreted as the onset of breakdown. The threshold voltage  $U_b$ , which corresponds to the condition of a steady self-sustained current in the homogeneous field  $E_b = U_b/d$  (1.2), is considered as the breakdown voltage. The so-called 'ignition condition' (1.2) will be derived in a stricter way in Chapter 5. Breakdown voltage  $U_b$  (and corresponding breakdown field  $E_b$ ) depends on the gas type, the pressure, the width of the discharge gap and the material of the cathode. Explicit expressions are [29]:

$$U_b = \frac{B (pd)}{C + \ln pd}, \quad \frac{E_b}{p} = \frac{B}{C + \ln pd}, \quad C = \ln \frac{A}{\ln(1/\gamma + 1)} . \quad (1.3)$$

derived by inserting the Townsend approximation  $\alpha(E) = Ap \exp(-Bp/|E|)$  into the ignition condition (1.2). The breakdown voltage, calculated in that way, with an experimentally determined constants  $A$  and  $B$  [29] Table 4.1, usually gives a satisfactory agreement with the experiment.

Experimental curves expressing the dependence of the breakdown voltage on discharge system parameters as gas pressure and the distance between the electrodes, are called **Paschen curves**. The curves have a clear minimum

which means that a minimal breakdown voltage for the discharge gap exists. According to (1.3), the parameters of this minimum point are:

$$(pd)_{min} = \frac{\bar{e}}{A} \ln(1/\gamma + 1), \quad \left(\frac{E}{p}\right)_{min} = B, \quad (U)_{min} = \frac{\bar{e}B}{A} \ln(1/\gamma + 1). \quad (1.4)$$

where  $\bar{e} = 2.72$  is the base of Natural logarithm. These expressions together with the experimental Paschen curves, can be used for the estimation of the secondary emission coefficient (see Appendix of Chapter 3), since only the value of  $(\frac{E}{p})_{min}$  does not depend on the cathode material. That value corresponds to the point (Stoletov's) where ionization capabilities of electrons are at a maximum.

At the left-hand branch and right-hand branch of the Paschen curve different physics is taking place. At the left-hand side, the steep increase of the breakdown voltage towards lower  $pd$  values corresponds to the transition to vacuum breakdown. Electrons there experience fewer collisions on their way to the anode and the ionization efficiency  $\alpha$  has to be very high, i.e., a high electric field is necessary to maintain the process. To the right of the minimum, the breakdown voltage grows as well. In this case electrons have many collisions but their ionization efficiency is low due to either a lower electric field (if the distance between electrodes  $d$  becomes larger) or a shorter mean free path (if the gas pressure  $p$  becomes higher). This similarity law is valid for a rather broad range of pressure and distance between the electrodes.

Strictly speaking, the voltage necessary for the breakdown should be slightly higher than  $U_b$  in order to ensure the expanded reproduction of electrons. The current and ionization in the gas will then increase until the growth is stopped by recombination or the ohmic resistance of the circuit. As the current increases, the resistance accepts a progressively greater part of the supply voltage, the voltage on the electrodes decreases until it reaches  $U_b$  and the current becomes stationary. The characteristic retardation time of the breakdown is on the order of  $10^{-5} - 10^{-3}$  s [29]. It consists of the statistical time of waiting for a seed electron and of the breakdown development time, which depends on both the electron multiplication rate and the characteristic time between two consequent generations of secondary electrons.

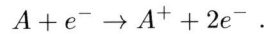
Multiple avalanches may develop simultaneously and each avalanche spreads transversally due to electron diffusion, so that new avalanches can start at different spots of the cathode. As a result, the Townsend breakdown most often involves the entire volume of the gap in a diffuse manner. This is the clear difference from the other breakdown mechanisms.

## 1.4 Production and loss of charges in a gas

There are two different categories of elementary discharge processes, namely volume processes and wall processes. To the volume processes where new charge carriers are generated, belong direct electron impact ionization, photoionization, Penning ionization (important in a gas mixture) and associative ionization (important in the inert gases). Volume processes where the number of free

electrons decrease are attachment and recombination. The excitation process also belongs to volume processes but it does not change the number of charged particles directly, but slows down the electrons. An excitation process occurs if the electron energy is big enough to bring the atom into an excited state. The excited atom may later participate in ionization processes or undergo a transition to the ground state with emission of a photon which is usually the reason of discharge glow.

In the atomic gases, the most important **volume process** is the ionization by electron impact. In the simplest case, it occurs if the electron has obtained from an electric field more energy than necessary to ionize the neutral atom and can be described by the formula



Attachment of an electron to a neutral atom or molecule leads to a generation of negative ions. This process plays an important role in electronegative gases, such as  $O_2$ ,  $Cl_2$ , and  $SF_6$ . It decreases the concentration of electrons and thus influences the development of avalanches. Negative ions have very low mobility and practically do not take part in excitation or ionization processes. This leads macroscopically to a higher breakdown field, therefore these gases are often used as insulators. Discharge is very sensitive to this process and even a small amount of oxygen or water vapor in the discharge gap leads to a strong increase of the breakdown voltage.

The most important **wall processes** are the removal of charge carriers from the gas volume and the generation of secondary charge carriers.

For the generation of secondary charge carriers, electron emission from wall (electrode) surfaces is important and there is a large variety of electron emission mechanisms which will not be discussed. Secondary electrons can also be emitted under the influence of various particles: Positive ions, excited atoms, electrons, and photons [30]. Secondary emission from a cold cathode produces breakdown of the discharge gap and also sustains a small DC current that is incapable of substantial heating of the cathode or of creating such a strong field at the cathode that thermionic or field emission develops. The most important secondary emission process is the ion-electron emission. It is characterized by the second Townsend coefficient  $\gamma_i$ : The number of secondary electrons emitted per incident positive ion. The kinetic energy of ions is practically the same as that of neutral particles (on the order of  $10^{-3}$  eV) and is insufficient to knock out an electron. The energy necessary for an electron to escape is obtained by the neutralization of the ion. The electric field of an ion on a distance comparable to atomic dimensions is very strong and transforms the potential well on the surface into a low and very narrow potential barrier. An electron from the body (metal, semiconductor or dielectric) tunnels to the ion and neutralizes it. The released recombination energy may be then spent on the emission of a second electron. The kinetic energy of secondary electrons is then  $I - 2e\varphi$ , where  $I$  is the ionization potential, and  $\varphi$  is the work function. Usually, the value of  $\gamma_i$  is on the order of  $10^{-3}$ , but in some cases it can reach the value of  $\gamma_i \sim 0.5$ .

## Chapter 2

# A pattern formation primer

Next to knowledge on gas discharges, concepts and methods of pattern formation and nonlinear analysis are used in this thesis. They are introduced in the present chapter, complemented with references for further reading.

### 2.1 General introduction

Dissipative, spatially extended systems which are driven far from equilibrium generate a great diversity of the spatio-temporal structures. The spontaneous emergence of these patterns is a fascinating phenomenon observed in many physical, chemical and biological systems far from thermal equilibrium. The behavior of the patterns can be rather complex, with temporal, spatial or spatio-temporal structures.

Some examples of nonequilibrium patterns with the largest length and time scale in the universe are [31]

- formation of galaxies into sheets and voids
- existence of spiral galaxies (versus elliptical galaxies)
- formation of nonequilibrium stripe patterns common to all gas giant planets like Jupiter, Saturn, Neptune and Uranus.

An example of a pattern on a smaller scale is, for instance, the formation of the ripples in sand on the beach [32]. Apart from these examples from granular matter and the universe, typical examples are the patterns found in chemical reaction-diffusion systems [33,34], hydrodynamic and liquid crystal systems [34, 35], electrochemical systems [36], semiconductors [20,37], optical systems [38], the heart [39,40], the central nervous system [41], and many other biological and ecological systems [42–46]. The most famous and very well understood patterns, which can be prepared in a laboratory are Rayleigh-Benard convection and Taylor-Couette flow in hydrodynamics and the most prominent example of a chemical pattern-forming system is the Belousov-Zhabotinsky reaction. The

complexity and diversity of self-organizing systems is mathematically reflected by nonlinear equations. Nonlinear dynamics [47, 48] gives the framework to describe all these phenomena.

Every pattern-forming process is accompanied by the appearance of characteristic length and time scales. Typically, the extension of the pattern is much larger than the size of an individual element of the system. Therefore, to describe the dynamics of the pattern, it is often not necessary to take into account the individual dynamics of every single element together with their mutual interactions. Instead, it is possible to interpret the pattern dynamics as a collective phenomenon and describe it by a macroscopic mean-field variable or order parameter. Another important feature of self-organization is that, although there are often different time scales involved in the dynamics of a given system, its long-term behavior is typically governed by the slow processes. In this case, it is possible to reduce the number of effective degrees of freedom by adiabatically eliminating the fast variables. Oscillations or wave phenomena in many systems can be described successfully by reaction diffusion models. This is obvious for chemical systems. Examples in the field of living systems are excitation waves (and their breakdown) in the heart [39], the propagation of action potentials in neural tissue [41], and the aggregation patterns in slime mold colonies [49]. Also current filaments in semiconductor devices [20] can be explained by effective reaction-diffusion models. Therefore, there have been many attempts to also explain the localized patterns found in gas-discharge systems by such models [5, 9, 15, 18, 19, 22, 26–28]. This concept will be addressed in detail in Chapter 7.

The investigation of pattern formation is an interdisciplinary task and important contributions were made by studying dynamical systems and deterministic chaos [50, 51]. These branches of applied mathematics can be traced back to Henri Poincare, who first described complex dynamics in a system with three degrees of freedom [52]. Since then, the dynamics of such low-dimensional systems has been intensively investigated [48, 53, 54], in particular chaotic behavior and instabilities due to parameter changes, called bifurcations [55]. Pattern-forming nonequilibrium systems on the other hand, are described by partial differential equations (PDE's) with an infinite number of degrees of freedom. Generic methods include the identification of stationary states and coherent structures, and the analysis of their perturbations.

## 2.2 Stability analysis and bifurcations

The investigated pattern forming system (like in Fig. 3.8) is spatially extended (in  $x - y$  directions) and has a small height (in  $z$  direction). The key steps of linear stability analysis about homogeneous stationary state can be summarized as follows:

- Formulation of the explicit equation of motion for the system

- Reformulation of the equations in dimensionless form in order to introduce the truly independent parameters in dimensionless form
- Use of the periodic boundary condition in order to be able to neglect influence of the boundaries in the extended direction
- Find an explicit stationary solution ( $u = u_0(z)$ ) which is uniform in extended direction  $x$ , for a set of control parameters
- Linearization of the non-linear dimensionless equation of motion about the uniform base state  $u_0$  in order to see how sufficiently small perturbations  $\delta u$  evolve (according to the linear equation which is easier to solve). The coefficients of this linear equation do not depend on the extended coordinates  $x$ .
- The particular solution of the form  $u_k(z) e^{\lambda t} e^{ikx}$  is used to solve linearized equations and to get the growth rate  $\lambda$ .
- Analyze the function  $\text{Re}(\lambda)$  versus wave vector  $k$  and identify local and (even more important) global maxima and the wave vector corresponding to these maxima. The uniform stationary state is linearly stable for the chosen parameters if  $\max_k \text{Re}(\lambda) < 0$ , and unstable otherwise.
- Analyze dispersion relation for different sets of parameters. Find parameter  $p$  of special interest and its critical value defined as  $\max_k \text{Re}(\lambda) = 0$ , and corresponding critical wave number and critical frequency.

### Reaction-diffusion equations as an example and the classification of the patterns due to linear instability

As an illustration, a set of partial differential equations of reaction-diffusion form is considered:

$$\partial_t \mathbf{u} = f(\mathbf{u}; \mathbf{p}) + D \nabla^2 \mathbf{u} . \quad (2.1)$$

$\mathbf{u}$  is a vector (in general  $n$ -component) describing the physical fields,  $f$  models the reaction in the system,  $D$  is a diffusion matrix and  $\mathbf{p}$  is a set of control parameters. The behavior of the solutions of this equation can be quite complex. In general, the nonlinear equations can not be solved analytically. One method to characterize the solutions systematically is perturbation analysis. Following the steps above, we first have to construct the linearized equation of motion. We consider a uniform stationary state  $\mathbf{u}_0$  which is a solution for all values of the control parameters  $\mathbf{p}$ . Then, near this state, it is possible to write the unknown solution  $\mathbf{u}$  as an expansion of Fourier modes in the following way:

$$\mathbf{u} = \mathbf{u}_0 + \int_0^\infty \delta \mathbf{u}_k dk , \quad (2.2)$$

where

$$\delta \mathbf{u}_k = \mathbf{v}_k A_k e^{\lambda t + ikx} + \text{c.c.} + \text{h.o.t.} \quad (2.3)$$



High order terms are denoted by h.o.t and c.c denotes complex conjugates. The Fourier modes with a wave number  $k$  depend on the eigenvector  $\mathbf{v}_k$ , which is determined from the linearized problem, and on the amplitude  $A_k$ .

The complex eigenvalue  $\lambda$  of the linearized problem can be decomposed into its real part  $s$  and imaginary part  $\omega$  in the following way

$$\lambda(k; p) = s(k; p) + i\omega(k; p) ,$$

where it is assumed for simplicity that the bifurcation only depends on one parameter  $p$ . For  $p < p_c$  all perturbations decay, i.e.,  $s < 0$  for all  $k$ . For the spatially extended system, the spectrum of eigenvalues is continuous; but we always focus at the eigenvalue of the largest real part. The critical parameter value  $p_c$  is given by  $s(k_c; p_c) = 0$  for a critical  $k_c$ , while all other modes relax for  $t \rightarrow \infty$ , i.e.  $s(k; p_c) < 0$  for all  $k \neq k_c$ . Then, after a short transient, the critical Fourier mode  $\mathbf{u}_{k_c}$  is given by

$$\delta \mathbf{u}_{k_c} = \mathbf{v}_{k_c} A_{k_c} e^{i(k_c x + \omega_c t)} , \quad (2.4)$$

where  $\omega_c = \omega(k_c; p_c)$ . Therefore, the systems may be classified according to the (critical) mode with the eigenvalue that first crosses the imaginary axis. At the bifurcation point, the critical wave number  $k_c$  and critical frequency  $\omega_c$  may be zero or nonzero, yielding three cases which are of interest here. The case  $k_c = 0$ ,  $\omega_c \neq 0$  corresponds to the so-called Hopf bifurcation, the case  $k_c \neq 0$ ,  $\omega_c = 0$  to the so-called Turing bifurcation, and the case  $k_c \neq 0$ ,  $\omega_c \neq 0$  to the wave bifurcation. Fig. 2.1 shows the linear growth rate ( $s \equiv \text{Re } \sigma$ ) as a

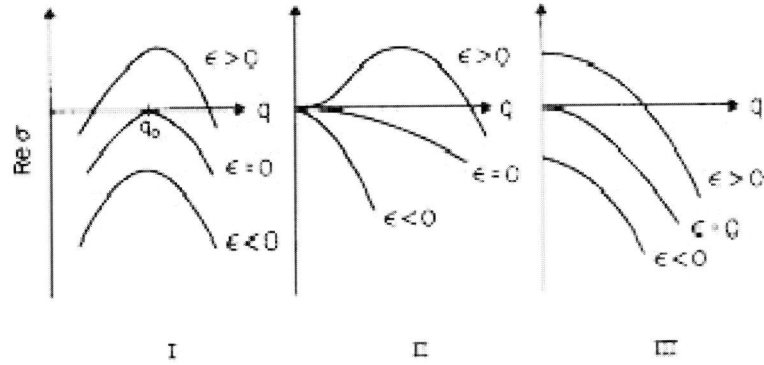


Figure 2.1: Three ways how an unstable mode can emerge on variation of a control parameter  $\epsilon$ . Cases I and II lead to spatially periodic patterns, case III to a homogeneous mode. The notation of this figure taken from [56] differs from our notation. The eigenvalue is denoted by  $\sigma$  (instead of  $\lambda$ ), wave number by  $q$  (instead of  $k$ ) and control parameter is  $\epsilon$  (defined as  $\epsilon = (p - p_c)/p_c$ ).

function of the wave number ( $k \equiv q$ ) for various values of  $\epsilon$ .

So, we have seen that by increasing the control parameter above a certain critical value, patterns arise; the bifurcation from stationary homogeneous state is called stationary if the resulting basic pattern is time independent and it is called oscillatory (Hopf bifurcation) if the critical mode is time-dependent. If the traveling wave mode is the basic pattern, then the instability is of oscillatory type with nonzero wave number.

In addition to the above described classification of the bifurcations, there is another one which distinguishes between supercritical and subcritical transition. In Fig. 2.2 we sketch the bifurcation diagrams of a supercritical (forward) bifurcation and of a subcritical (backward) pitchfork bifurcation. The supercritical case, where the transition is continuous, is analogous to a second order phase transition. When the reduced control parameter  $\epsilon$  passes through zero, the homogeneous stationary state becomes linearly unstable and the system continuously transits to a new stable state. This kind of bifurcation is observed in the experiment [57] (presented in the next chapter) where the system bifurcates continuously from the homogeneous state to a stationary periodic stripe pattern.

#### SUPERCritical BIFURCATION

#### SUBCRITICAL BIFURCATION

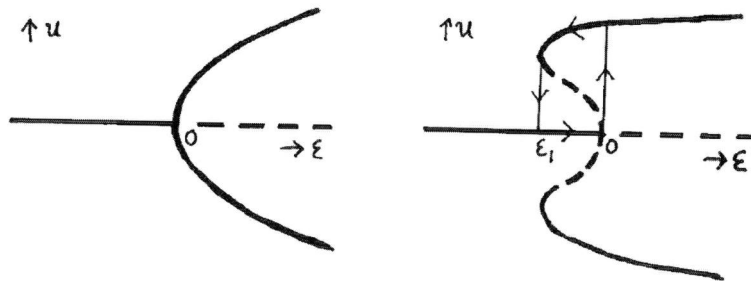


Figure 2.2: The sketch [58] of supercritical and subcritical (pitchfork) bifurcation. Stable state is represented by solid lines and unstable by dashed lines.

The subcritical bifurcation diagram, on the other hand, describes a different situation. If the reduced control parameter  $\epsilon$  is increased through zero, the  $u = 0$  state loses stability and the system will jump to a new branch of solutions. Going in the opposite direction and decreasing  $\epsilon$ , the system will jump back to the stationary homogeneous  $u = 0$  state, but at some different value of the control parameter  $\epsilon_1 \neq 0$ . This hysteresis and discontinuous change of the amplitude is similar to a first order phase transition. For the discharge in nitrogen, in the experiments [11, 12] also presented in the next chapter, a subcritical (Hopf) bifurcation to a homogeneously oscillating state is found.



## Chapter 3

# Experiments

Discharges can form a variety of spatio-temporal structures [59]. The current constriction in a normal glow discharge as well as the longitudinal striations of a long positive column of a glow discharge [1, 2, 60] are some examples. In general, gas discharge systems showing instabilities are often quite complex: with complex external circuits or complex geometries, with gas mixtures and usually driven by AC or pulsed voltage [61–66]. Extensive studies of a variety of spatio-temporal patterns in short discharges can be found in [8–11, 57, 67–74]. Even a simple well-controlled setup, DC driven and with pure nitrogen, exhibits similar phenomena. We focus on this case, since phase diagrams and systematic and detailed studies are available. Therefore, in this chapter, the experiments of Strümpel et al. [11, 12] are discussed as an example of homogeneous temporal oscillations, though oscillations of similar type in a different experimental realizations are observed in several other cases [16, 18, 19]. Experiments [11, 12] show a transition from a homogeneous stationary to a homogeneous oscillating and further to a spatially structured oscillating state. As an example of stationary spatial patterns, an experiment by Astrov et al. is presented [57].

### 3.1 Experimental setup and parameters

The system investigated in [11, 12] is a sandwich-like structure composed of two parallel layers. One layer is the gas gap which represents the nonlinear part of the system, while the other one is the semiconductor layer that operates in its linear regime. The semiconductor and the discharge layer are of the order of mm thick, and the whole structure has a wide lateral aspect ratio. The experimental setup is represented schematically in the Fig. 3.1.

The anode is formed by a glass plate covered with a transparent and conductive indium tin oxide (ITO) layer. It is adjoint to the gas discharge layer filled with nitrogen. The gas pressure is of the order of 40 mbar and the width of the gas gap can be varied from 0.5 to 1.5 mm. The semiconductor acts as the cathode, therefore its outer plane is covered with thin gold film. Due to the small

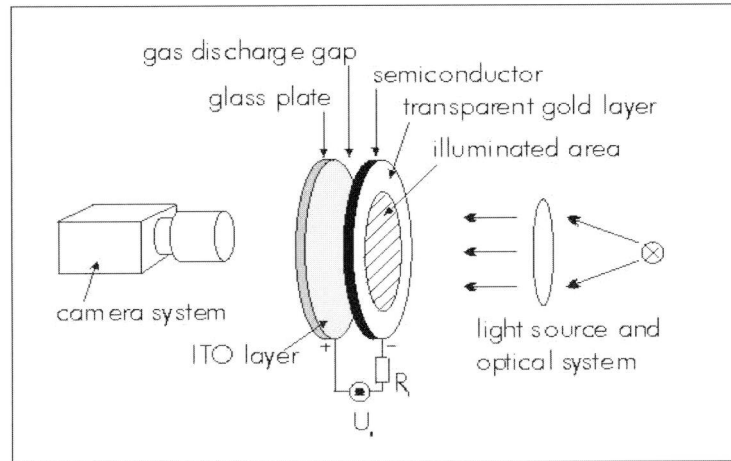


Figure 3.1: Sketch of experimental setup. It consist of two planar electrodes enclosing the discharge gap. The diameter of the discharge area is 30mm and the width of gas gap is typically 1mm.

thickness of only 40nm it is transparent to the visible light with a transmission of about 10%. The resistance of the ITO layer and thin gold film is of course negligible when compared with the resistance of the semiconductor layer. The ITO and the gold electrode are connected to the external electric circuit consisting of a DC voltage supply and a serial resistor that is included to measure the global discharge current in the circuit. The voltage drop at the resistor is negligible in comparison with the applied high voltage. Therefore, the voltage at the electrodes of the semiconductor-gas discharge system is virtually equal to the applied feeding voltage. Furthermore, different types of semiconductor can be used. In experiments of interest to us, GaAs is used [11] or a silicon plate that has been doped with deep impurities of gold or zinc [57]. Due to the photo-sensitivity of the semiconductor, its conductivity can be controlled by irradiation with light. The irradiation can lift the electrons in the semiconductor from the valence to the conduction band. For gallium arsenide, which is a direct semiconductor, the band gap is 1.42eV at room temperature. The conductivity of the semiconductor increases monotonically when the intensity of irradiation  $\phi_L$  is raised. The conductivity as a function of the irradiation intensity is shown in Fig. 3.2.  $\phi_L$  is normalized to the maximum output of the used light source (halogen lamp). Therefore, one of the primary control parameter is the conductivity of the semiconductor layer which can be changed by one order of magnitude. The dark conductivity (without irradiation) is  $3.2 \cdot 10^{-8} (\Omega \text{ cm})^{-1}$ . The width of the semiconductor layer is 1.5 mm and the dielectricity constant of GaAs is 13.1. Another control parameter in the experiments is the applied DC voltage. It is varied from the breakdown voltage up to the 600 V for the smaller gas gap width of  $d = 0.5$  mm, or up to 740 V for the gas gap of 1mm

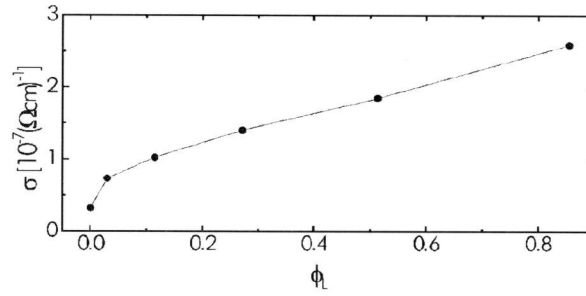


Figure 3.2: Specific conductivity of the semiconductor layer as a function of the intensity of the irradiation  $\phi_L$ . The quantity  $\phi_L$  is normalized to its maximum value.

thickness. Higher voltages are excluded since they can permanently damage the cell.

Although control parameter space is at least four dimensional ( $\phi_L$ ,  $U_0$ ,  $p$ ,  $d$ ), in the following we will mainly confine ourselves to an exploration of the oscillatory behavior of the discharge in the two dimensional projection of the phase space given by  $\phi_L$  and  $U_0$ . The behavior of the system depends on the gas pressure  $p$  and width  $d$  rather weakly since there is a broad range of this parameters where the characteristics of oscillations change only slightly. However, for larger gaps, while other parameters remain unchanged the frequency of oscillations diminishes. Also the amplitude of oscillations decreases when increasing the width of the discharge gap  $d$ .

## 3.2 Overview over experimental results

When the applied voltage is high enough, a discharge will develop in the gas gap and light will be emitted. Usually the light emission is not homogeneous and some patterns are formed. The spatio-temporal behavior of this patterns can be rather complicated. Our system can operate in a stationary homogeneous mode, it can exhibit homogeneous oscillations, and the oscillating modes can undergo a spatial instability leading to blinking filaments.

For low current density, a stationary and spatially homogeneous distribution of the current is stable.

Increasing the current either by increasing the applied voltage  $U_0$  or by increasing the irradiation  $\phi_L$  of the semiconductor, the system starts to oscillate while staying spatially homogeneous.

Homogeneous oscillations exist in a broad range of experimental parameters, see Fig.3.3, where the domain of their existence in the control parameter plane ( $U_0$ ,  $\sigma_{GaAs}$ ) is shown. For Fig.3.3(a), the width of the discharge gap is  $d = 0.5$  mm, whereas the bifurcation diagram in Fig.3.3(b) corresponds to  $d = 1$  mm.

The circles indicate the subcritical bifurcation, which destabilizes the homoge-

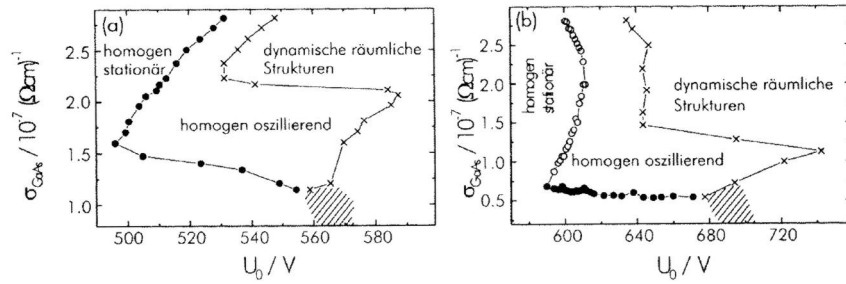


Figure 3.3: Existence-domain of oscillations in the control parameter plane ( $U_0, \sigma_{GaAs}$ ) for two different system sizes (a)  $d = 0.5 \text{ mm}$  and (b)  $d = 1 \text{ mm}$ . The circles denote the bifurcation from homogeneous stationary to homogeneous oscillatory states. The crosses indicate transition to spatially inhomogeneous structures. From [12].

neous stationary state in favor of the oscillatory state. A detailed description of the bifurcation in the case of  $d = 0.5 \text{ mm}$  [Fig. 3.3(a)] is given in Fig. 3.4, where a typical example is presented. There, a hysteretic transition to the oscillatory state can clearly be noted when the irradiation of the semiconductor is used as a control parameter. A peculiarity of the system is that after the bifurcation to the oscillatory state, a further increase of the control parameter  $\phi_L$  leads to a transition back to the stationary state [Fig. 3.3(a)]. This transition shows hysteresis, as well. The width of the hysteresis loops is approximately equal for both cases that are shown in Fig. 3.4. The bifurcation points in Fig. 3.4 are slightly shifted when compared to the corresponding ones in Fig. 3.3(a). This shift is probably due to aging processes of the semiconductor cathode because the two discussed measurements were not done at the same time.

When increasing either the applied voltage  $U_0$  or the semiconductor irradiation  $\phi_L$  further, the system undergoes another bifurcation to a dynamic filament structure where spatial structures emerge while temporal oscillations persist.

### 3.3 Homogeneous oscillations

Oscillations can be observed as the oscillations of the discharge current or the oscillations of the intensity of light emitted from the glow discharge area. The bifurcation to the oscillatory states creates a homogeneously oscillating state whose frequency and amplitude depend on  $U_0$  and  $\phi_L$ . In Fig. 3.5, a typical time series of discharge current and emitted glow light are shown.

The general shape of the signals is similar. However, they are not exactly in phase. The current reaches its maximum somewhat earlier than the discharge

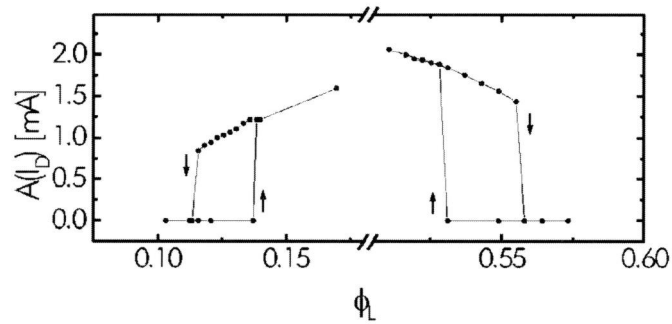


Figure 3.4: An example of bifurcations from a stationary to an oscillatory state [with amplitude  $A(I_D)$ ] when  $\phi_L$  is varied while the supply voltage is fixed at  $U_0 = 510$  V. Two subcritical bifurcations are observed. The directions of change of the control parameter are indicated with arrows. The parameters are  $d = 0.5$  mm and  $p = 40$  mbar. The figure is taken from [11].

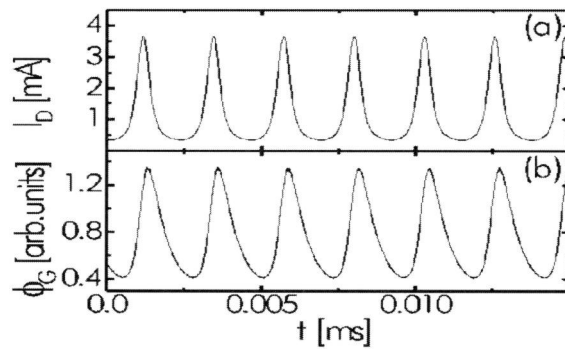


Figure 3.5: Oscillations of the discharge current  $I_D$  (a) and of the intensity  $\phi_G$  of the light emitted by the gas discharge (b). From [11].



glow, whereas the falling edges of emitted light peaks are less steep when compared to the current peaks. This last phenomenon can be explained as the afterglow of the discharge.

The frequency of the oscillation depends on experimental parameters. By altering these parameters, the frequency is changed in the range between 100 and 600 kHz, and the amplitude  $A(I_D)$  of the oscillation of the current (the difference between maximum and minimum values of the current) varies in the range between 0.5 and 4 mA. In [11,12], the properties of the oscillating system are characterized by the discharge current. Equivalently, the signal of the light intensity emitted by the discharge could be used, because the amplitude of its oscillation is proportional to that of the current when the control parameters are varied. When the active area of the device is halved, the oscillation persists with nearly unchanged frequency, while its amplitude decreases to approximately half of its initial value. This gives an indication that the oscillation is actually spatially homogeneous. The direct proof of the spatial homogeneity of the oscillating state is given by making snapshots of the discharge glow at different phases of an oscillation, presented in Fig. 3.6.

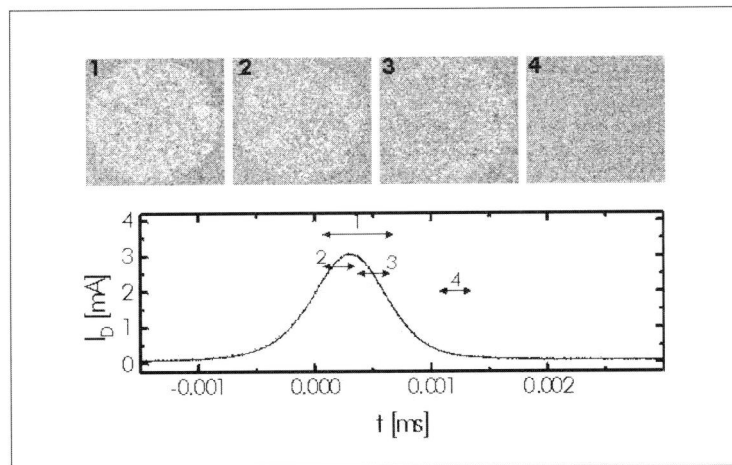


Figure 3.6: Pictures taken with the intensifying camera during the rise and fall of one peak [11]. The exposure times are 630 ns for picture (1) and 300 ns for pictures (2), (3), and (4). The position and length of the corresponding pulses, with which the camera is triggered, are marked in the oscilloscope trace for the current. The frequency of the oscillation is  $f_0=175$  kHz. The parameters are  $U_0 = 583$  V,  $\phi_L = 0.42$ ,  $d = 1$  mm, and  $p = 40$  mbar. From [11].

The obtained images are rather noisy because of the short exposure times, and the low intensity of the emitted light. These data show that the discharge oscillates quite uniformly across the active area. The last picture shown in the sequence refers to a situation where the current has nearly reached its minimum value. No significant emission of light could have been recorded with the applied

technique, while measurements with a photomultiplier tube gave evidence of light emission in this stage.

In the parameter range of the homogeneous oscillations, the dependence of the dynamical characteristics of the oscillating state on the experimental parameters can be investigated. While it is difficult to give a full description of the characteristics for the two-dimensional parameter space  $(U_0, \sigma_{GaAs})$  such as that depicted in Fig. 3.3(a), examples of data for two cross sections of this space are given in Fig. 3.7(a) and (b); and for the bifurcation diagram Fig. 3.3(b) of the larger system ( $d = 1$  mm), the corresponding examples are given in Fig. 3.7(c) and (d). Profiles along parallel cross sections are similar. The hysteresis in the transitions is not shown; the data refer only to the increase in control parameters. Increasing the supply voltage  $U_0$  at constant irradiation of the semiconductor leads to a decrease in the frequency and an increase in the amplitude of the oscillation as can be seen in Fig. 3.7(b). At a further increase of the voltage, both the frequency and the amplitude tend to saturate. In the case of the system size  $d = 1$  mm, behavior is qualitatively the same, only that the profiles  $f(U_0)$  and  $A(U_0)$  are saturating at lower levels.

The variation of the irradiation of the semiconductor at a constant value of the supply voltage gives rise to an increase in the frequency of the oscillation (see Fig. 3.7(a),(c) and (d)). This is the case for both system sizes and all three different values of fixed applied voltage ( $U_0 = 528$  V, 605 V and 616 V). The amplitude changes non-monotonically with the variation of the conductivity of the semiconductor layer. For the smaller system size, just after the bifurcation to the oscillatory state, the amplitude grows, and after passing a maximum, it decreases until the transition back to the stationary state takes place, as can be seen in Fig. 3.7(a). In the case of  $d = 1$  mm, depending on the applied voltage, oscillations may become harmonic. In Fig. 3.7(c), region of harmonic oscillations is denoted by the crosses; The frequency increases linearly with the increase of semiconductor conductivity  $\sigma_{GaAs}$  and at the certain moment, there is a continuous transition from anharmonic to harmonic oscillations. For higher values of  $\sigma$ , there is a jump in frequency at the transition from harmonic to anharmonic oscillations; and amplitude increases linearly, whereas the amplitude of harmonic oscillations is basically constant and much smaller. For small and increasing  $\sigma_{GaAs}$ , the amplitude grows, and after passing a maximum, it decreases until the transition to the region of harmonic oscillations takes place.

For the slightly higher value of the fixed applied voltage, the functions  $f(\sigma)$  and  $A(\sigma)$  are presented in Fig. 3.7(d). As it can be seen, in this case the oscillations are always anharmonic.

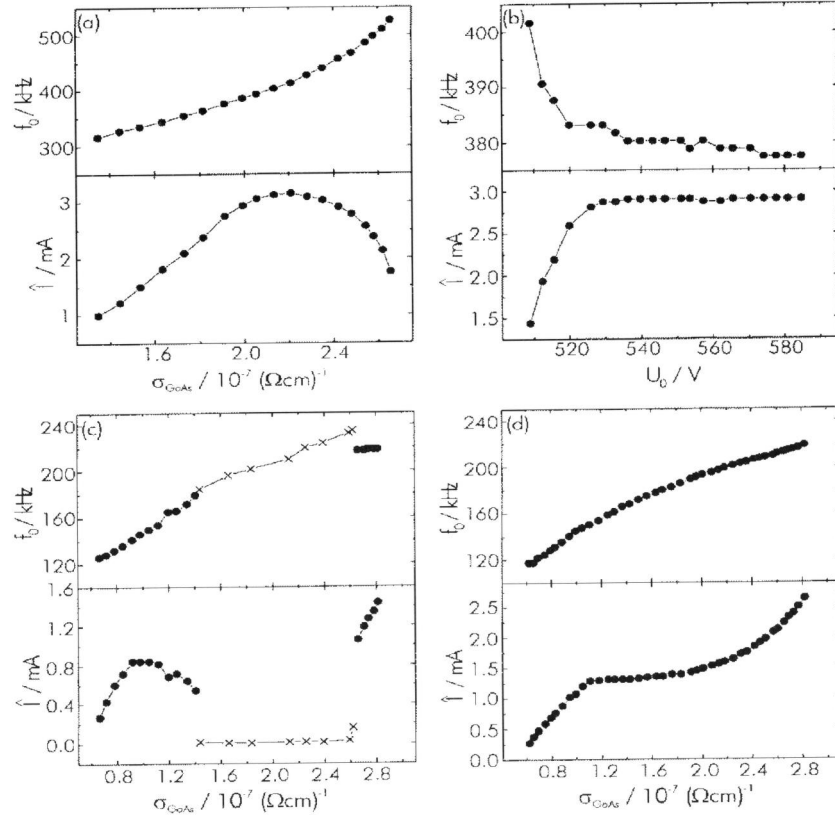


Figure 3.7: Frequency  $f_0$  and the amplitude  $A(I_D)$  of the oscillations of discharge current along the cross section of bifurcation diagrams for  $d = 0.5\text{mm}$  figures (a) and (b); for  $d = 1\text{mm}$  figs.(c) and (d). For case (b), irradiation is kept constant and the voltage is increased. For cases (a), (c) and (d) voltage is kept constant (correspondingly at 528 V, 605 V and 616 V) while intensity of the irradiation is varied. From [12].

### 3.4 Spatial patterns

The same experimental system in a different parameter regime can develop instabilities of the Turing type, which means that the first bifurcation from a homogeneous stationary state will lead to stationary spatial patterns [57]. The experiment uses silicon doped with gold or zinc as a semiconductor material. The thickness of the silicon wafer is of the order of 1 mm and the gas discharge region has approximately the same dimension. The experiment is carried out near liquid nitrogen temperature ( $T \approx 90$  K). The resistivity of the semiconductor is between  $10^7$  and  $10^9 \Omega \text{ m}$ . Further differences in a parameter regimes are in the pressure of nitrogen, which is higher than before ( $p \approx 100$  mbar), as well as the applied voltage (which is now of the order of 2000 V). Though, a detailed investigation of the parameter space is not done, some regularity in the behavior has been reported in [57]. Namely, increasing the control parameter (the feeding voltage or the irradiation intensity), the first bifurcation from the homogeneous stationary state is always towards a stationary inhomogeneous pattern (hexagons or stripes) and only then to some non-stationary state. Stationary hexagon or stripe patterns emerge quite generally in two-dimensional pattern forming systems [56] if the bifurcation is supercritical. One of the scenarios is that hexagon pattern can evolve from the destabilization of low current homogeneous state, by increasing the supply voltage. Further increase of the voltage is accompanied by the transformation of hexagon into the stripe pattern. This example is shown in Fig. 3.8.

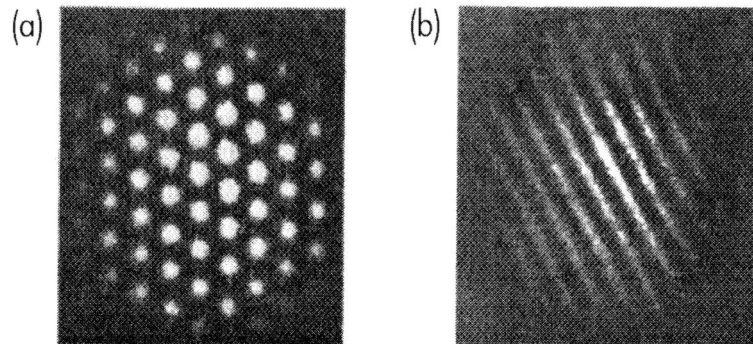


Figure 3.8: (a) Stationary hexagon and (b) stationary stripe pattern. Experimental conditions:  $d = 0.8$  mm,  $p = 120$  mbar and the voltage over the gas discharge and the averaged current densities are: (a) 1815 V,  $9.3 \mu\text{A}/\text{cm}^3$ ; (b) 1935 V,  $18.5 \mu\text{A}/\text{cm}^3$  respectively for the hexagon and stripe distribution of current. Pictures are taken from [57].

The transition from a homogeneous state to a stationary stripe pattern is accompanied by a continuous increase of the amplitude of the structure starting at the threshold value of the control parameter. As explained in a previous chapter, such a behavior is called a supercritical transition. It is found that the wave length of the critical mode is comparable with the dimension of the sandwiched system along the direction of the electric current ( $z$  direction). Also, it has been observed that the wave length decreases when this dimension is diminished. The amplitude of the critical mode is to a good approximation increasing as a square root of the distance from the bifurcation point, which is typical for a supercritical bifurcation [56].

### 3.A Appendix A

#### Paschen curves and the estimation of the secondary emission coefficient

For the investigated experimental setup, experimentally obtained [12] Paschen curves are given in Fig. 3.9. The plot is such that if the approximation (1.3) for the Paschen curve would hold strictly, the curves would precisely lie on top of each other. As they do not, there is some liberty in choosing the value of secondary emission coefficient  $\gamma$ . On the one hand, from the minimum of the Paschen curve, the expressions (1.4) and tabulated values of the coefficients  $A$  and  $B$  [29], the secondary emission coefficient can be estimated. For the discharge gap of 0.5 mm, it is  $\gamma=0.03$ .

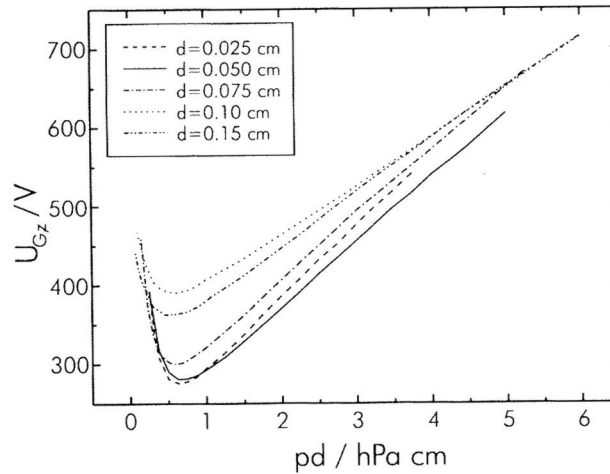


Figure 3.9: Paschen curves for different values of the gas gap width. Conductivity of the semiconductor layer is fixed. From [12].

On the other hand, the value of  $(\frac{E}{p})_{min}$  does not depend on the cathode material. Therefore, measuring the breakdown voltage as a function of pressure for fixed  $d$  (0.5 mm) as shown in Fig. 3.10, the constant  $B$  can be experimentally determined. This procedure determines  $\gamma$  as 0.08 which is the value used throughout this thesis.

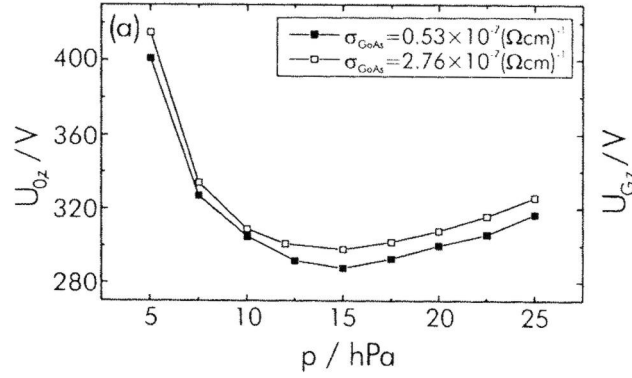


Figure 3.10: Breakdown voltage as a function of pressure for two different values of the conductivity of the semiconductor layer and for fixed  $d = 0.5\text{mm}$ . From [12].

Furthermore, for the same fixed  $d$ , one can read from Fig. 3.9 either the minimal voltage or the value of  $pd$  where the voltage is minimal. Inserting these values into corresponding expressions (1.4), the resulting  $\gamma$ 's differ considerably.

Therefore, this thesis concentrates on the longer system of 1 mm since the results for this system are less dependent on the value of  $\gamma$  as it will be discussed in Chapter 6. Also, whenever it was possible, an investigation of the dependence of discharge properties on the secondary emission coefficient has been performed and results for different values of  $\gamma$  are compared.



# Chapter 4

## Derivation of the model

In this chapter, a simple classical model is introduced for the experiments described in the previous chapter. First, we separately discuss the relevant equations for the gas discharge and for the semiconductor layer. Then a dimensional analysis is performed to identify the truly independent parameters of the system. The complete model in dimensionless form that is analyzed in the remainder of the thesis, is summarized in the scheme on page 42. Furthermore, 1D reductions are discussed that apply when the system is laterally homogeneous.

### 4.1 Gas gap

Modelling the gas discharge system we take two types of ionization processes into account: the  $\alpha$  process of electron impact ionization in a strong field in the bulk of the gas, and the  $\gamma$ -process, the creation of secondary electrons at the cathode. We use continuity equations for electrons and ions coupled to Poisson's equation for the electric field. This ionization-field coupling is a nonlinear mechanism that can cause pattern formation. More precisely, a sufficiently high electric field leads to a multiplication of charge carriers by a local impact ionization reaction. The generated charges drift in the electric field. If their density is high enough, they will modify the field and hence change the local reaction rates and drift velocities. This process is described by continuity equations for the particle densities

$$\partial_t n_e + \nabla \cdot \mathbf{\Gamma}_e = \text{source} , \quad (4.1)$$

$$\partial_t n_+ + \nabla \cdot \mathbf{\Gamma}_+ = \text{source} , \quad (4.2)$$

and the Poisson equation

$$\nabla \cdot \mathbf{E} = \frac{e}{\epsilon_0} (n_+ - n_e) \quad , \quad \mathbf{E} = -\nabla \Phi , \quad (4.3)$$

where  $n_e$  is the electron density,  $n_+$  the ion density and  $\mathbf{E}$  the electric field. We assume here that there is only one non-attaching gas species like nitrogen in



the system. The electric field can be described in electrostatic approximation by the scalar potential  $\Phi$  because for small currents magnetic and relativistic effects can be neglected. In the Poisson equation  $e$  is the absolute value of the electron charge while  $\varepsilon_0$  is dielectric constant.

The particle current densities i.e., the fluxes of electrons and positive ions  $\mathbf{\Gamma}_e$  and  $\mathbf{\Gamma}_+$  can be described in a simplified representation as a sum of diffusion and Ohmic friction (drift). This is true as long as the degree of ionization is so small that dissipative heating can be neglected.

$$\mathbf{\Gamma}_e = -n_e \mu_e \mathbf{E} - D_e \nabla n_e , \quad (4.4)$$

$$\mathbf{\Gamma}_+ = n_+ \mu_+ \mathbf{E} - D_+ \nabla n_+ . \quad (4.5)$$

The drift velocity of electrons or ions is assumed to depend linearly on the field strength with a coefficient that represents the mobility of electrons or ions  $\mu_{e/+}$ , respectively, and  $\mu_+ \ll \mu_e$ , although the linear approximation is valid only in the low-field limit [29]. Furthermore, we will also neglect diffusion  $D_e = 0 = D_+$  and concentrate on the drift contributions to the currents only.

In both continuity equations for electrons and ions, the source term is identical due to charge conservation, since there is only one type of simply ionized particles. In local field approximation, the  $\alpha$  process is modelled as a local source term in the continuity equations (4.1) and (4.2)

$$source = |\mathbf{\Gamma}_e| \bar{\alpha}(|\mathbf{E}|) - \beta n_e n_+ , \quad \bar{\alpha}(|\mathbf{E}|) = \alpha_0 \alpha \left( \frac{|\mathbf{E}|}{E_0} \right) . \quad (4.6)$$

The efficiency of generation of free charges by impact ionization depends on the product of electric field and mean free path of electrons. If this product is large enough, electrons can gain kinetic energy exceeding the ionization energy. Accordingly, there is a threshold field  $E_0$  and for  $|\mathbf{E}| \gtrsim E_0$ , impact ionization can occur, while for  $|\mathbf{E}| \ll E_0$  the ionization process is mostly suppressed. This behavior is modelled by the traditional Townsend approximation [29]:

$$\alpha = \exp(-E_0/|\mathbf{E}|)^s . \quad (4.7)$$

The function is characterized by the parameter  $s$  with typical values  $s = 1/2$  or 1 depending on the type of gas. All our numerical results are for the most common value  $s = 1$ , since  $s = 1/2$  is used only for inert gases.

Furthermore, in the source term we can neglect bulk recombination because recombination processes at the boundaries dominate. Photoionization is also neglected since the ionization crosssection due to photons is much smaller than the one due to electrons. The model applies only to non-attaching gases (like  $N_2$  or He).

To summarize, in our model we have neglected diffusion:  $D_+ = 0 = D_e$  and we have used a number of assumptions and facts such as: There is only one dominant neutral species (one background gas), only one type of ions, only a simple one-step ionization of particles, no recombination, no photoionization, no attachments. Then we arrive at the classical minimal model [13, 22, 29, 75–

79] of reaction and drift of charged particles coupled to an externally imposed electric field which applies to discharges in simple non-attaching gases with low current densities. We will see in later chapters that this simple model is actually sufficient to describe the complex patterns observed in the experiments semi-quantitatively, and that the simplicity of the model actually allows a deeper physical understanding of the pattern formation processes.

At this place, we finally introduce a generalized total electric current as a sum of conductive and displacement current arising from the continuity equations (4.1), (4.2) together with the Poisson equation (4.3)

$$\varepsilon_0 \partial_t \mathbf{E} + e(\mathbf{\Gamma}_e + \mathbf{\Gamma}_+) = \mathbf{J} \quad , \quad \nabla \cdot \mathbf{J} = 0 . \quad (4.8)$$

### 4.1.1 Boundary conditions

In order to complete our model for the gas discharge we have to add (initial conditions and) boundary conditions. The boundary condition at the anode ( $Z = 0$ ) describes the absence of ion emission. Ions are created only in the bulk of the gas and they travel towards the cathode. At the anode the electrons are simply absorbed and if diffusion is neglected, the ion density vanishes

$$\mathbf{\Gamma}_+(X, Y, 0, t) = 0 \quad \iff \quad n_+(X, Y, 0, t) = 0 . \quad (4.9)$$

The boundary condition at the cathode  $Z = d_g$  describes secondary emission, the  $\gamma$ -process. At the cathode, an incoming positive ion will liberate an electron with probability  $\gamma$ , so we have without diffusion

$$\begin{aligned} |\mathbf{\Gamma}_e(X, Y, d_g, t)| &= \gamma |\mathbf{\Gamma}_+(X, Y, d_g, t)| \iff \\ \mu_e n_e(X, Y, d_g, t) &= \gamma \mu_+ n_+(X, Y, d_g, t) , \end{aligned} \quad (4.10)$$

where  $d_g$  represents the thickness of the gas layer. The coefficient  $\gamma$  can be determined from the minimum of the Paschen curve as has been already explained.

Note that in contrast with most other literature, the anode is on the left hand side at  $Z = 0$ . This has the advantage that the electric field in  $z$ -direction is positive, and sign mistakes when evaluating  $\mathbf{E}$  or  $|\mathbf{E}|$  cannot occur. The electric potential  $U$  between the electrodes is

$$U(X, Y, t) = \Phi(X, Y, 0, t) - \Phi(X, Y, d_g, t) > 0 \quad , \quad E(\mathbf{R}, t) = -\nabla \Phi(\mathbf{R}, t) , \quad (4.11)$$

where  $\mathbf{R} = X \hat{i} + Y \hat{j} + Z \hat{k}$  and  $\hat{i}, \hat{j}, \hat{k}$  are unit vectors.

## 4.2 Semiconductor layer

In order to explain how the semiconductor is coupled to the gas discharge layer and which processes are taking part there, I will make small digression and give short introduction to electric fields in matter.

Essential conclusions about electric fields in matter are: Matter can be polarized; its condition being described completely (so far as the macroscopic field is concerned), by a polarization density  $\mathbf{P}$ , which is the dipole moment per unit volume. The contribution of such matter to the electric field  $\mathbf{E}$  is the same as that of a charge distribution  $q_{bound}$  existing in a vacuum and having a density  $q_{bound} = -\nabla \cdot \mathbf{P}$ . In particular, at the surface of polarized matter where there is a discontinuity in  $P$ , this reduces to a surface charge of density  $q_{surface} = -P_n$ . Add any free charge that may be present, and the electric field is the field that this *total* charge would produce in the vacuum. In a dielectric,  $\mathbf{P}$  is proportional to  $\mathbf{E}$  with the coefficient  $\chi_e$  called the electric susceptibility ( $\chi_e = \mathbf{P}/\mathbf{E}$ ). It is useful to define the dielectric constant  $\epsilon = 1 + \chi_e$  as the characteristic of material, since free charge immersed in a dielectric give rise to electric fields which are  $1/\epsilon$  times as strong as the same charge would produce in the vacuum.

To model dielectric response of ‘our’ semiconductor, we use Maxwell’s equations in macroscopic media. The most important is that we take the semiconductor to work in a linear regime. The fields are weak enough that presence of an applied electric field induces an electric polarization proportional to the magnitude of the applied field. The first Maxwell equation (known as Coulomb’s law) says that free charge is divergence of the vector quantity called  $\mathbf{D}$ .

$$\nabla \cdot \mathbf{D} = q \quad .$$

$\mathbf{D}$  is the electric displacement vector ( $\mathbf{D} = \epsilon_0 \mathbf{E} + \mathbf{P}$ ) and is sort of an artificially defined physical variable, since now it seems that  $D$  is the vector field whose source is the free charge distribution in the same sense that the total charge distribution is the source of electric field  $\mathbf{E}$ . In general, that is not true since  $\nabla \times \mathbf{D}$  is usually not zero. Thus the distribution of free charge is not sufficient to determine  $\mathbf{D}$ , but boundary conditions (basically for  $\mathbf{E}$  and  $\mathbf{P}$ ) at the dielectric surfaces are playing an important role. At the boundary between the gas discharge layer and the semiconductor, potential and tangential component of the electric field are continuous, while the jump in the normal component of the electric field is caused by surface charge. A way to deal with the semiconductor is to determine the charge and the current in the semiconductor, and then to apply charge conservation law to the bulk of the semiconductor and at the boundary surface.

From what has been said above, it is clear that:

$$q = \epsilon_s \epsilon_0 \nabla \cdot \mathbf{E} \quad , \quad (4.12)$$

where  $\epsilon_0$  is the electric permittivity of free space, while  $\epsilon_s$  is the dimensionless dielectric constant of the semiconductor (for GaAs is 13.1). Considering the semiconductor layer to work in the linear regime, its (specific electric) conductivity  $\bar{\sigma}_s$  (quantities describing semiconductor will be labeled with ‘s’) is just a constant that represents a coefficient of proportionality among the applied electric field and the current density:

$$\mathbf{J}_s(t) = \bar{\sigma}_s \mathbf{E}_s(t) \quad . \quad (4.13)$$

In general, the conductivity of a semiconductor is a strongly nonlinear function of the electric field, but we assume that we stay in the linear initial part.

To summarize, it is necessary to know the characteristics of the semiconductor as a material (its conductivity and dielectric constant). Besides, it is important to note that in the bulk of the semiconductor there are no free charges. As a consequence, we can work with the equation  $\Delta\Phi = 0$ , since there are no space charges within the semiconductor (or negligible). Finally, one has to derive correct boundary conditions at the semiconductor surface using charge conservation law and the free charge distribution.

### Surface charge and boundary conditions

As it has already been mentioned, at the interface between different media boundary conditions on  $\mathbf{D}$  and  $\mathbf{E}$  are derived from the full set of Maxwell equations. As a result the normal components of  $\mathbf{D}$  and the tangential components of  $\mathbf{E}$  on either side of an interface satisfy:

$$(\mathbf{D}_2 - \mathbf{D}_1) \cdot \hat{n}_{21} = q_s \quad , \quad (4.14)$$

$$(\mathbf{E}_2 - \mathbf{E}_1) \times \hat{n}_{21} = 0 \quad , \quad (4.15)$$

where  $\hat{n}_{21}$  is a unit normal to surface, directed from region 1 to region 2, and  $q_s$  is the macroscopic surface charge density on the boundary surface (not including the polarization charge).

Now, it follows that  $\hat{n} \cdot (\epsilon_s \epsilon_0 \mathbf{E}_s - \epsilon_0 \mathbf{E}_g) = q_s$ . For the sake of clarity (only here), all the variables are having indexes -  $g$  for gas and  $s$  for semiconductor. The way to actually calculate surface charge is to apply charge conservation law at the boundary interface and integrate over the space, using divergence theorem:

$$\int_V \partial_t q \, dV = - \int_V \nabla \cdot \mathbf{J} \, dV \quad (4.16)$$

$$= - \int_S \mathbf{J} \cdot \hat{n} \, da \quad (4.17)$$

$$= J_{gz} - J_{sz} \quad , \quad (4.18)$$

where is  $dV$  volume element and  $da$  an area element with unit outward normal (from the gas to the semiconductor)  $\hat{n}$  at  $da$ .  $J_{gz}$  and  $J_{sz}$  are  $z$  components of the current at the point  $z = d_g$ . Then the important condition which has to be satisfied at the boundary interface  $z = d_g$  for all  $z$  components of the vector fields is

$$\epsilon_s \epsilon_0 E_s - \epsilon_0 E_g = q_s(t=0) + \int_0^t dt [(1 + \gamma)en_+ \mu_+ E_g - \bar{\sigma}_s E_s] \quad . \quad (4.19)$$

To this condition, from now on, we will refer as to 'jump' condition since it tells that the  $z$  component of electric field across the internal border is not continuous but it has a jump due to the existence of surface charge.

### 4.2.1 1D reduction

We can reduce the problem to one spatial dimension  $Z$  transverse to the layers as long as the system is laterally homogeneous. This is very well realized in a substantial parameter regime of the experiments [11, 12]. Therefore charge conservation together with Eq. (4.12) can be rewritten as

$$\partial_t q + \nabla \cdot \mathbf{J}_s = 0 \quad \Rightarrow \quad \nabla \cdot (\epsilon_s \epsilon_0 \partial_t \mathbf{E} + \mathbf{J}_s) = 0 ,$$

and in 1D approximation we derive the conservation of the total current  $J$

$$\epsilon_s \epsilon_0 \partial_t E_s(t) + J_s(t) = J(t) \quad , \quad \partial_z J = 0 , \quad (4.20)$$

where the first term is the displacement current and the second is the conductive current of the semiconductor, and the sum is constant throughout the whole semiconductor layer. The total current in the gas discharge system  $J(t) = \epsilon_0 \partial_t E + e(\Gamma_+ - \Gamma_e)$  ,  $\partial_z J = 0$  is the same as the total current in the semiconductor layer  $J(t)$ . Hence in macroscopic parameters, the semiconductor solves<sup>1</sup>:

$$\begin{aligned} C_s \partial_t U_s(t) + J_s(t) &= J(t) \quad , \quad U_s(t) = R_s J_s(t) \quad , \quad (4.21) \\ C_s &= \frac{\epsilon_s \epsilon_0}{d_s} \quad , \quad R_s = \frac{d_s}{\bar{\sigma}_s} \end{aligned}$$

where  $C_s$  is the capacitance and  $R_s$  the resistance per area,  $d_s$  is the thickness of the semiconductor and the voltage applied to the semiconductor is simply:

$$U_s(t) = E_s(t) d_s. \quad (4.22)$$

In general, there are three independent parameters describing the semiconductor — namely dielectricity constant  $\epsilon_s$ , conductivity  $\bar{\sigma}_s$  and width  $d_s$  —, but in 1D there are only two, namely its capacitance  $C_s$  and its resistance  $R_s$ .

$T_s$  is the Maxwell time and it is the intrinsic time scale of the semiconductor dynamics

$$T_s = C_s R_s = \frac{\epsilon_s \epsilon_0}{\bar{\sigma}_s} . \quad (4.23)$$

This time scale is independent of the thickness of the semiconductor layer although it represents the time of the charge decay through the semiconductor layer. The time scale of experimentally observed oscillations seems to be of this order, and actually almost linear in  $T_s$  when  $\bar{\sigma}_s$  is varied, as will be discussed in Chapter 6.

---

<sup>1</sup>The notation (4.21) is introduced to relate the analysis to the work of [24].

### 4.3 Complete model in dimensionless form

By dimensional analysis, the independent dimensionless parameters of the model are identified. It is convenient to start from the Townsend approximation of the impact ionization coefficient in order to introduce the units for time, lengths and fields, therefore  $\alpha_0$  and  $E_0$  are essential quantities for this analysis. First, we introduce  $r_0 = 1/\alpha_0$  so to measure all lengths in units of the ionization length. Second natural unit is given by the characteristic impact ionization field  $E_0$  and the electron mobility  $\mu_e$  determining characteristic velocity  $v_0 = \mu_e E_0$ . Consequently the time unit is  $t_0 = r_0/v_0$  and the charge unit will be determined by the Colombo's law. Therefore, dimensionless lengths, times and fields are:

$$\begin{aligned} r &= \frac{R}{r_0} \quad , \quad \tau = \frac{t}{t_0} \quad , \quad \sigma(r, \tau) = \frac{e n_e(R, t)}{q_0} \quad , \\ \rho(r, \tau) &= \frac{e n_+(R, t)}{q_0} \quad , \quad \mathcal{E}(r, \tau) = \frac{E(R, t)}{E_0} \quad , \quad \text{where :} \quad (4.24) \\ r_0 &= \frac{1}{\alpha_0} \quad , \quad t_0 = \frac{1}{\alpha_0 \mu_e E_0} \quad \text{and} \quad q_0 = \epsilon_0 \alpha_0 E_0 \quad . \end{aligned}$$

An effective field-dependent impact ionization coefficient  $\alpha(E) = Ap \exp(-Bp/|E|)$ , now in dimensionless units, reads

$$\alpha(\mathcal{E}) = e^{-(1/|\mathcal{E}|)^s} \quad , \quad (4.25)$$

where we use only  $s = 1$  as has been already said.  $p$  is the gas pressure and mobilities then scale with inverse pressure  $\mu_e = \bar{\mu}_e/p$  and  $\mu_+ = \bar{\mu}_+/p$ . It is important to note that other characteristic properties scale with the pressure in the following way:

$$\begin{aligned} r_0 &= \frac{1}{Ap} \quad , \quad E_0 = Bp \quad , \quad (4.26) \\ v_0 &= \mu_e E_0 = \bar{\mu}_e B \quad , \quad q_0 = \frac{\epsilon_0 E_0}{r_0} = \epsilon_0 AB p^2 \quad . \end{aligned}$$

Further, we can rescale the total applied voltage as follows:

$$u_t = \frac{U_t}{E_0 r_0}$$

and introduce the small parameter

$$\mu = \frac{\mu_+}{\mu_e} \quad ,$$

which is the ratio of ion over electron mobility, and state that neither of these quantities depend on pressure. Here, we have also recalled the scaling properties with pressure  $p$ , such that the pressure dependent similarity laws can easily be identified in the represented dimensionless results.

It should be noted that only bulk gas parameters have been used for the dimensionless analysis. Therefore dimensionless properties do not depend on the secondary emission coefficient.

The properties of the semiconductor are also rescaled:

$$\sigma_s = \frac{\bar{\sigma}_s}{\mu_e q_0} \quad , \quad (4.27)$$

while dielectric constant  $\epsilon_s$  is already dimensionless.

The dimensionless lengths of gas discharge layer and the semiconductor are

$$L = \frac{d_g}{r_0} \quad , \quad L_s = \frac{d_s}{r_0} \quad , \quad (4.28)$$

and they scale with the pressure as  $Apd$ .

That brings us to the point where we can sketch the complete system in the dimensionless form schematically as:

anode ( $z = 0$ ):	$\phi = u_t$
boundary condition:	$\rho = 0$
G A S	impact ionization
electrons:	$\partial_\tau \sigma - \nabla \cdot (\sigma \mathcal{E}) = \sigma  \mathcal{E}  \exp(-1/ \mathcal{E} )$
ions:	$\partial_\tau \rho + \mu \nabla \cdot (\rho \mathcal{E}) = \sigma  \mathcal{E}  \exp(-1/ \mathcal{E} )$
electric field:	$\nabla \cdot \mathcal{E} = \rho - \sigma \quad , \quad \mathcal{E} = -\nabla \phi$
boundary conditions ( $z = L$ ):	$\gamma \mu \rho = \sigma$ <span style="float: right;">secondary emission</span>
at the cathode	$q_s = (\epsilon_s \mathcal{E} _{L^+} - \mathcal{E} _{L^-}) \cdot \hat{z}$ <span style="float: right;">surface charge</span>
linear S E M I C O N D U C T O R	$\mathbf{j}_s = \sigma_s \mathcal{E} \quad , \quad \mathbf{D} = \epsilon_s \mathcal{E} \quad , \quad \nabla \cdot \mathbf{D} = 0$
cathode ( $z = L + L_s$ ):	$\phi = 0$

The model consists of the continuity equations for electrons and ions, coupled to the Poisson equation. The only processes taken into account are the impact ionization in the bulk of the gas and the secondary emission at the cathode. The semiconductor is easy to describe since it works in a linear regime. This representation of our system is clear and simple, though we can use different form of these equation for the numerical calculations and especially in 1D approximation, elimination of some of the variables is advisable.

### 4.3.1 1D representation of the full model

For further calculations, it is useful to note, that the one-dimensional approximation of the above dimensionless equations (two continuity equations and Poisson equation ) makes the total electric current homogeneous

$$j(\tau) = \partial_\tau \mathcal{E} + \mu \rho \mathcal{E} + \sigma \mathcal{E} \quad , \quad \partial_z j(\tau) = 0 \quad . \quad (4.29)$$

The dimensionless total current is defined as:

$$j(\tau) = \frac{J(t)}{q_0 r_0 / t_0} = \frac{J(t)}{\mu_e E_0 \epsilon_0 \alpha_0 E_0} \propto \frac{J}{p^2} \quad . \quad (4.30)$$

This identity (4.29) can be used to substitute either ion current or the electron current by  $j(\tau)$ . After eliminating the ion dynamics by the total current  $j(\tau)$ , the equations of motion of the gas discharge becomes

$$\partial_\tau \sigma = \partial_z (j_e) + j_e \alpha(\mathcal{E}) \quad , \quad (4.31)$$

$$\partial_\tau \mathcal{E} = j(\tau) - (\mu + 1) j_e - \mu \mathcal{E} \partial_z \mathcal{E} \quad , \quad (4.32)$$

where  $j_e = \sigma \mathcal{E} = -e J_e / [q_0 r_0 / t_0]$  is the dimensionless conductive current carried by the electrons.

The boundary conditions for the glow discharge are:

$$\partial_\tau \mathcal{E}(0, \tau) = j(\tau) - \sigma(0, \tau) \mathcal{E}(0, \tau) \quad , \quad (4.33)$$

$$\partial_\tau \mathcal{E}(L, \tau) = j(\tau) - \frac{1 + \gamma}{\gamma} \sigma(L, \tau) \mathcal{E}(L, \tau) \quad . \quad (4.34)$$

As the analyzed system is driven by the DC voltage, the total current is a conserved quantity through the whole system. The applied (total) voltage  $U_t$  over the complete system is kept fixed ( $\partial_t U_t = 0$ ):

$$U_t = U(t) + U_s(t) \quad , \quad U(t) = \int_0^{d_g} E(r, t) dr \quad . \quad (4.35)$$

If we now introduce the dimensionless potentials:

$$u_t = \frac{U_t}{E_0 r_0} \quad , \quad u(\tau) = \int_0^L \mathcal{E}(z, \tau) dz \quad , \quad (4.36)$$

from the equation (4.21) the total current can be expressed as:

$$j(\tau) = \frac{1}{\mathcal{R}_s} \left( u_t - u(\tau) - \tau_s \partial_\tau u(\tau) \right) \quad , \quad (4.37)$$

with the dimensionless parameters

$$\mathcal{R}_s = R_s \frac{\mu_e q_0}{r_0} \quad , \quad \tau_s = \frac{T_s}{t_0} = \frac{\epsilon_s}{\sigma_s} \quad . \quad (4.38)$$



The voltage  $u_t(\tau) = \int_0^L \mathcal{E}(z, \tau) dz$  is related to the electric field  $\mathcal{E}$  and potential  $\phi$  in differential form as

$$\mathcal{E}(z, \tau) = -\partial_z \phi(z, \tau) \quad , \quad u(\tau) = \phi(0, \tau) - \phi(L, \tau), \quad (4.39)$$

where gauge freedom allows one to choose

$$\phi(0, \tau) = 0. \quad (4.40)$$

Hence the dynamics of the complete system in one-dimensional representation is described by Eqs. (4.31)–(4.34), (4.37), (4.39) and (4.40). The system is characterized completely by the independent dimensionless parameters  $\mu$ ,  $L$  and  $\gamma$  for the gas discharge layer,  $\tau_s$  and  $\mathcal{R}_s$  for the semiconductor layer and the total applied DC voltage  $u_t$ .

For a better physical insight, it might be instructive to rewrite equation (4.37) as:

$$\partial_\tau u = \frac{u_t - u - \mathcal{R}_s j}{\tau_s}. \quad (4.41)$$

The dynamics of the voltage at the gas-semiconductor interface is characterized by the time scale  $\tau_s$  which is nothing less but the Maxwellian time

$$\tau_s = \mathcal{R}_s \mathcal{C}_s \quad , \quad \text{where is } \mathcal{C}_s = C_s \frac{r_0}{t_0 \mu_e q_0}. \quad (4.42)$$

The load line is  $u = u_t - \mathcal{R}_s j$  and it is a stationary solution of the semiconductor part of the system.

## Chapter 5

# Stationary solutions

As a first step of any further investigation, the behavior and the resulting current-voltage-characteristics of the purely one-dimensional gas discharge system have to be understood. In this chapter, the transition from Townsend to glow discharge is investigated numerically in one space dimension in the full parameter space within the previously described classical model: with electrons and positive ions drifting in the local electric field, impact ionization by electrons ( $\alpha$  process), secondary electron emission from the cathode ( $\gamma$  process) and space charge effects. We also perform a systematic analytical small current expansion about the Townsend limit up to third order in the current that fits our numerical data very well.

Depending on the two determining parameters  $\gamma$  and system size  $pd$ , the transition from Townsend to glow discharge with growing current density can show the textbook subcritical behavior, but for smaller values of  $pd$ , we also find supercritical or some unexpected intermediate ‘mixed’ behavior. The term ‘subcritical’ is used here to describe falling current-voltage characteristics i.e., decrease of the voltage with current grow, while ‘supercritical’ denotes increase of the voltage. Our work shows the same qualitative dependence of  $U = U(I, pd)$  for fixed  $\gamma$  as the old experiments by Pokrovskaya-Soboleva and Klyarfeld [80]. Furthermore, the analysis lays the basis for understanding the complex spatio-temporal patterns in short planar ‘barrier’ discharge systems.

### 5.1 Introduction

An investigation of the system [11] along the lines of the textbook [29] shows that the pattern formation occurs at the space charge driven transition from Townsend to glow discharge. The gas discharge layer is rather short, more precisely, the product  $pd$  of gas pressure  $p$  times electrode distance  $d$  is small. This raises the question of the Townsend to glow transition for small  $pd$ . However, despite a history of more than 70 years, we are not aware of any thorough and complete study of this classical problem. Therefore, our aim in the present

chapter is to develop a consistent picture of the Townsend to glow transition in one dimension from analytical and numerical investigations, in particular, for short systems.

Many authors focus on quite long discharges that have a clearly pronounced subcritical characteristics, i.e., for fixed large  $pd$  and growing total current  $I$ , the voltage first decreases from the Townsend limit towards the normal glow regime, then it increases again in the abnormal glow regime as has been seen in Fig. 1.2 of Chapter 1. The initial decrease of voltage from Townsend discharge towards normal glow creates a regime of negative differential conductivity, and some authors [19] believe that negative differential conductivity is generic for this system.

However, already in the early 1940'ies, e.g., in the extensive review by Druyvesteyn and Penning [75], it was suggested that this subcritical behavior might not be the only possible one, but that also a monotonic increase of voltage with current was possible. Such a behavior we will call supercritical, in line with modern bifurcation theory. There are early experimental papers by Pokrovskaya-Soboleva and Klyarfeld [81] and McClure [82] that clearly indicate a supercritical transition for small values of  $pd$  in hydrogen and deuterium in combination with metal electrodes. Later data by the same authors [80] is reproduced in Raizer's textbook [29], however, only for rather long systems with subcritical characteristics.

Theoretical insight into the question of bifurcation behavior can be gained by analytical or numerical investigation of an appropriate model. The classical model contains the drift of charged particles in the local field, the  $\alpha$ -process of impact ionization in the bulk of the gas, the  $\gamma$ -process of secondary electron emission from the cathode, and space charge effects.

Numerical calculations date back to the 50'ies [76], the first numerical evaluations using an 'electronic computer' can be found in the early 60'ies in [77, 78]. In particular, in the work of Ward [78], current-voltage characteristics with or without a region of negative differential conductivity can be found for different values of  $pd$ . However, computing power at the time was quite restricted and hence only a few current-voltage-characteristics were calculated. The work does not seem to have been extended significantly later on. We will take up the issue in Section 5.4.

Analytical efforts were constrained to small current expansions about the Townsend limit. The old German textbook of Engel and Steenbeck [13] contains an elegant argument that the initial increase or decrease of the characteristics from the Townsend limit depends on the sign of  $\alpha''(E_T)$  where  $\alpha(E)$  is the effective impact ionization coefficient as a function of the electric field  $E$ , and  $''$  denotes the second derivative (of  $\alpha$  with respect to  $E$ ) evaluated at Townsend's breakdown field  $E_T$ . We recall this argument in Subsection 5.3.2. The book [13] also gives an explicit expression for the coefficient  $c_2 \propto \alpha''(E_T)$  in the expansion  $U(I) = U_T + c_2 I^2$ , however, without derivation or reference. Exactly the same statements can be found more than 60 years later in Raizer's much read textbook [29]. Kolobov and Fiala [22] assume that  $\alpha'' = 0$  marks the point where negative differential conductivity disappears. A similar small current expansion of the

voltage about the Townsend limit has recently been performed in [19], but with a different result — here the leading correction is found to be linear in the current rather than quadratic. None of the two results has been compared to numerical solutions. In the present paper, we will present yet another result for the small current expansion and evaluate it to higher orders. Our derivation is a systematic expansion and in very good agreement with our numerical results.

In general, our aim in the present chapter is a consistent theoretical investigation of the simple classical model of these discharges treated by so many authors [13, 18, 19, 22, 29, 75–79]. We will use both analytical and numerical methods for the exploration of the full parameter space, extending and correcting the previous literature. The exploration of the full parameter space is possible, because the current-voltage characteristics in appropriate dimensionless units depends essentially only on two parameters: the secondary emission coefficient  $\gamma$  and the dimensionless system size  $L \propto pd$ .

Of course, various extensions of the model can be considered: particle diffusion, attachment, nonlinear particle mobilities, a field-dependent secondary emission rate or nonlocal ionization rates. However, e.g., Boeuf [83] has argued that for the transition from normal to abnormal glow, nonlocal terms in the impact ionization reaction should be taken into account through hybrid numerical models [84], while in the subnormal regime between Townsend and normal glow, a local fluid model is considered sufficient [22]. This supports the strategy to first seek a full understanding of the predictions of the classical model as a corner stone and starting point for any further work.

In the present work, we perform a systematic analytical expansion of the voltage about the Townsend limit up to  $O(I^3)$ , recovering the qualitative features of the solution from [13, 29]: in particular, we find that a linear term in current  $I$  indeed is missing, and that the coefficient  $c_2$  indeed is proportional to the  $\alpha''(E_T)$ , but with a different proportionality constant. In fact, our coefficient  $c_2$  does depend on the secondary emission coefficient  $\gamma$ , while the expression given in [13, 29] does not depend on  $\gamma$  at all. We compare our systematic expression with the earlier result in the limit of small  $\gamma$ . We also evaluate the next order  $O(I^3)$ . Our analytical result fits our numerical solutions very well within its range of validity. The stationary states of the pattern forming system [11] are within the range of validity of this expansion.

Furthermore, we explore the current-voltage characteristics numerically beyond the range of the small current expansion in the full parameter space. We show that within the classical model, there is not only the familiar subcritical bifurcation from Townsend to glow discharge for large values of  $pd$ , but for sufficiently small values of  $pd$ , the bifurcation is supercritical, in agreement with the scenario suggested by Druyvesteyn and Penning [75]. Furthermore, for intermediate values of  $pd$ , there always exist completely unexpected ‘mixed’ bifurcations. This surprising finding implies that the negative differential conductivity does not vanish when  $\alpha''(E_T) = 0$  in the Townsend limit, as most authors assume [22, 29], but only for smaller values of  $pd$ . These statements are true for all relevant values of secondary emission  $\gamma$ . Our three-dimensional plots of the voltage as a function of dimensionless system size  $L \propto pd$  and current  $I$

for a given gas-electrode combination are done in the same manner as the old experimental plots by Pokrovskaya-Soboleva and Klyarfeld [80].

The chapter is organized as follows: in Section 5.2, we reformulate the stationary one-dimensional problem as a boundary condition problem. In Section 5.3, we recall the Townsend limit and the classical argument of Engel and Steenbeck on the qualitative dependence of the small current expansion on  $\alpha''$ . We then perform a new systematic small current expansion up to third order in the total current  $I^3$ , determine the coefficients of the expansion explicitly and compare it with earlier results in the limit of small  $\gamma$ . Section 5.4 begins with our numerical strategy and a discussion of the parameters with their ranges. The parameter dependence of the current-voltage characteristics on system size  $L \propto pd$  and secondary emission coefficient  $\gamma$  is first presented in the form of  $(I, U, pd)$ -plots for fixed  $\gamma$  as in [80]. We then present spatial plots of electron current and field, and compare our numerical results to our analytical small current expansion. Finally, we classify the bifurcation structure in the complete relevant parameter space. Last Section contains a summary and an outlook onto the implications of this work for spatio-temporal pattern formation in barrier discharges. Two appendices contain the proof of the uniqueness of the solution of the boundary value problem and details of the small current expansion in order  $I^3$ .

## 5.2 The stationary problem

For a given dimensionless total current  $j$ , mobility ratio  $\mu$ , secondary emission coefficient  $\gamma$ , functional form  $\alpha(\mathcal{E})$  as defined in previous chapter Eq.(4.25) and dimensionless system length  $L$ , the stationary solutions of Eq.(4.31) for electron current density and Eq.(4.32) for electric field are determined by

$$d_z j_e = -\alpha(\mathcal{E}) j_e , \quad (5.1)$$

$$\mu \mathcal{E} d_z \mathcal{E} = j - (1 + \mu) j_e , \quad (5.2)$$

together with the boundary conditions (4.10), (4.9) that conveniently are expressed by  $j$  as

$$j_e(0) = j \quad \text{and} \quad j_e(L) = j e^{-L_\gamma} \quad (5.3)$$

where we recall that cathode is at  $z = L$ , and we define new constant  $L_\gamma$  as:

$$L_\gamma = \ln \frac{1 + \gamma}{\gamma} . \quad (5.4)$$

We assume that  $\alpha(\mathcal{E}) > 0$  and  $\partial\alpha/\partial|\mathcal{E}| > 0$  within the relevant range of fields  $\mathcal{E}$ . We prove in Appendix A that this determines a unique solution for the two functions  $j_e(z)$  and  $\mathcal{E}(z)$ . Finally, the integrated field yields the potential

$$u = \int_0^L \mathcal{E}(z) dz , \quad (5.5)$$

and hence the current-voltage-characteristics  $u(j)$ .

### 5.2.1 A global conservation law

$\alpha(\mathcal{E}(z))$  for all solutions  $(j_e(z), \mathcal{E}(z))$  is related to  $L_\gamma$  through the global conservation law

$$\int_0^L \alpha(\mathcal{E}(z)) dz = L_\gamma . \quad (5.6)$$

This can be seen by formally integrating Eq. (5.1) with the boundary condition  $j_e(0) = j$  with the result

$$j_e(z) = j e^{-\int_0^z \alpha(\mathcal{E}(z')) dz'} , \quad (5.7)$$

and by evaluating this solution with the boundary condition  $j_e(L) = j e^{-L_\gamma}$  at  $L$ . The identity (5.6) can also be found in [13, 29].

It follows immediately that for a bounded function with  $\alpha(\mathcal{E}) \leq 1$  for all  $\mathcal{E}$  as in (4.25), the system size  $L$  needs to be larger than  $L_\gamma$

$$L \geq L_\gamma \quad (5.8)$$

to sustain a stationary self-sustained discharge. This is true for arbitrary currents  $j$  and space charge effects.

The identity (5.6) also plays a prominent role in the small current expansion about the Townsend limit, as we will see now.

## 5.3 Analytical small current expansion

### 5.3.1 The Townsend limit

The well-known Townsend limit can be understood as a consequence of (5.6): for currents  $j$  so small that  $\partial_z \mathcal{E} \approx 0$  in (5.2), the electric field is constant  $\mathcal{E}(z) = \mathcal{E}_T$ . Eq. (5.6) then reduces to the familiar ‘ignition condition’ [29]

$$\alpha(\mathcal{E}_T)L = L_\gamma \iff \gamma \left( e^{\alpha(\mathcal{E}_T)L} - 1 \right) = 1 . \quad (5.9)$$

The Paschen curve relates the potential  $u_T = \mathcal{E}_T L$  in the Townsend limit to the system size  $L$  through  $\alpha(u_T/L) = L_\gamma/L$ . In particular, for the form of Eq. (4.25), the Paschen curve is

$$u_T(L, \gamma) = \frac{L}{\ln^{1/s}(L/L_\gamma)} , \quad (5.10)$$

while the field is

$$\mathcal{E}_T(L, \gamma) = \frac{1}{\ln^{1/s}(L/L_\gamma)} . \quad (5.11)$$

In dimensionless form,  $u_T$  and  $\mathcal{E}_T$  depend only on the secondary emission coefficient  $\gamma$ , system size  $L$  and the parameter  $s$  in (4.25). The Townsend field  $\mathcal{E}_T$  increases monotonically with decreasing system size  $L$  and diverges for  $L \downarrow L_\gamma$ . The Paschen curve  $u_T(L, \gamma)$  (5.10) has a minimum at  $L = L_\gamma e^{1/s}$  and diverges both for  $L \downarrow L_\gamma$  and for  $L \rightarrow \infty$ .

### 5.3.2 The argument of Engel and Steenbeck

In the old German textbook of Engel and Steenbeck [13], the following argument for an expansion about the Townsend limit can be found: write the electric field as the Townsend field  $\mathcal{E}_T$  plus a perturbation  $\Delta(z)$ , and note that the potential is the integrated field:

$$\mathcal{E}(z) = \mathcal{E}_T + \Delta(z) \quad , \quad u = u_T + \int_0^L \Delta(z) dz . \quad (5.12)$$

The local impact ionization coefficient can then be expanded about  $\alpha(\mathcal{E}_T)$  as

$$\alpha(\mathcal{E}(z)) = \alpha(\mathcal{E}_T) + \alpha'(\mathcal{E}_T) \Delta(z) + \frac{\alpha''(\mathcal{E}_T)}{2} \Delta^2(z) + \dots . \quad (5.13)$$

For fixed system size  $L$  and parameter  $L_\gamma$ , the global constraint (5.6) relates different solutions  $\mathcal{E}(z)$  to  $\alpha(\mathcal{E}_T)L$  through

$$\begin{aligned} \alpha(\mathcal{E}_T)L &= \int_0^L \alpha(\mathcal{E}(z)) dz \\ &= \alpha(\mathcal{E}_T)L + \alpha'(\mathcal{E}_T) \int_0^L \Delta(z) dz \\ &\quad + \frac{\alpha''(\mathcal{E}_T)}{2} \int_0^L \Delta^2(z) dz + \dots , \end{aligned} \quad (5.14)$$

where the expansion of  $\alpha$  was used in the second step. This identity allows to express  $\int_0^L \Delta(z) dz$  by the higher order terms  $\int_0^L \Delta^n(z) dz$ ,  $n = 2, 3, \dots$ . Insertion of this expansion into the definition of  $u$  yields

$$u = u_T - \frac{\alpha''(\mathcal{E}_T)}{2 \alpha'(\mathcal{E}_T)} \int_0^L \Delta^2(z) dz + \dots \quad (5.15)$$

Since  $\Delta^2$  is positive and since  $\alpha$  is assumed to be an increasing function of  $\mathcal{E}$ , the sign of the correction is determined by the sign of  $\alpha''$ . This statement from [13] is recalled in the recent literature [22, 29]. It should be noted that the estimate (5.15) is valid as long as  $|\alpha^{(n)} \int \Delta^n dz| \ll |\alpha'' \int \Delta^2 dz|$  for all  $n \geq 3$ .

The question is now how to calculate  $\int_0^L \Delta^2(z) dz$ . In [13], a result is quoted referring to a long calculation without reference. The same result is given more than 60 years later in [29] in Section 8.3 with a sketch of an argument and again without reference. The argument assumes that  $|J_+| \gg |J_e|$  throughout the discharge volume. This assumption is in disagreement with the boundary condition (4.9). A somewhat different argument based on a constant space charge through the whole system is given in [81]. In Ref. [29], the electric field profile is assumed to be  $\mathcal{E}(z) \propto \sqrt{1 - z/z_0}$ , while in Ref. [81] it is assumed to be  $\mathcal{E}(z) \propto (1 - z/z_0)$  where the length scale  $z_0$  depends on the current  $j$ . In both cases, the breakdown of the approximation is determined from the field vanishing at the anode:  $\mathcal{E}(L) \approx 0$ . This prescription yields no dependence

on  $\gamma$  at all, quite in contrast to our results below. The functional forms for  $\mathcal{E}(z)$  should be compared with our systematic analytical results (5.16), (5.32) below (note that we reversed the order of anode and cathode), and with our numerically derived field profiles in Figs. 5.4 and 5.5. They do not justify the Ansätze given above.

Rather a consistent ansatz is chosen in [19], and the structure of their expansion in terms of  $e^{-L_\gamma}$  and  $L_\gamma$  is quite similar to ours below. However, these authors fail to incorporate the global conservation law (5.6), and get a correction already in linear order, in contrast to the rigorous result (5.15) above.

### 5.3.3 A systematic expansion in small $j$

We now perform a systematic expansion in powers of  $j$  about the Townsend limit. In principle, this expansion can be extended to arbitrary order. We have evaluated it up to  $O(j^3)$ . We write the field correction as a power series in  $j$ , namely  $\Delta(z) = j \mathcal{E}_1(z) + j^2 \mathcal{E}_2(z) + \dots$ , and use the same ansatz for the current  $j_e(z)$

$$\mathcal{E}(z) = \mathcal{E}_T + j \mathcal{E}_1(z) + j^2 \mathcal{E}_2(z) + \dots, \quad (5.16)$$

$$j_e(z) = j \iota_1(z) + j^2 \iota_2(z) + \dots, \quad (5.17)$$

and we introduce the short hand notation

$$\alpha = \alpha(\mathcal{E}_T), \quad \alpha' = \alpha'(\mathcal{E}_T), \quad \alpha'' = \alpha''(\mathcal{E}_T), \quad \dots \quad (5.18)$$

for the Taylor expansion of

$$\begin{aligned} \alpha(\mathcal{E}(z)) &= \alpha + \alpha' (j\mathcal{E}_1(z) + j^2\mathcal{E}_2(z) + \dots) \\ &\quad + \frac{\alpha''}{2} (j\mathcal{E}_1(z) + j^2\mathcal{E}_2(z) + \dots)^2 + \dots \end{aligned} \quad (5.19)$$

Insertion of the Ansätze (5.16), (5.17) into Eqs. (5.1) and ordering in powers of  $j$  yields

$$O(j^1) : \quad \partial_z \iota_1(z) = -\iota_1(z) \alpha, \quad (5.20)$$

$$O(j^2) : \quad \partial_z \iota_2(z) = -\iota_2(z) \alpha - \iota_1(z) \alpha' \mathcal{E}_1(z), \quad \dots \quad (5.21)$$

For Eq. (5.2), the same procedure gives

$$O(j^0) : \quad \partial_z \mathcal{E}_T = 0, \quad (5.22)$$

$$O(j^1) : \quad \mu \mathcal{E}_T \partial_z \mathcal{E}_1 = 1 - (1 + \mu) \iota_1(z), \quad (5.23)$$

$$O(j^2) : \quad \mu \mathcal{E}_T \partial_z \mathcal{E}_2 + \mu \mathcal{E}_1 \partial_z \mathcal{E}_1 = -(1 + \mu) \iota_2(z), \quad \dots \quad (5.24)$$

The boundary condition (5.3) at the anode ( $z = 0$ ) yields

$$\iota_1(0) = 1, \quad \iota_2(0) = 0, \quad \iota_3(0) = 0, \quad \dots \quad (5.25)$$



The boundary condition (5.3) at the cathode ( $z = L$ ) most conveniently is evaluated with the help of the global conservation law (5.6). Taking into account that  $L_\gamma$  is independent of  $j$ , the expanded form reads

$$O(j^0) : \quad \alpha L = L_\gamma, \quad (5.26)$$

$$O(j^1) : \quad \int_0^L \mathcal{E}_1(z) dz = 0, \quad (5.27)$$

$$O(j^2) : \quad \int_0^L \left( \alpha' \mathcal{E}_2(z) + \alpha'' \frac{\mathcal{E}_1^2(z)}{2} \right) dz = 0, \quad (5.28)$$

$$O(j^3) : \quad \int_0^L \left( \alpha' \mathcal{E}_3 + \alpha'' \mathcal{E}_1 \mathcal{E}_2 + \alpha''' \frac{\mathcal{E}_1^3}{3!} \right) dz = 0, \\ \dots \quad (5.29)$$

where the first equation (5.26) reproduces the ignition condition (5.9). Finally, the potential  $u$  from (5.5) is

$$u = u_T(L, \gamma) + j \int_0^L \mathcal{E}_1(z) dz + j^2 \int_0^L \mathcal{E}_2(z) dz \\ + j^3 \int_0^L \mathcal{E}_3(z) dz + \dots \quad (5.30)$$

The lowest order  $u_T(L, \gamma)$  reproduces the Paschen curve (5.10). Eq. (5.27) reveals immediately that the order  $j^1$  in  $u$  has to be absent. For the order  $j^2$  in (5.30), the function  $\mathcal{E}_1(z)$  has to be calculated. First,

$$\iota_1(z) = e^{-\alpha z} \quad (5.31)$$

is the solution of (5.20) and (5.25).  $\iota_1(z)$  has to be inserted into (5.23) which now can be solved analytically up to a constant of integration. This constant is determined by (5.27). The result is

$$\mathcal{E}_1(z) = \frac{\alpha z - \frac{L_\gamma}{2} + (1 + \mu) \left( e^{-\alpha z} - \frac{1 - e^{-L_\gamma}}{L_\gamma} \right)}{\alpha \mu \mathcal{E}_T}. \quad (5.32)$$

For the contribution in order  $j^2$  to the potential, the calculation of  $\mathcal{E}_1$  is sufficient since with the help of (5.28):

$$\int_0^L \mathcal{E}_2(z) dz = - \frac{\alpha''}{2 \alpha'} \int_0^L \mathcal{E}_1^2(z) dz = - \frac{\alpha''}{2 \alpha'} \frac{F(\gamma, \mu)}{\alpha^3 \mu^2 \mathcal{E}_T^2},$$

with the function

$$F(\gamma, \mu) = \frac{L_\gamma^3}{12} + (1 + \mu) (2 - L_\gamma - 2e^{-L_\gamma} - L_\gamma e^{-L_\gamma}) \\ + (1 + \mu)^2 \left( \frac{1 - e^{-2L_\gamma}}{2} - \frac{(1 - e^{-L_\gamma})^2}{L_\gamma} \right). \quad (5.33)$$

The function is plotted in Fig. 5.1. Within the interesting parameter regime, it depends strongly on  $\gamma$  and invisibly on  $\mu$ . Here we use the parameter range for  $\gamma$  suggested by [29] and the maximal mobility ratio  $\mu = \mu_+/\mu_e = 0.0095$  is reached for the lightest molecules, namely hydrogen.

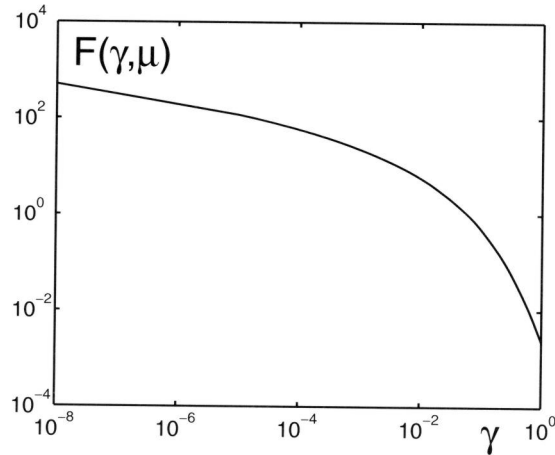


Figure 5.1: Plot of  $F(\gamma, \mu)$  as a function of  $\gamma$  in a double-logarithmic plot. The dependence on  $\mu$  for realistic values  $0 \leq \mu \leq 0.0095$  is too weak to be visible in the plot. However,  $F(\gamma, \mu)$  varies over almost 4 orders of magnitude as a function of  $\gamma$ .

The small current expansion of the current-voltage-characteristics is in this approximation

$$u = u_T - \left(\frac{j}{\mu}\right)^2 \frac{\mathcal{E}_T \alpha''}{2 \alpha'} \frac{F(\gamma, \mu)}{(\alpha \mathcal{E}_T)^3} + O(j^3). \quad (5.34)$$

The range of validity of this expansion can be easily estimated by inserting (5.32) into (5.16): the correction to the field due to the current should not exceed half of the Townsend field, so

$$j \lesssim \frac{\mathcal{E}_T}{2 \max_z |\mathcal{E}_1(z)|} \stackrel{\gamma \leq 1}{\approx} \frac{\mathcal{E}_T}{2 \mathcal{E}_1(L)} \stackrel{L \gamma \gg 1}{\approx} \frac{\mu \mathcal{E}_T^2}{L}. \quad (5.35)$$

In view of the very good fit of this expansion with our numerical results to be presented below in Fig. 5.8, and in view of the interesting bending structure of the numerically derived current-voltage characteristics in Fig. 5.11 below, it seemed promising to calculate the next term of the expansion of order  $j^3$

$$u = u_T - \left(\frac{j}{\mu}\right)^2 \frac{\mathcal{E}_T \alpha''}{2 \alpha'} \frac{F(\gamma, \mu)}{(\alpha \mathcal{E}_T)^3} + \left(\frac{j}{\mu}\right)^3 f_3 + O(j^4). \quad (5.36)$$

The function  $f_3$  can also be calculated fully analytically and along the same lines: first  $\nu_2(z)$  is derived from (5.21) and (5.25) and inserted into the o.d.e. (5.24) for  $\mathcal{E}_2(z)$ . The equation is solved, and the constant of integration is determined by (5.28). Then  $\int_0^L \mathcal{E}_3(z) dz$  is derived from (5.29) and the explicit expressions for  $\mathcal{E}_1(z)$  and  $\mathcal{E}_2(z)$  and inserted into (5.30). However, the result of this calculation is still considerably longer than (5.33) and does not show any simple structure. We therefore will not give the explicit form here. Rather, we summarize essential steps of the calculation in more detail in Appendix B. The final steps are done by computer algebra (mathematica). Some of the results for  $f_3$  are shown in Fig. 5.8 and compared with numerical solutions of the full problem (5.1) – (5.5).

### 5.3.4 Discussion of the result

In order to compare our systematic second order expansion with earlier work [13, 29], it is useful to rewrite equation (5.34) in the following way:

$$u = u_T - A_{SE} \bar{j}^2 + O(\bar{j}^3), \quad (5.37)$$

$$A_{SE} = \frac{\mathcal{E}_T \alpha''}{2 \alpha'} \frac{F(\gamma, \mu)}{(\alpha \mathcal{E}_T)^3}, \quad (5.38)$$

where the current  $j$  is rescaled with the mobility ratio as  $\bar{j} = j/\mu$ .

The result agrees qualitatively with the one given by Raizer [29] and Engel and Steenbeck [13]. In particular, the leading order correction is also of order  $\alpha''(j/\mu)^2$ . However, the explicit coefficient of  $j^2$  differs: while the coefficient  $A$  in [13, 29] does not depend on  $\gamma$  at all, we find that the dependence on  $\gamma$  exists. In fact,  $F$  is proportional to  $L_\gamma^3$  in leading order, and the plot of  $F$  in Fig. 5.1 clearly indicates that within the relevant range of  $10^{-6} \leq \gamma \leq 10^0$ , this coefficient varies by almost five orders of magnitude. On the other hand, the denominator  $(\alpha \mathcal{E}_T)^3$  in (5.38) has in leading order the same strong dependence on  $\gamma$ , since

$$\frac{1}{(\alpha \mathcal{E}_T)^3} = \left( \frac{L}{L_\gamma} \ln(L/L_\gamma) \right)^3, \quad (5.39)$$

according to the Townsend breakdown criterion  $\alpha L = L_\gamma$ , cf. (5.9)–(5.11). Therefore the leading order dependence on  $L_\gamma^3$  of the coefficient of  $\bar{j}^2$  in (5.37) is cancelled and replaced by a dependence on  $L^3$ , while the term with  $\alpha''$  has the classical explicit form

$$\frac{\mathcal{E}_T \alpha''}{2 \alpha'} = \frac{1 - 2\mathcal{E}_T}{2\mathcal{E}_T} = \frac{\ln(L/L_\gamma) - 2}{2}. \quad (5.40)$$

In [13, 29], another small current expansion was derived from (4.1)–(4.4), assuming  $n_+ \gg n_e$  and  $n_+(x) \approx \text{const}$ . This approximation was criticized in [85], since it is in contradiction with the boundary condition that there are no ions at the anode — however, for very small  $\gamma$ , it is a good approximation in a large

part of the gap. The resulting equations (8.8) and (8.10) from [29] read in the notation of the present thesis

$$U = U_T - \frac{U_T}{48} \frac{1 - 2\mathcal{E}_T}{2\mathcal{E}_T} \left( \frac{J}{J_L} \right)^2, \quad (5.41)$$

$$J_L = \frac{\epsilon_0 \mu + U_T^2}{2d^3}. \quad (5.42)$$

(Here a misprint in [29] was corrected, namely the missing factor  $U_T$  in the coefficient of  $J^2$  in (5.41) is added), and the factor  $1/(8\pi)$  in (8.8) is substituted by  $\epsilon_0/2$  in (5.42), since we here write the Poisson equation (4.3) in MKS units rather than in Gaussian units, cf. (8.6) in [29].)

In (5.41), the physical current density  $J$  is compared to  $J_L$ .  $J_L$  is the current density where deviations from the Townsend limit through space charges start to occur; it explicitly depends on  $\gamma$  through  $U_T$  (5.10).

Comparison of our results (SE) (5.37) and Engel/Raizer (ER) (5.41) show that the coefficients  $A_{SE,ER}$  in the expansion (5.37) are related like

$$A_{SE} = A_{ER} \frac{12 F(\gamma, \mu)}{L_\gamma^3}, \quad A_{ER} = \frac{1 - 2\mathcal{E}_T}{2\mathcal{E}_T} \frac{L^3}{12 \mathcal{E}_T^3}. \quad (5.43)$$

The coefficients  $A_{SE}$  and  $A_{ER}$  depend in the same way on  $L$ , and they are essentially independent of  $\mu$  for realistic values of  $\mu$ . Therefore the ratio  $A_{SE}/A_{ER}$  depends on  $\gamma$  as shown in Fig. 5.2. For  $\gamma \rightarrow 0$ , the ratio tends to unity. For a large range of  $\gamma$  values, the deviation is not too large, approaching a factor 0.44 for  $\gamma = 10^{-1}$ .

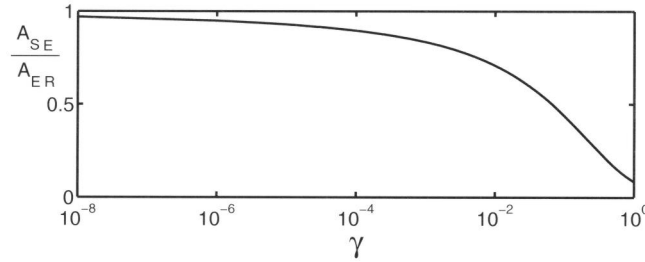


Figure 5.2: The ratio of the coefficients  $A_{SE}/A_{ER}$  in the small current expansions derived here and by Engel/Raizer as a function of  $\gamma$ .

In Fig. 5.3, we show that the factor  $A_{SE}$  indeed strongly depends on  $\gamma$  by plotting

$$\frac{24 A_{SE}(L, \gamma)}{L^3 \ln^4 L} = \frac{A_{SE}}{A_{ER}} \left( 1 - \frac{2 + \ln L_\gamma}{\ln L} \right) \left( 1 - \frac{\ln L_\gamma}{\ln L} \right)^3 \quad (5.44)$$

as a function of  $\gamma$  for a number of gap lengths  $L$ . In the limit of infinite gap length  $\ln L \rightarrow \infty$ , this ratio should reach the ratio  $A_{SE}/A_{ER}$ . However, it should

be noted that considering long gaps is not physical anymore, since in that case a Townsend discharge would not occur, but rather streamer breakdown would take place.

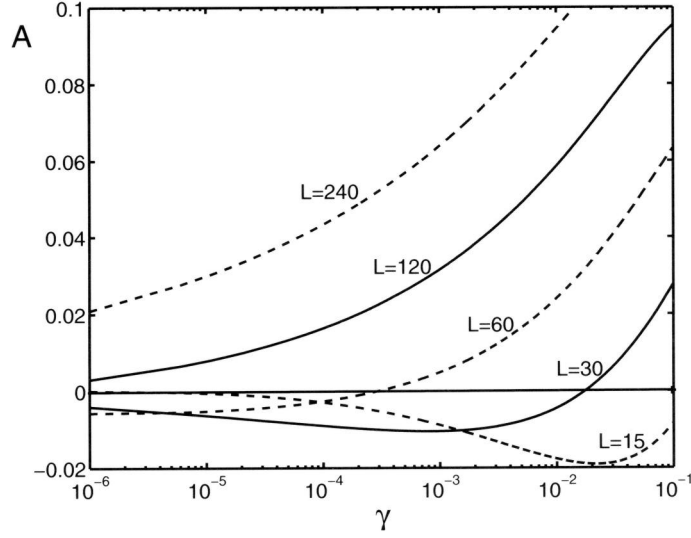


Figure 5.3: The normalized coefficient  $A = 24 A_{SE}/(L^3 \ln^4 L)$  as a function of  $\gamma$  for gap lengths  $L = A p d = 15, 30, 60, 120, 240$  (dashed and solid lines with labels).

The strong dependence of  $A_{SE}$  or  $A_{ER}$  on  $\gamma$  for a given short gap length  $L$  means that we can obtain both negative and positive differential resistance  $dU/dJ$  close to the Townsend limit for the same gap length. Therefore the choice of  $\gamma$  is important since it can change the differential conductivity and therefore the stability of a Townsend discharge in a short gap.

Translating back from dimensionless to physical units, the result reads

$$U(J) = U_T - \left( \frac{J}{\epsilon_0 \mu_+} \right)^2 \frac{E \partial_E^2 \bar{\alpha} \Big|_{E_T}}{2 \partial_E \bar{\alpha} \Big|_{E_T}} \frac{F(\gamma, \mu)}{(\bar{\alpha} E_T)^3} + \left( \frac{J}{\epsilon_0 \mu_+} \right)^3 \frac{f_3}{(E_0^2 A p)^3} + \dots,$$

with the dimensionless coefficient

$$\frac{E \partial_E^2 \bar{\alpha} \Big|_{E_T}}{2 \partial_E \bar{\alpha} \Big|_{E_T}} = \frac{\mathcal{E}_T \alpha''}{2 \alpha'} = \frac{s E_0^s - (s+1) E_T^s}{2 E_T^s}. \quad (5.45)$$

The coefficient of  $J^2$  changes sign for  $\mathcal{E}_T = E_T/E_0 = [s/(s+1)]^{1/s}$ . With the help of (5.11), this transition at  $\alpha'' = 0$  can be located on the Paschen curve; it

occurs at

$$L_{crit} = L_\gamma e^{1+1/s} . \quad (5.46)$$

This is always on the right branch of the Paschen curve, since the minimum is at  $L = L_\gamma e^{1/s}$ .

Our  $\gamma$ -dependent analytical result also excellently fits our numerical solutions, as we will show in the next section.

## 5.4 Numerical solutions

We now discuss our numerical results for the voltage  $u$  as a function of total current  $j$ , secondary emission coefficient  $\gamma$ , mobility ratio  $\mu$  and system size  $L$ , as resulting from Eqs. (5.1)–(5.5). We will work with the Townsend approximation  $\alpha(\mathcal{E}) = e^{-1/|\mathcal{E}|}$  (4.25) with  $s = 1$  as the standard case [29].

### 5.4.1 The numerical method

In Appendix A, we showed that the solution  $u = u(j)$  is unique for fixed  $\gamma$ ,  $\mu$  and  $L$ , and we proved the useful property that the system size  $L$  is a monotonically decreasing function of the electric field  $\mathcal{E}(0)$  at the anode,  $dL/d\mathcal{E}(0) < 0$  (5.50), for fixed  $\gamma$ ,  $\mu$  and  $j$ . The second observation lays the basis for our numerical iteration procedure:

First the two o.d.e.'s (5.1), (5.2) are integrated from  $z = 0$  with the known initial value  $j_e(0) = j$  and some guessed initial value  $\mathcal{E}(0)$  towards larger  $z$ . The equations are integrated until for some  $z = \bar{z}$ , we find the value  $j_e(\bar{z}) = j e^{-L\gamma}$  that should be assumed at the fixed system size  $z = L$ . If  $\bar{z} > L$ , a larger value of  $\mathcal{E}(0)$  is chosen for the next iteration step, and if  $\bar{z} < L$ , a smaller  $\mathcal{E}(0)$  where a linear interpolation of  $d\bar{z}/d\mathcal{E}(0)$  is used. This iteration loop is continued until the boundary condition (5.3) at  $L$  is obeyed with sufficient accuracy. The potential  $\phi(z)$  is integrated together with  $j_e(z)$  and  $\mathcal{E}(z)$  by adding the third o.d.e.  $\partial_z \phi = -\mathcal{E}$  [86]. The voltage  $u$  over the system is  $u = \phi(0) - \phi(L)$ .

For the numerical integration of the o.d.e.'s, we used the `lsodar.f` routine of the `ODEPACK` package from the free-ware site `netlib.org`. It integrates initial value problems for sets of first order o.d.e.'s and chooses automatically the appropriate numerical method for stiff or non-stiff systems. At the same time, it locates the roots of any specified function. We defined this function as  $j_e(z) - j e^{-L\gamma}$  which returns the value  $\bar{z}$  for the next iteration loop with high precision.

### 5.4.2 Parameters $L$ , $\gamma$ and $\mu$ , and $j/\mu$ -scaling

The problem depends on the following parameters: the first one is the system size  $L$  which is proportional to  $pd$  in physical units. It can take arbitrary values; we explore a continuous range of  $L$  on both the left and the right branch of the Paschen curve.

The second parameter is the secondary emission coefficient  $\gamma$  which is determined by both the gas and the cathode surface. Increasing  $\gamma$  decreases the

minimum breakdown voltage which is at  $eL_\gamma$  as discussed after Eq. (5.46). This mechanism can be used for improving performance in technical applications like plasma display panels [87]. According to [29],  $\gamma$  can take values between  $10^{-6}$  and  $10^{-1}$ , in extreme cases even larger. We show results either for the two extreme cases  $10^{-6}$  and  $10^{-1}$ , or we show one representative result for  $\gamma = 10^{-2}$ .

The third parameter is the mobility ratio  $\mu = \mu_+/\mu_e$  of the charged species. Since ions are much heavier than electrons,  $\mu$  is always much smaller than 1. The largest value of  $\mu = 0.0095$  [29] is reached for the lightest molecules, namely hydrogen. As a standard, we use the value  $\mu = 0.0035$  for nitrogen.

The functional form of the defining equations (5.1)-(5.4) and of the small current expansion (5.36) suggest that  $u$  in leading order does not depend on  $j$  and  $\mu$  separately, but only on the scaling variable  $j/\mu$  and on the factor  $(1 + \mu) \approx 1$ . This observation motivates our choice of the variable  $j/\mu$  in the following figures. However, Fig. 5.9 will show that for large  $j/\mu$  in the abnormal glow regime and for large systems  $L$ , there is some small  $\mu$ -dependent correction to this scaling behavior. Reconsidering (5.1)-(5.4), this means that the factor  $(1 + \mu)$  can not simply be equated with 1 even for  $\mu < 10^{-2}$ , but yields some correction. In physical terms, the substitution of  $(1 + \mu)$  by 1 means the elimination of the field increase in the anode fall region, and we conclude that in large systems in the glow regime, the anode fall yields some small contribution to the current-voltage-characteristics.

### 5.4.3 General features of the current-voltage-characteristics

We now give an overview over our numerical results in the full parameter regime of the current-voltage-characteristics  $u(j)$  from Townsend up to abnormal glow discharge as a function of rescaled current  $j/\mu$ , system size  $L$  and secondary emission coefficient  $\gamma$ . In Figs. 5.4 and 5.5, we plot  $u$  as a function of  $j/\mu$  and  $L$  for  $\gamma = 10^{-6}$  and  $\gamma = 10^{-1}$ , respectively. The plots follow the style of an experimental plot in [80], which is reproduced as Fig. 1 in [22]. To the best of our knowledge, our Figs. 5.4 and 5.5 for the first time present numerical results in the same style.

Comparing the two figures for different  $\gamma$ , it can be noted that on the one hand, the shapes look qualitatively similar, while on the other hand, the actual parameter regimes of potentials, currents and system sizes vary by an order of magnitude or more. Let us now consider the common features.

In the limit of small current  $j$  (i.e., in the foreground of the figures), the curves saturate to a plateau value which actually reproduces the Paschen curve  $u = u_T(L, \gamma)$  from Eq. (5.10).

Following  $u = u(j)$  along a line of fixed system size  $L$ , we get the current-voltage-characteristics for this particular system characterized by the two parameters  $L$  and  $\gamma$ . For these curves  $u = u(j)$ , two features can be noted.

First, for larger  $L$ , the voltage  $u$  first decreases for increasing current  $j$ . This is the familiar Townsend-to-glow-transition with negative differential conductivity. For larger  $j$ , the voltage  $u$  increases again towards the regime of abnormal glow. However, in the minimum of the potential, there is no plateau in con-

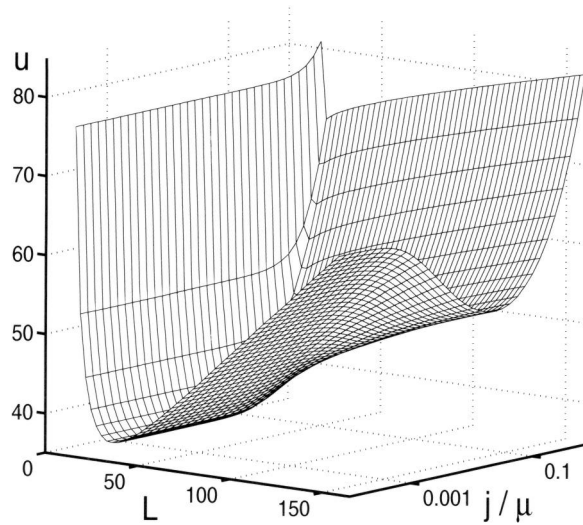


Figure 5.4:  $u$  as a function of  $j/\mu$  and  $L$  for the small secondary emission coefficient  $\gamma = 10^{-6}$ . The parameter range is  $3 \cdot 10^{-7}/\mu \leq j/\mu \leq 5 \cdot 10^{-3}/\mu$  for  $\mu = 0.0035$  and  $17.3 \leq L \leq 160$ .

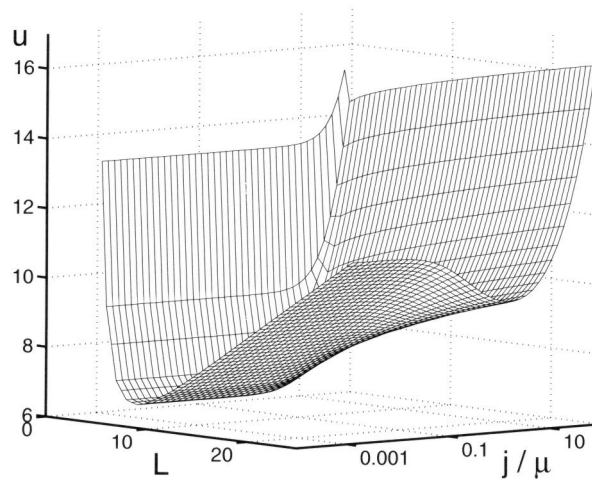


Figure 5.5: Plot as in Fig. 5.4, but now for  $\gamma = 10^{-1}$ . The parameter range is  $10^{-6}/\mu \leq j/\mu \leq 7 \cdot 10^{-2}/\mu$  for  $\mu = 0.0035$  and  $3 \leq L \leq 28$ .



trast to experimental plots. This is because we solve the purely one-dimensional system without the possibility of a lateral growth of the glow discharge column.

Second, for smaller values of  $L$ , in particular, when starting from the left branch of the Paschen curve, the voltage does not decrease for increasing current, but it increases immediately. We will discuss this different bifurcation structure in more detail at the end of this section.

#### 5.4.4 Spatial profiles

It is instructive to study the spatial profiles of electron current  $j_e(z)$  and field  $\mathcal{E}(z)$  for different system sizes. In Figs. 5.6 and 5.7, we plot such profiles for  $L = eL_\gamma$  and for  $L = e^3L_\gamma = eL_{crit}$ . The smaller system size  $eL_\gamma$  coincides with the minimum of the Paschen curve, while  $L_{crit} = e^2L_\gamma$  (5.46) is the system size where  $\alpha''$  in (5.36) changes sign. So for  $L < L_{crit}$  the voltage increases initially in the small current expansion around the Townsend limit, while for  $L > L_{crit}$  it decreases.

Note that in contrast to previous plots, e.g., in [29], our cathode is on the right hand site at  $z = L$ , because we found it more convenient to work with a positive field  $\mathcal{E}$ . The electron current is normalized by the total current.

In each plot, the profiles for the two smallest current values are well described by the small current expansion from Section 5.3. This is in agreement with the range of validity of these expansions of  $j/\mu \lesssim 0.08$  for  $L = eL_\gamma = L_{crit}/e$  or of  $j/\mu \lesssim 1.3 \cdot 10^{-3}$  for  $L = eL_{crit}$ , resp., estimated according to (5.35).

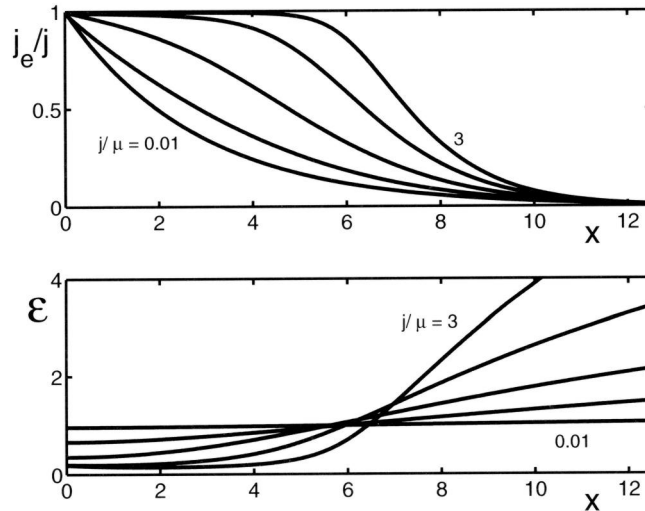


Figure 5.6: Spatial profiles  $j_e(z)/j$  and  $\mathcal{E}(z)$  for system size  $L = eL_\gamma$  at the minimum of the Paschen curve. Plotted are curves for  $j/\mu = 0.01, 0.1, 0.3, 1, 3$ . Other parameters:  $\gamma = 0.01, \mu = 0.0035$ .

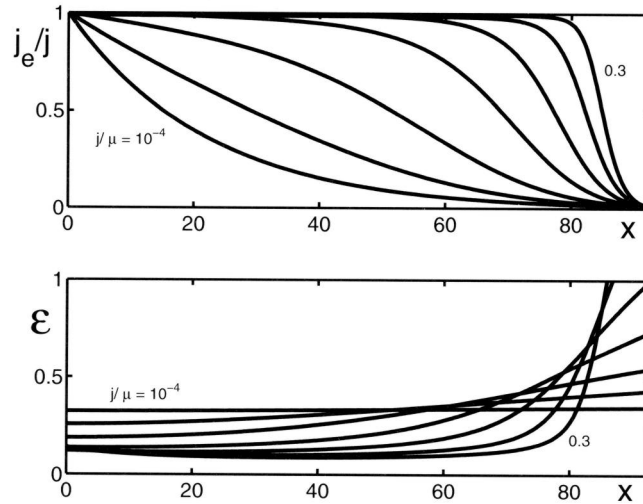


Figure 5.7: The same as in the previous figure, but now for the larger system size  $L = e^3 L_\gamma$ . The current now explores the smaller values  $j/\mu = 10^{-4}, 10^{-3}, 3 \cdot 10^{-3}, 0.01, 0.03, 0.1, 0.3$ .

For larger currents, a separation into a resistive column on the left and cathode fall on the right becomes pronounced. While in the smaller system, both regions take about equal parts, in the larger system, the cathode fall takes only a small part of the volume on the right hand side.

#### 5.4.5 Comparison of numerical and analytical results

Let us now compare the current-voltage-characteristics corresponding with these profiles with our analytical results from Section 5.3. In Fig. 5.8, the numerical results for  $u(j)$  are plotted as a thick solid line, and the analytical expansions (5.34) and (5.36) up to second or third order in  $j/\mu$  as thin solid and dashed lines, respectively. For the calculation of the third order, the procedure described in Appendix A has been followed. Fig. 5.8 shows that in particular the expansion up to order  $(j/\mu)^3$  gives a very good agreement at least within the range of validity of  $j/\mu \lesssim 0.08$  or  $1.3 \cdot 10^{-3}$ , resp., according to (5.35).

#### 5.4.6 Corrections to $j/\mu$ -scaling

Fig. 5.9 shows the current-voltage-characteristics for the same two systems, but now up to larger values of the current than in Fig. 5.8. Actually, the same current range is explored in each system as in the corresponding Figs. 5.6 and 5.7.

In addition, in Fig. 5.9 we test the  $j/\mu$ -scaling by plotting  $u$  as a function of

$j/\mu$  within the physical range of  $\mu$ -values, including the limit of  $\mu = 0$ . It can be noted that for short systems or small currents, the  $\mu$ -correction is negligible; this means that  $(1+\mu)$  can be replaced by 1 in Eq. (5.2) without visible consequences. In contrast, for large systems and large currents, there is a small, but visible  $\mu$ -correction to the dominant  $j/\mu$ -scaling.

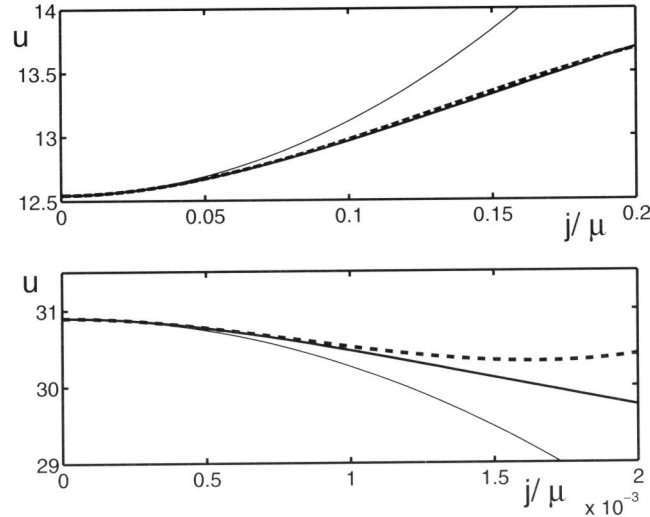


Figure 5.8:  $u(j)$  for the systems from Figs. 5.6 and 5.7 in the small current limit: upper plot  $L = eL_\gamma$ , lower plot  $L = e^3L_\gamma$ , both with  $\gamma = 0.01$ . Numerical result (thick solid line), analytical result (5.34) up to second order in  $j/\mu$  (thin solid line) and analytical result (5.36) up to third order in  $j/\mu$  (dashed line).

### 5.4.7 Discussion of bifurcation structures

We now set the final step in the quantitative understanding of the current-voltage-characteristics at the transition from Townsend to glow discharge. We characterize the transitions as subcritical, mixed or supercritical and locate them in parameter space.

Fig. 5.10 gives an overview over the different behaviors for  $\gamma = 0.01$ . It corresponds to different  $L$ -sections of plots as in Figs. 5.4 and 5.5, but now with  $j/\mu$  plotted on a linear rather than a logarithmic scale. For the terminology of sub- or supercritical bifurcations, it should be noted that  $j/\mu = 0$  is a solution for arbitrary  $u$ . So the complete  $u$ -axis is a solution, too.

In the case of  $L = 0.85L_{crit}$ , there is a pure forward or supercritical bifurcation:  $u$  increases monotonically as  $j/\mu$  increases. In contrast, for  $L = 1.05L_{crit}$ , the bifurcation is purely subcritical: with increasing  $j/\mu$ , the voltage first decreases, and eventually it increases again. This subcritical behavior continues

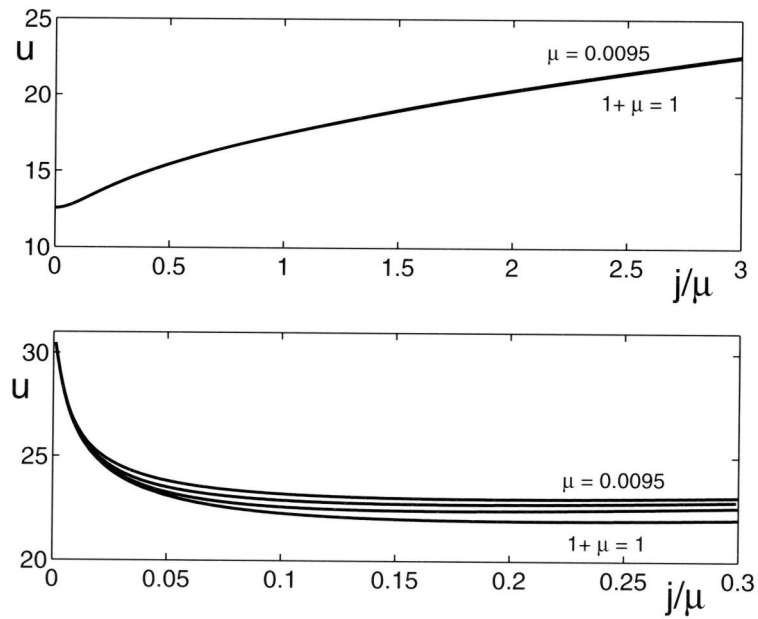


Figure 5.9: Current-voltage characteristics for the same two systems as in Figs. 5.6, 5.7, and 5.8 (upper plot  $L = eL_\gamma$ , lower plot  $L = e^3L_\gamma$ ), but now for a larger current range than in Fig. 5.8. Furthermore, besides the curves for the nitrogen value for the mobility ratio  $\mu = 0.0035$ , also the curves for  $\mu = 0.0095$  (hydrogen),  $\mu = 0.001$  and the limiting value  $\mu = 0$  are shown.

down to  $L = L_{crit} = L_\gamma e^2$  where  $\alpha''$  changes sign. So indeed, the sign change of  $\alpha''$  in the small current expansion determines the transition from subcritical to some other behavior. However, for  $L < L_{crit}$ , the system does not immediately enter the supercritical regime, but some unexpected ‘mixed’ behavior can be seen: for increasing  $j/\mu$ , the voltage  $u$  first increases, then it decreases and then it increases again. We distinguish ‘mix<sub>I</sub>’ where the voltage minimum at finite  $j/\mu$  is smaller than the Townsend voltage, and ‘mix<sub>II</sub>’ where it is larger.

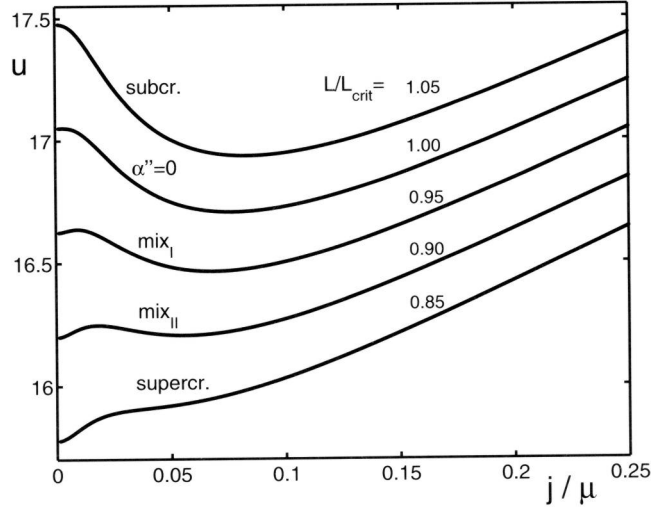


Figure 5.10: The current-voltage-characteristics for fixed parameters  $\gamma = 0.01$  and  $\mu = 0.0035$  and different system sizes, measured in multiples of  $L_{crit} = L_\gamma e^2$ . Shown are all possible bifurcation structures from supercritical up to the familiar subcritical case for various values of  $L$ .

Fig. 5.11 shows a zoom into Fig. 5.10: a smaller range of current and of system sizes. The form of an upwards parabola of the order  $(j/\mu)^2$  next to the  $u$ -axis is well described by the analytical small current expansion of Section 5.3. However, in contrast to initial hopes, the turn-over of the curves at  $j/\mu \approx 0.02$  is not covered by the small current expansion up to order  $(j/\mu)^3$  whose coefficient even changes sign within the parameter range of Fig. 5.11. In fact, the range of validity of the expansion breaks down at  $j/\mu \leq 0.017$ , just briefly before the first interesting bending structure in the characteristics.

Finally, in Fig. 5.12, the bifurcation behavior in the full parameter range of  $\gamma$  is explored. The transition from subcritical to mix<sub>I</sub> always takes place when  $\alpha''$  changes sign, i.e., at system size  $L_{crit} = L_\gamma e^2$ . The transitions from mix<sub>I</sub> to mix<sub>II</sub> and then further to supercritical occur at smaller relative system sizes  $L/L_{crit}$  when the secondary emission coefficient  $\gamma$  is smaller. All transitions occur on the right branch of the Paschen curve, since its minimum is at  $L/L_{crit} = e^{-1} = 0.368$ .

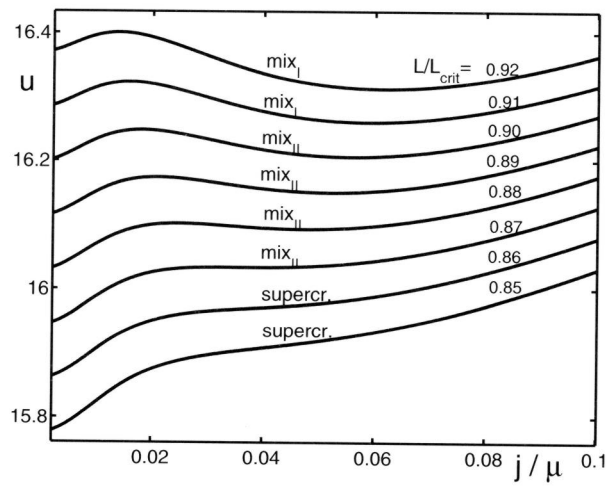


Figure 5.11: Zoom into Fig. 5.10 with smaller values of  $j/\mu$  and system sizes  $L$ . The range of validity of the analytical small current expansion (5.36) is  $j/\mu \leq 0.017$ .

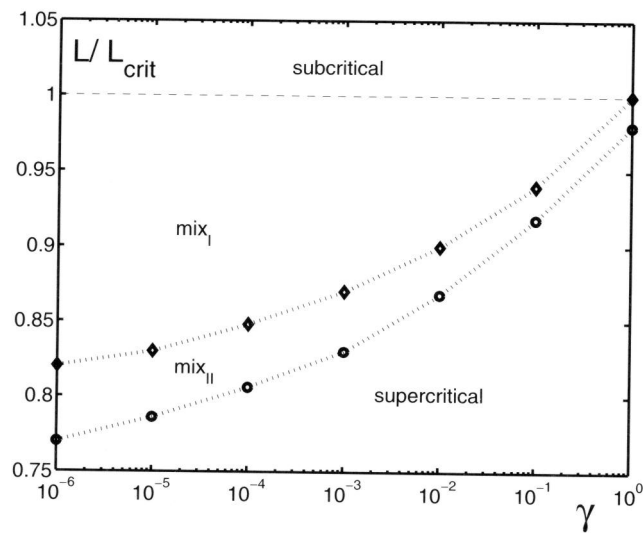


Figure 5.12: Complete overview over the bifurcation behavior of the current-voltage characteristics as a function of secondary emission coefficient  $\gamma$  and system size  $L$ .

## 5.5 Summary and Outlook

We have studied the classical minimal model that creates a Townsend or glow discharge, in one-dimensional approximation. The dimensionless current-voltage characteristics  $u = u(j/\mu)$  depends on essentially only two parameters, the secondary emission coefficient  $\gamma$  and the dimensionless system size  $L \propto pd$ . (With  $j/\mu$ -scaling, the further dependence on the small mobility ratio  $\mu = \mu_+/\mu_e$  is very weak and becomes visible only for long systems in the normal and abnormal glow regime.) Numerically, we have fully explored the bifurcation structure as a function of  $\gamma$  and  $L$ . Besides the familiar subcritical bifurcation structure of long systems, for decreasing system size  $L$ , there is a sequence of current-voltage characteristics, that we have called  $\text{mix}_I$  and  $\text{mix}_{II}$ , before the supercritical transition is reached. This general sequence is the same for all relevant values of  $\gamma$  while the precise lengths where the transitions occur, depend on  $\gamma$ , cf. Fig. 5.12. Analytically, we have calculated the small current expansion about the Townsend limit in a systematic expansion. We found that the term of order  $j/\mu$  is missing, and that the term of order  $(j/\mu)^2$  indeed is proportional to the second derivative of the Townsend coefficient  $\alpha''$  according to the old argument from Engel and Steenbeck [13], but with a different, strongly  $\gamma$ -dependent proportionality constant. We also have calculated the term of order  $(j/\mu)^3$ . These analytical expansions are in very good agreement with our numerical results within their predicted range of validity.

Of course, the study of this minimal model can only be a first step, and it has been suggested to include a number of additional features. First,  $\gamma$  might not be constant; while the dependence  $\gamma = \gamma(I, V)$  [18] on global parameters seems unphysical, the local dependence  $\gamma = \gamma(E/p)$  has been suggested [21] and experimentally tested [88]. Second, the particle mobilities might be field-dependent  $\mu_{\pm} = \mu_{\pm}(E)$ . Third, diffusion was neglected, the approach was fully local, and only one ion type was considered. However, our aim was first to settle the predictions of the classical model in full parameter space as a corner stone and starting point for any future extension that simultaneously also will increase the number of parameters.

The motivation for this work is the impressive variety of spatio-temporal patterns formed in short barrier discharges [8–11, 24, 67–70]. The nonlinear element responsible for the spontaneous pattern formation is believed to be a gas discharge in the parameter range of the present work. Parameter regions with negative differential conductivity (NDC) are generally believed to play a decisive role in the formation of the instabilities. Knowledge about NDC regions and the bifurcation structure in the range of these experiments therefore are a condition for their future investigation, and conversely, properties of the current-voltage characteristics might be deduced from temporal oscillations or current constrictions. These pattern formation processes will be subject of the next chapter.

## 5.A Appendix A

### Uniqueness of the solution of the boundary value problem

Here we prove that the boundary value problem defined by (5.1) – (5.4) for fixed  $j$ ,  $\mu$ ,  $\gamma$  and  $L$  defines a unique solution  $(j_e(z), \mathcal{E}(z))$  and hence a unique potential  $u = \int_0^L \mathcal{E}(z) dz$ . This lays the ground for our analytical as well as for our numerical procedure. We will keep  $j$ ,  $\mu$  and  $\gamma$  fixed within this appendix, and will discuss how  $\mathcal{E}(z)$  is determined by  $L$  and vice versa.

First Eq. (5.1) for  $j_e$  is integrated with initial condition  $j_e(0) = j$  (5.3) and inserted into (5.2):

$$\mu \mathcal{E} \partial_z \mathcal{E} = j \left( 1 - (1 + \mu) e^{-\int_0^z \alpha(\mathcal{E}(z)) dz} \right) \quad (5.47)$$

The boundary condition (5.3) at  $L$  amounts to

$$\int_0^L \alpha(\mathcal{E}(z)) dz = L_\gamma, \quad (5.48)$$

where we assume that

$$\alpha(\mathcal{E}) > 0 \quad \text{and} \quad \partial \alpha / \partial \mathcal{E} > 0 \quad \text{for all } \mathcal{E} > 0. \quad (5.49)$$

An initial condition  $\mathcal{E}(0)$  defines a unique solution  $\mathcal{E}(z)$  of (5.47) and hence a unique system size  $L$  through (5.48). We will show below that  $L$  is a monotonically decreasing function of  $\mathcal{E}(0)$

$$dL/d\mathcal{E}(0) < 0 \quad \text{for fixed } j, \mu, \gamma. \quad (5.50)$$

This statement has two immediate consequences: (i) it shows that  $\mathcal{E}(0)$  and therefore also  $\mathcal{E}(z)$  and  $u$  are uniquely determined by  $L$ ; and (ii) it lays the ground for our numerical iteration procedure where  $\mathcal{E}(0)$  is fixed, and the resulting  $L$  is calculated and compared to the true  $L$ .

Why is statement (5.50) true? Compare two solutions  $\mathcal{E}_{1,2}(z)$  and suppose that  $\mathcal{E}_1(z') > \mathcal{E}_2(z')$  on some interval  $0 \leq z' \leq z$ . Then for the difference, we get from (5.47) that

$$\begin{aligned} & \frac{\mu}{2j(1+\mu)} (\partial_z \mathcal{E}_1^2 - \partial_z \mathcal{E}_2^2) \\ &= e^{-\int_0^z \alpha(\mathcal{E}_2(z)) dz} - e^{-\int_0^z \alpha(\mathcal{E}_1(z)) dz} \geq 0, \end{aligned} \quad (5.51)$$

where the bound  $\dots \geq 0$  is a direct consequence of (5.49). So when  $\mathcal{E}_1$  is above  $\mathcal{E}_2$  on some interval  $0 \leq z' \leq z$ , then at the end of the interval, we have  $\partial_z \mathcal{E}_1^2 > \partial_z \mathcal{E}_2^2$ , and  $\mathcal{E}_1$  stays above  $\mathcal{E}_2$ . As a consequence

$$\mathcal{E}_1(z) > \mathcal{E}_2(z) \quad \text{for all } z \geq 0, \quad \text{if } \mathcal{E}_1(0) > \mathcal{E}_2(0). \quad (5.52)$$

Inserting this into (5.48) and using (5.49), statement (5.50) results.



## 5.B Appendix B

### The correction of $O(j^3)$ about the Townsend limit

We here sketch the essential elements of the calculation of the third term  $j^3$  of the expansion about the Townsend limit: first Eq. (5.21) is integrated. With (5.31) for  $\iota_1$ , (5.32) for  $\mathcal{E}_1$ , and the boundary condition (5.25), we get

$$\iota_2(z) = -\frac{\alpha' e^{-\alpha z}}{\alpha^2 \mu \mathcal{E}_T} \left[ \frac{(\alpha z)^2}{2} + (1 + \mu)(1 - e^{-\alpha z}) - \alpha z \left( \frac{L_\gamma}{2} + (1 + \mu) \frac{1 - e^{-\alpha z}}{L_\gamma} \right) \right] \quad (5.53)$$

This result allows us now to integrate  $\mathcal{E}_2(z)$  in (5.24) with the rather lengthy result

$$\begin{aligned} \mathcal{E}_2(z) = & \frac{1}{2\alpha^2 \mu^2 \mathcal{E}_T^3} \left[ (1 + \mu) \frac{\alpha' \mathcal{E}_T}{\alpha} \cdot \right. \\ & \left. \left\{ -(\alpha z)^2 e^{-\alpha z} + (1 + \mu)(e^{-2\alpha z} - 2e^{-\alpha z}) \right. \right. \\ & \left. \left. + 2 \left( \frac{L_\gamma}{2} - 1 + (1 + \mu) \frac{1 - e^{-L_\gamma}}{L_\gamma} \right) (\alpha z + 1) e^{-\alpha z} \right\} \right. \\ & \left. - \alpha z \left( L_\gamma - \alpha z + 2(1 + \mu) \frac{1 - e^{-L_\gamma}}{L_\gamma} \right) \right. \\ & \left. + 2(1 + \mu) \left( \frac{L_\gamma}{2} + (1 + \mu) \frac{1 - L_\gamma}{L_\gamma} - \alpha z \right) e^{-\alpha z} \right. \\ & \left. - (1 + \mu)^2 e^{-2\alpha z} \right] + C \quad (5.54) \end{aligned}$$

The constant of integration  $C$  is determined through (5.28)

$$\int_0^L \mathcal{E}_2 dz = -\frac{\alpha''}{2\alpha'} \frac{F(\gamma, \mu)}{\alpha^3 \mu^2 \mathcal{E}_T^2}. \quad (5.55)$$

Finally,  $\int_0^L \mathcal{E}_3 dz$  is determined by  $\mathcal{E}_1$  and  $\mathcal{E}_2$  through (5.29) as

$$\int_0^L \mathcal{E}_3 dz = -\frac{\alpha''}{\alpha'} \int_0^L \mathcal{E}_1 \mathcal{E}_2 dz - \frac{\alpha'''}{3! \alpha'} \int_0^L \mathcal{E}_1^3 dz. \quad (5.56)$$

Insertion of the result in Eq. (5.30) yields the third order expansion (5.36) with an explicit expression for the function  $f_3$ .

All integrals can be performed analytically. However, the results are lengthy and exhibit no simplifying structure. Therefore, we rather have performed the remaining integrals by computer algebra. Results are shown in Fig. 5.8.

## Chapter 6

# Oscillatory solutions

As has been explained in Chapter 3, experimentally it is possible to obtain the domain of existence of the homogeneous oscillations in the parameter plane (applied voltage and conductivity of the semiconductor) for fixed values of pressure ( $p$ ) and gas gap width ( $d$ ). The system spontaneously undergoes a transition to temporal oscillations which are spatially homogeneous. This behavior is reproduced by our full time-dependent numerical solutions of the model, including the coexistence of stationary and oscillating solutions in certain parameter regimes. Furthermore, linear stability analysis of the stationary solutions gives a result which is in excellent agreement with numerical predictions. We find semi-quantitative agreement with experiment both for the bifurcation diagram from stationary to oscillating solutions as well as for the amplitude and frequency of the developing limit cycle oscillations. Apart from experimental system (presented in Chapter 3), the results on these homogeneous oscillations apply equally to a planar discharge in series with any resistor with capacitance as shown in Fig. 6.1.

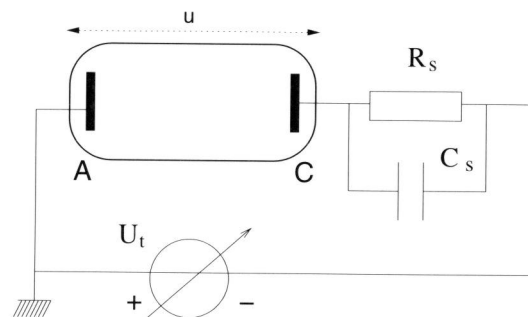


Figure 6.1: The effective electric circuit to which our results on homogeneous oscillations do apply. The semiconductor with its resistivity and capacitance is replaced by resistor  $R_s$  and condenser  $C_s$ .

## 6.1 Numerical solutions of the dynamics

In this section, the dynamical model in 1D (Chapter 4) is solved numerically and the results are compared with experiments. The section is divided into 5 subsections. In the first one, we discuss physical parameters and numerical details in the second. In the third, qualitative features of experimental and numerical system are compared like the bistability between stationary and oscillating state. In the next subsection, a quantitative comparison between theory and experiment is performed, and the dependence of amplitude and frequency of the oscillation as a function of  $u_t$  and  $1/R_s$  is determined numerically. Finally, in the last one, the mechanism of the oscillations is explained and a comparison with other model reductions given.

### 6.1.1 Physical parameters

In the experiments [11,12] from Chapter 3, nitrogen at a pressure of 40 mbar was used in gaps with widths of 0.5 or 1 mm. The article [11] contains mainly data for the 0.5 mm gap, while the Ph.D. thesis [12] also contains more data for 1 mm. The gas discharge was coupled to a semiconductor layer of GaAs with a width of  $d_s = 1.5$  mm and a dielectricity constant  $\epsilon_s = 13.1$ . Through photosensitive doping, the conductivity of the semiconductor layer could be increased by about an order of magnitude; the dark conductivity was  $\sigma_s = 3.2 \cdot 10^{-8} (\Omega\text{cm})^{-1}$ . For the discharge gap of 0.5 mm width, voltages in the range of 500 to 600 V were used; for the gap of 1 mm width, the applied voltages were in the range of 580 to 740 V.

Of course, the predictive power of the theory depends on the model approximations as well as on the chosen parameters. Our simple classical model will not give fully quantitative agreement. On the other hand, its simple structure and few parameters give a chance of physical understanding and control.

For the gas discharge, we used the ion mobility  $\mu_+ = 23.33 \text{ cm}^2/\text{Vs}$  and electron mobility  $\mu_e = 6666.6 \text{ cm}^2/\text{Vs}$ . For  $\alpha_0 = Ap = [27.78\mu\text{m}]^{-1}$  and  $E_0 = Bp = 10.26 \text{ kV/cm}$ , the value from [29] was used. The gap widths of  $d = 0.5$  and 1 mm then correspond to dimensionless gap widths  $L = 18$  and 36. For  $\gamma$ , we used the value 0.08 determined from experimental Paschen curves in [12] as explained in Appendix of Chapter 3. It should be noted that our classical model predicts that the Paschen curves (i.e., the breakdown voltage  $U$  of the gas discharge as a function of pressure times gap width  $pd$ ) for different system sizes should be indistinguishable. In practice, they do not precisely fall on top of each other.

It is interesting to note how sensitive the theoretical results are to small changes of the secondary emission coefficient  $\gamma$ , in particular, for the short gap with  $L = 18$ . This is illustrated in Fig. 6.2. The upper three solid lines show the shape of the current voltage characteristics for  $\gamma = 0.08$  and gap widths of  $L = 17, 17.5$  and 18. As discussed in more detail in [85,89], the characteristics can be supercritical ( $L = 17$ , positive differential conductivity for all values of the current  $j$ ),  $\text{mix}_{\text{II}}$  ( $L = 17.5$ , Townsend breakdown voltage lower than the

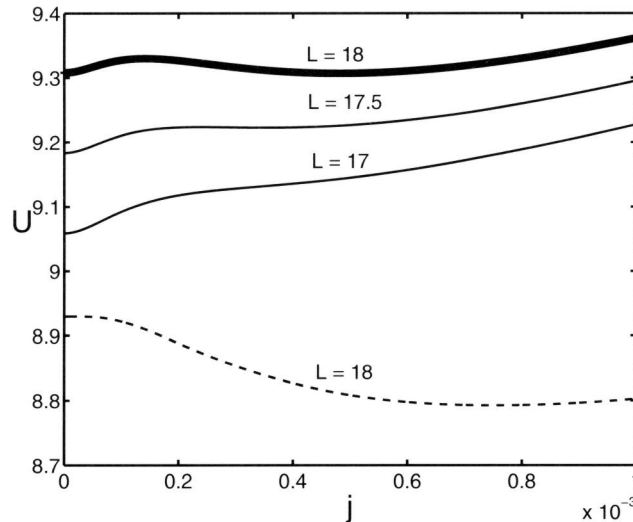


Figure 6.2: Current-voltage characteristics for  $\gamma = 0.08$  (solid lines) and  $\gamma = 0.1$  (dashed line) for the dimensionless gap widths  $L$  as indicated in the figure.

local voltage minimum for  $j \neq 0$ ) or  $\text{mix}_I$  ( $L = 18$ , Townsend breakdown voltage higher than the local voltage minimum for  $j \neq 0$ ). The dashed line shows the characteristics for  $L = 18$  and  $\gamma = 0.1$ .  $u$  then overall is considerably lower and the characteristics is fully subcritical, i.e., the voltage has only one minimum as function of current  $j$  and this occurs for a value  $j \neq 0$ . This subcritical behavior corresponds to the classical textbook case where the characteristics bends down from the Townsend breakdown voltage towards a voltage minimum in the glow discharge regime — as we have discussed in [85, 89] in detail, this requires a sufficiently large system size. For  $\gamma = 0.08$ , the characteristics becomes subcritical for system size  $L > L_{crit} = e^2 \ln [(1 + \gamma)/\gamma] = 19.2$  while the transition to supercritical behavior is determined numerically [85] to the value of  $L = 17.2$ .

Data on the coefficient  $\gamma$  of secondary electron emission are relatively scarce, so it is quite common [90] to use it as an adjustable parameter as we do. The tabulated data for  $\alpha_0 = Ap$  and  $E_0 = Bp$  from [29] together with the Paschen curve for  $d = 0.5$  mm from [12] would suggest  $\gamma = 0.03$ , but that would mean that the characteristics would be supercritical up to  $L = 24.9$ , then it would develop some regime with negative differential conductivity, and it would become subcritical only for  $L > L_{crit}(\gamma = 0.03) = 26.1$ .

We conclude that the case of a gap with width of 0.5 mm (corresponding to  $L = 18$ ) is so sensitive to the not very well known parameter  $\gamma$  that an analysis of the experimental data would be rather uncertain. Furthermore, the approximation of purely local interactions becomes worse in shorter gaps. Finally, the electric fields in short discharges are higher and vary more; therefore

the assumption that  $\gamma$  does not depend on  $E$  becomes more restrictive. For this reason, we chose to analyze the system with gap width 1 mm ( $L = 36$ ).

To summarize, the following intrinsic scales

$$\begin{aligned} r_0 &\approx 27.78 \mu\text{m} & , & & t_0 &\approx 40.6 \cdot 10^{-12} \text{ s}, \\ q_0 &\approx 32.69 \cdot 10^{-8} \text{ As/cm}^3 & , & & E_0 &\approx 10.26 \text{ kV/cm} \end{aligned} \quad (6.1)$$

enter the dimensional analysis of equations discussed in Chapter 4.

The dimensionless parameters for a system with gap width of  $d = 1$  mm and applied voltages in the range from 500 to 740 V are in our simulations:

$$\begin{aligned} \mu &= 0.0035 & , & & L &= 36 & , & & \gamma &= 0.08, \\ \tau_s &= 0.243 \mathcal{R}_s & , & & 3 \cdot 10^5 &\leq \mathcal{R}_s \leq 3 \cdot 10^6 \\ 17.5 &\leq u_t \leq 26. \end{aligned} \quad (6.2)$$

Here, the dimensionless capacitance of the semiconductor layer is  $\mathcal{C}_s = 0.243$ , and its dimensionless characteristic time scale is  $\tau_s = \mathcal{C}_s \mathcal{R}_s$ . The lower value of the semiconductor resistance corresponds to the dark conductivity when the semiconductor is not illuminated at all, and the upper value of the resistivity range corresponds to the fully photo-activated conductivity. The dimensionless voltage range of  $17.5 \leq u_t \leq 26$  corresponds to the dimensional range of  $500 \text{ V} \leq U_t \leq 740 \text{ V}$ .

### 6.1.2 Numerical solution strategy

Equations (4.31)–(4.40) were solved numerically with an implicit temporal discretization, which makes the calculation numerically stable for arbitrary time and space steps. After discretization, the dynamical equations (4.31) and (4.32) have the form

$$\begin{aligned} \frac{\sigma_i^{m+1} - \sigma_i^m}{\Delta\tau} &= \frac{(\sigma\mathcal{E})_{i+1}^{m+1} - (\sigma\mathcal{E})_i^{m+1}}{\Delta z} + (\mathcal{E}\sigma\alpha(\mathcal{E}))_i^{m+1}, \\ \frac{\mathcal{E}_i^{m+1} - \mathcal{E}_i^m}{\Delta\tau} &= j^m - \mu\mathcal{E}_i^m \frac{\mathcal{E}_i^{m+1} - \mathcal{E}_{i-1}^{m+1}}{\Delta z} - (1 + \mu)(\mathcal{E}\sigma)_i^m, \end{aligned} \quad (6.3)$$

where  $i$  parametrizes the spatial and  $m$  the temporal grid.

For known  $\sigma^m$  and  $\mathcal{E}^m$  at time step  $m$ , the boundary condition on the left (4.33) determines

$$\mathcal{E}_1^{m+1} = \mathcal{E}_1^m + \Delta\tau(j^m - (\mathcal{E}\sigma)_1^m), \quad (6.4)$$

then the other fields  $\mathcal{E}_i^{m+1}$  are calculated successively from the left to right ( $i = 2, 3, \dots, N$ ) by the equation

$$\mathcal{E}_i^{m+1} = \frac{\mathcal{E}_i^m \left( 1 + \frac{\mu\Delta\tau}{\Delta z} \mathcal{E}_{i-1}^{m+1} - (1 + \mu)\Delta\tau\sigma_i^m \right) + \Delta\tau j^m}{1 + \frac{\mu\Delta\tau}{\Delta z} \mathcal{E}_i^m}. \quad (6.5)$$

Here, once again we recall that the ‘left’ corresponds to anode, and ‘right’ to cathode. For  $\sigma_i^{m+1}$ , the boundary condition on the right (4.34) determines

$$\sigma_N^{m+1} = \left( j^m - \frac{\mathcal{E}_N^{m+1} - \mathcal{E}_N^m}{\Delta\tau} \right) / \left( \frac{1 + \gamma}{\gamma} \mathcal{E}_N^{m+1} \right). \quad (6.6)$$

The remaining  $\sigma_i^{m+1}$  can now be calculated successively from the right to left ( $i = N - 1, N - 2, \dots, 1$ ) as

$$\sigma_i^{m+1} = \frac{\sigma_i^m + \frac{\Delta\tau}{\Delta z} (\sigma\mathcal{E})_{i+1}^{m+1}}{1 + \frac{\Delta\tau}{\Delta z} \mathcal{E}_i^{m+1} - \Delta\tau \mathcal{E}_i^{m+1} \alpha(\mathcal{E}_i^{m+1})}. \quad (6.7)$$

The total current  $j^m$  in these equations is determined by

$$j^m = \frac{1}{\mathcal{R}_s + \tau_s L} \left[ \mathcal{U}_t - \mathcal{U}^m + \tau_s \left( \frac{\mu}{2} \left( (\mathcal{E}_N^m)^2 - (\mathcal{E}_1^m)^2 \right) + (1 + \mu) \Delta z \sum_{i=1}^{N-1} (\mathcal{E}\sigma)_i^m \right) \right]. \quad (6.8)$$

This identity can be derived from (4.37) where  $\partial_\tau u$  is identified with  $\int_0^L dz \partial_\tau \mathcal{E}$  through (4.39), and then for  $\partial_\tau \mathcal{E}$ , the identity (4.32) is used.

The results presented in Figures 6.2 to 6.9 are derived on a grid with  $\Delta z = 36/600$  and  $\Delta\tau = 180/600$  which gives a sufficient numerical accuracy.

### 6.1.3 Qualitative features of experimental and numerical oscillations: Hysteresis and limit cycles

The experiments [11] show approximately periodic oscillations. They are quite anharmonic with long phases of low current interrupted by a short current pulse. Depending on applied voltage  $u_t$  and resistance of the semiconductor layer  $\mathcal{R}_s$ , either the homogeneous stationary or the homogeneous oscillating state are dynamically stable. In between, there is a regime of bistability where it depends hysteretically on the previous state whether the system is stationary or oscillating.

The same qualitative behavior can be observed in our numerical solutions. First, the upper panel in Fig. 6.3 shows the current  $j(\tau)$  as a function of time for the system with the parameters from (6.2) and  $\mathcal{R}_s = 4 \cdot 10^5$  and  $u_t = 19.5$  (which corresponds to  $\sigma_s = 2.4 \cdot 10^{-7}/(\Omega\text{cm})$  and  $U_t = 555$  V). After some transient, the current relaxes to periodic anharmonic oscillations. The lower panel in Fig. 6.3 shows the voltage  $u(\tau)$  over the gas discharge; the voltage on the semiconductor is correspondingly  $u_t - u(\tau)$ . In dimensional units, the peak current density of the oscillations is about 9 mA/cm<sup>2</sup> and the frequency is about 120 kHz.

The same numerical data for current  $j$  and voltage  $u$  are shown as a phase space plot in Fig. 6.4. The figure shows more precisely the approach to a

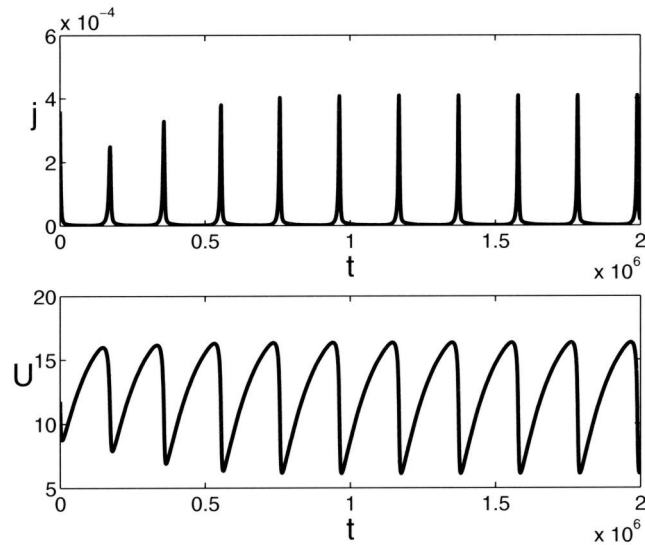


Figure 6.3: The total current  $j(\tau)$  and voltage  $u(\tau)$  over the gas discharge as a function of time  $\tau$ , for the dimensionless parameters from (6.2),  $\mathcal{R}_s = 4 \cdot 10^5$  and  $u_t = 19.5$ .

limit cycle. Fig. 6.4 contains two additional lines, namely the current voltage characteristics of the gas discharge  $u = u(j)$  and the load line  $u = u_t - \mathcal{R}_s j$ . Their intersection marks the stationary solution of the system. In the present case, it is located in the low current regime close to the Townsend limit, while the peak current explores the regime of subnormal glow.

The system of Figs. 6.2 and 6.3 is actually in the bistable regime. For different initial conditions that are a sufficiently small perturbation of the stationary state, the same system relaxes to the stationary point. This is shown as phase space plot in Fig. 6.5.

If the applied voltage  $u_t$  becomes large enough, the stationary state becomes unstable for any initial condition. The search for appropriate parameters was guided by the stability analysis described in section 6.2 and section 6.3. We find that  $u_t = 24$  ( $U_t = 684$  V) with all other parameters unchanged can be used as an example of a system where the stationary solution is dynamically unstable, and the system runs away from this initial state and eventually reaches a limit cycle oscillation. This behavior is shown in Fig. 6.6 as  $j(\tau)$  and  $u(\tau)$ , while Fig. 6.7 shows the corresponding phase space plot.

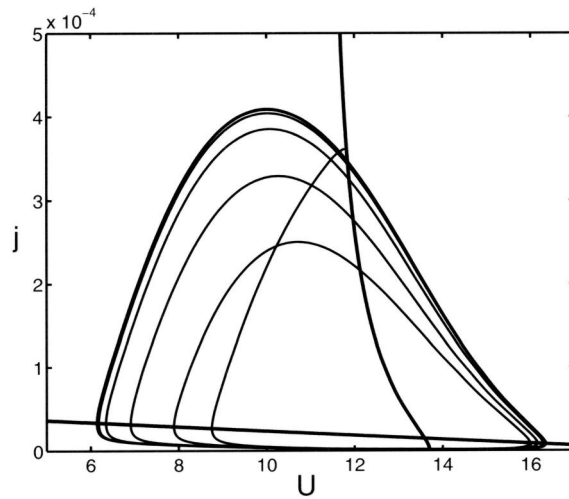


Figure 6.4: Phase space plot of the data from Fig. 6.3. After some transient time, a stable limit cycle is reached. Also drawn are the current-voltage-characteristics  $u = u(j)$  of the gas discharge and the load line  $u = u_t - \mathcal{R}_s j$ . Their intersection denotes the stationary solution.

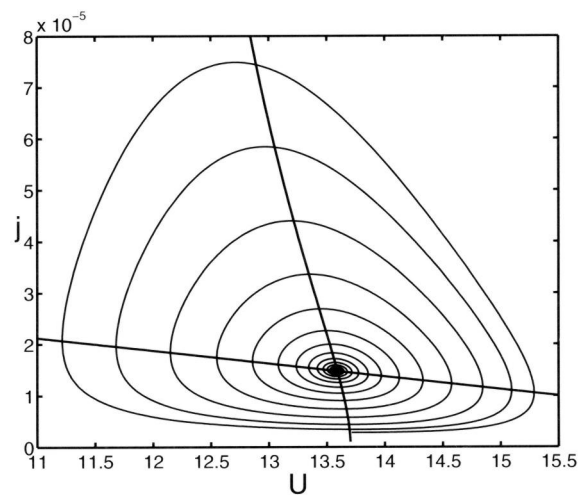


Figure 6.5: System with exactly the same parameters as in Figs. 6.2 and 6.3, but for different initial conditions. The system now spirals inwards towards the stationary point: intersection of the current-voltage-characteristics of the gas discharge and the load line.



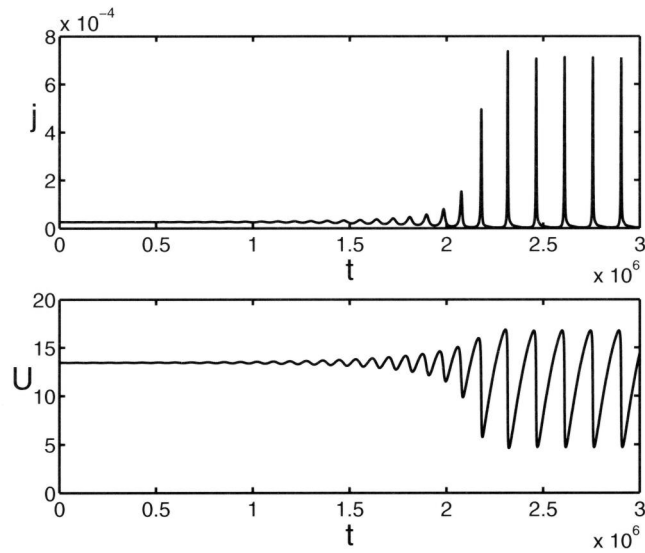


Figure 6.6:  $j(\tau)$  and  $u(\tau)$  for the parameters from (6.2),  $\mathcal{R}_s = 4 \cdot 10^5$  and  $u_t = 24$ . The stationary state now is linearly unstable and develops into a limit cycle.

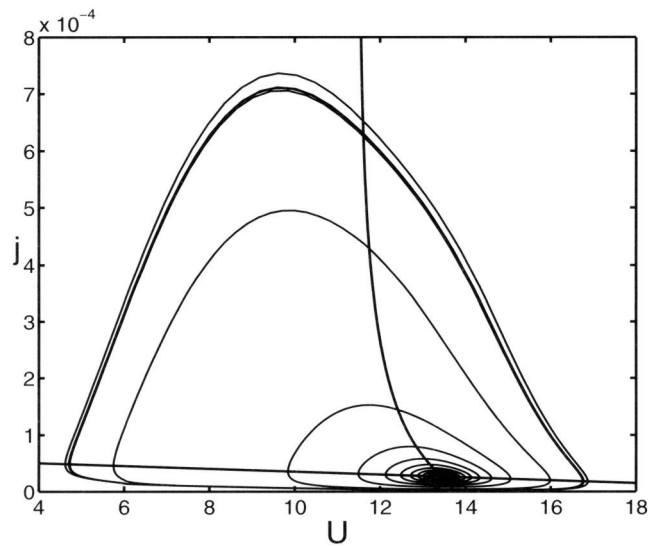


Figure 6.7: Phase space plot of the data from Fig. 6.6 with current-voltage-characteristics and load line.

### 6.1.4 Quantitative comparison: Amplitude and frequency of oscillations

The qualitative agreement of numerical solutions and experiment now encourages a more quantitative comparison. The thesis [12] contains diagrams on how frequency and maximal current amplitude depend on the semiconductor conductivity for a gas gap of 1 mm. These diagrams are presented in Chapter 3 of the present study, in Fig. 3.7.

The same diagrams can also be derived from the numerically obtained limit cycle oscillations, they are presented in Fig. 6.8. The figure shows the current amplitude  $A$  and frequency  $f$  as a function of semiconductor conductance  $1/\mathcal{R}_s$  for fixed voltage  $u_t$  or as a function of  $u_t$  for fixed  $1/\mathcal{R}_s$ . The notation of Fig. 6.8 corresponds to the notation of the experimental Fig. 3.7 as follows way:  $f \equiv f_0$ ,  $u_t \equiv U_0$ ,  $A \equiv \hat{I}$ ,  $1/\mathcal{R}_s \equiv \sigma_{GaAs}$ .

We now compare the results for the gas discharge width of 1mm, from the simulation (Fig.6.8) and the experiment (Fig. 3.7). The upper left panel of Fig. 6.8 shows that the maximal current amplitude  $A$  as a function of applied voltage  $u_t$  is increasing with decreasing slope. This agrees with the experimental observations Fig. 3.7(b) lower panel. No attempt of quantitative comparison is made, since the experimental result is for  $d = 0.5\text{mm}$  and the numerical is for  $d = 1\text{mm}$ . Nevertheless, qualitative comparison is possible since [12] says that the frequency and amplitude for fixed conductivity depend for both system sizes, in about the same way on the applied voltage. The upper right panel (Fig. 6.8) shows that the frequency  $f$  is an almost linearly increasing function of applied voltage  $u_t$ ; this is actually in contradiction with the statement in [12] that the frequency would decrease (as seen in Fig. 3.7(b) upper panel).

The lower two panels allow some quantitative comparison since corresponding experimental diagrams exist and are presented in Fig. 3.7. The experiments explore the range of  $0.6 \cdot 10^{-7}/(\Omega\text{cm}) \leq \sigma_s \leq 2.8 \cdot 10^{-7}/(\Omega\text{cm})$  which corresponds to  $0.62 \cdot 10^{-6} \leq 1/\mathcal{R}_s \leq 2.9 \cdot 10^{-6}$ . The experimental diagrams for  $U_t = 605\text{ V}$  - Fig. 3.7(c) and  $616\text{ V}$  - Fig. 3.7(d) show that the amplitude  $A$  is very sensitive to this change while the frequency  $f$  is rather robust. The numerical results are derived for  $u_t = 21$  which corresponds to  $U_t = 600\text{ V}$ .

In detail, the experimental curve for the current amplitude for  $605\text{ V}$  shows an initial increase from  $0.2$  to  $0.8\text{ mA}$  with a subsequent sudden drop to essentially  $0$  from which the current suddenly jumps to values from  $1.0$  to  $1.5\text{ mA}$ . For  $616\text{ V}$ , in contrast, an almost continuous increase from  $0.2$  to  $2.7\text{ mA}$  is observed for the same resistance range. Not too surprisingly, our numerical results reproduce neither of these results. Rather, we observe an almost constant value in the range of  $5.5 \cdot 10^{-4}$  to  $6.0 \cdot 10^{-4}$  in the lower left panel.

On the other hand, for the variation of the frequency  $f$  with conductivity, experiments [12] both for  $605\text{ V}$  and for  $616\text{ V}$  observe nearly linear increase from  $115\text{ kHz}$  or  $125\text{ kHz}$  to  $220\text{ kHz}$  ( $4.6 \cdot 10^{-6} \leq f \leq 8.8 \cdot 10^{-6}$  in our dimensionless units) in the range of  $0.62 \cdot 10^{-6} \leq 1/\mathcal{R}_s \leq 2.9 \cdot 10^{-6}$ . Our numerical results in this range of  $1/\mathcal{R}_s$  show the same linear increase, from  $1.5 \cdot 10^{-6}$  to  $6.5 \cdot 10^{-6}$ . We believe that this agreement is quite convincing, in particular, since no parameter

fitting was tried.

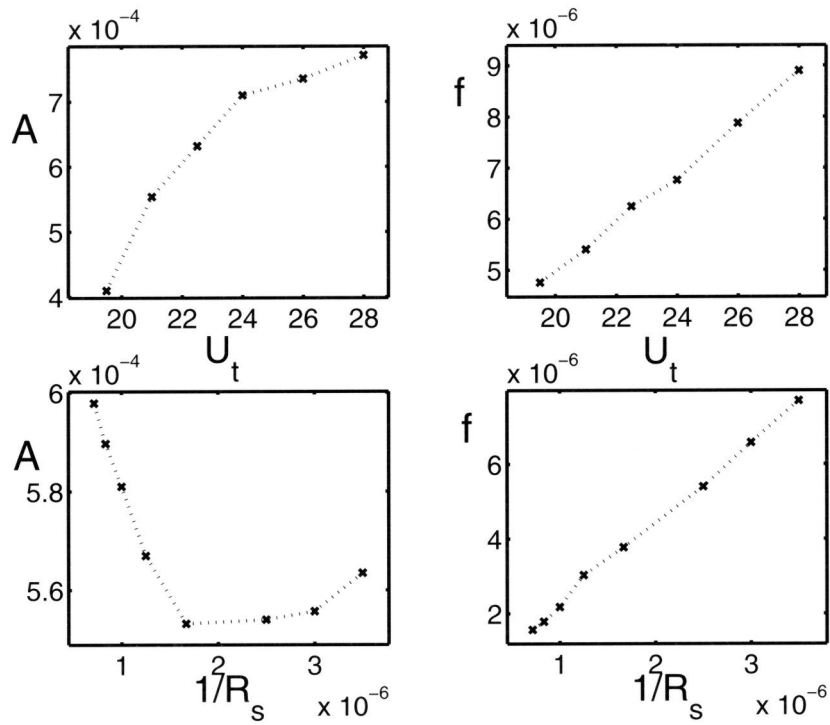


Figure 6.8: Amplitude  $A$  and frequency  $f$  of the current oscillations as a function of applied total voltage  $u_t$  (for fixed resistance  $R_s = 4 \cdot 10^5$ ) and as a function of conductivity  $1/\mathcal{R}_s$  (for fixed voltage  $u_t = 21$ ).

Summarizing, we find convincing agreement with experiment for  $A$  as a function of  $u_t$  as well as for  $f$  as a function of  $1/\mathcal{R}_s$ . For the last, the available experimental results allow to identify an almost quantitative agreement. The sensitivity of the experimental results on  $A$  as a function of  $1/\mathcal{R}_s$  does not allow quantitative comparison, and our results for  $f$  as a function of  $u_t$  deviate in their functional form from the available statements about experimental results.

### 6.1.5 Mechanism of the oscillations, reaction-diffusion models and surface charge

The voltage profiles  $u(\tau)$  in Figs. 6.2 and 6.5 show that there are two processes involved in the oscillations.

The first process occurs on the slow time scale  $\tau_s$  of the semiconductor. It describes the exponential decay of the voltage  $u_t - u(\tau) - \mathcal{R}_s j \propto e^{-\tau/\tau_s}$  over the semiconductor layer according to Eq. (4.37), as long as the contribution of  $\mathcal{R}_s j$  does not vary substantially. The decay time  $\tau_s$  is the Maxwell time due to resistance and capacitance of the semiconductor layer.  $\tau_s$  accounts for the slow rise of the voltage  $u(\tau)$  over the gas discharge layer to a value above the current voltage characteristics of the gas discharge.

The other process is the electric breakdown of the gas discharge layer for sufficiently large  $u(\tau)$  which leads to a current pulse and a rapid subsequent decay of  $u(\tau)$ .

It has been suggested by a number of authors that the current could be approximated by a similarly simple equation of the type  $\partial_\tau j = g(u, j)$ , where  $g$  vanishes on the current-voltage-characteristics. This would bring the equations into a reaction diffusion form.

However, as it will be seen in the next chapter (and in [91]), such an approximation of the underlying equations (4.31)–(4.34), (4.39) and (4.40) is not possible, since it would not admit the period doubling events observed in [91], and it would not allow the phase space plots in Figs. 6.3, 6.4 and 6.6 to intersect the characteristics with a non-vanishing derivative, as they definitely do.

The physical reason for this behavior is the finite response time of the semiconductor, its “inertia” which doesn’t allow an instantaneous reaction of the current. If ions are created by bulk impact ionization close to the anode, they will cross the whole gap until they reach the cathode and possibly liberate more electrons by secondary emission. The time that the ions need to cross the gap, is therefore an important scale of internal memory of the gas discharge. It can be approximated as  $\tau_{ion} \approx L/(\mu\mathcal{E}) \approx L^2/(\mu u(\tau))$  where  $|\mathcal{E}|$  is some average field within the gas gap. For the gap of  $L = 36$  ( $d = 1$  mm), the ion crossing time is estimated as  $2.6 \cdot 10^4$  for  $u(\tau) = 14$  or as  $1.5 \cdot 10^4$  for  $u(\tau) = 24$  (which corresponds to 0.6 or 1  $\mu$ s in dimensional units). This time is of the same order or larger than the duration of a current pulse, both in our numerical solutions and in the experimental results of [11] presented in Fig. 3.6. (For the experiments on the 0.5 mm gap of Fig. 3.5, the situation seems to be different.)

Finally, it has been suggested in [92] that the surface charge on the interface between gas and semiconductor could play an important role, in a similar way as in AC discharges. This is certainly true, but the surface charge  $q(\tau)$  is not an independent variable. Rather it is fully determined by the solution discussed above through

$$q(\tau) = \epsilon_s \frac{u_t - u(\tau)}{L} - \mathcal{E}(L, \tau). \quad (6.9)$$

The assumption that this surface charge is the only relevant charge in the whole system doesn’t lead to a satisfactory description either, but the space charges

in the gas discharge layer have to be taken into account, too.

## 6.2 Stability analysis: Method

The direct numerical solution of the dynamical problem is a time consuming procedure, that does not allow the exploration of a wide set of parameter values. We therefore have developed a linear stability analysis of the stationary state. It determines whether the stationary state is dynamically unstable and how small perturbations of such a state grow. In the present section, we present the method, and in the following one the results.

### 6.2.1 Problem setting and stationary solutions

We recall the dynamical equations from the Chapter 4 in the following form

$$\partial_\tau \sigma = \partial_z j_e + j_e \alpha(\mathcal{E}) \quad , \quad j_e = \sigma \mathcal{E}, \quad (6.10)$$

$$\partial_\tau \mathcal{E} = j(\tau) - (1 + \mu)j_e - \mu \mathcal{E} \partial_z \mathcal{E}, \quad (6.11)$$

$$\tau_s \partial_\tau u(\tau) = u_t - u(\tau) - \mathcal{R}_s j(\tau), \quad (6.12)$$

$$0 = \partial_z \phi(z, \tau) + \mathcal{E}(z, \tau) \quad (6.13)$$

with the boundary conditions

$$\partial_\tau \mathcal{E}(0, \tau) = j(\tau) - j_e(0, \tau), \quad (6.14)$$

$$\partial_\tau \mathcal{E}(L, \tau) = j(\tau) - \frac{1 + \gamma}{\gamma} j_e(L, \tau), \quad (6.15)$$

$$\phi(L, \tau) = -u(\tau) \quad , \quad \phi(0, \tau) = 0. \quad (6.16)$$

The stationary solutions form the starting point of the perturbation analysis. They solve the equations

$$\partial_z j_{e0} = -j_{e0} \alpha(\mathcal{E}_0), \quad (6.17)$$

$$\mu \mathcal{E}_0 \partial_z \mathcal{E}_0 = j_0 - (1 + \mu)j_{e0}, \quad (6.18)$$

$$\partial_z \phi_0 = -\mathcal{E}_0, \quad (6.19)$$

$$u_0 = u_t - \mathcal{R}_s j_0 \quad (6.20)$$

with boundary conditions

$$j_{e0}(0) = j_0 \quad , \quad \frac{1 + \gamma}{\gamma} j_{e0}(L) = j_0, \quad (6.21)$$

$$\phi_0(0) = 0 \quad , \quad \phi_0(L) = -u_0. \quad (6.22)$$

Eqs. (6.17)–(6.19) with (6.21) and (6.22) define the current voltage characteristics  $u = u(j)$  of a stationary discharge in the regime between Townsend and glow discharge [29, 85, 89]. Eq. (6.20) is the load line due to the external circuit. The intersection of load line and characteristics defines a generically discrete number of stationary solutions of the system as a whole.

### 6.2.2 Linear perturbations

For linear perturbations about this stationary state, we use the ansatz

$$j_e(z, \tau) = j_{e0}(z) + j_{e1}(z) e^{\lambda\tau}, \quad (6.23)$$

$$\mathcal{E}(z, \tau) = \mathcal{E}_0(z) + \mathcal{E}_1(z) e^{\lambda\tau}, \quad (6.24)$$

$$\phi(z, \tau) = \phi_0(z) + \phi_1(z) e^{\lambda\tau}, \quad (6.25)$$

$$j(\tau) = j_0 + j_1 e^{\lambda\tau}. \quad (6.26)$$

The lower index 0 denotes the unperturbed stationary solutions while the lower index 1 denotes the linear perturbations about this stationary solution. The factorization of the perturbation into a  $z$  dependent function times the exponential  $e^{\lambda\tau}$  anticipates the eigenvalue problem of the solution.

In terms of the original variables, the explicit expansion in first order perturbation theory is a lengthy expression, but in terms of the variables

$$h = \frac{\sigma_1 \mathcal{E}_0 + \sigma_0 \mathcal{E}_1}{\sigma_0 \mathcal{E}_0} = \frac{j_{e1}(z) e^{\lambda\tau}}{j_{e0}(z)} \quad \text{and} \quad g = \mathcal{E}_0 \mathcal{E}_1 \quad (6.27)$$

the equations have a more compact form

$$\partial_z h = \frac{\lambda}{\mathcal{E}_0} h - \left( \frac{\alpha'(\mathcal{E}_0)}{\mathcal{E}_0} + \frac{\lambda}{\mathcal{E}_0^3} \right) g, \quad (6.28)$$

$$\partial_z g = -(1 + \mu) \frac{j_{e0}}{\mu} h - \frac{\lambda}{\mu \mathcal{E}_0} g + \frac{j_1}{\mu}, \quad (6.29)$$

$$\partial_z j_1 = 0, \quad (6.30)$$

$$\partial_z \phi_1 = -\frac{1}{\mathcal{E}_0} g \quad (6.31)$$

with boundary conditions

$$\phi_1(0) = 0, \quad (6.32)$$

$$j_1 = \frac{\lambda}{\mathcal{E}_0(0)} g(0) + j_0 h(0), \quad (6.33)$$

$$j_1 = \frac{\lambda}{\mathcal{E}_0(L)} g(L) + j_0 h(L), \quad (6.34)$$

$$\mathcal{R}_s j_1 = (1 + \lambda \tau_s) \phi_1(L). \quad (6.35)$$

Here the equation  $\partial_z j_1 = 0$  for the conservation of the total current is written explicitly in order to bring the equations into the homogeneous form

$$\partial_z \begin{pmatrix} h \\ g \\ j_1 \\ \phi_1 \end{pmatrix} = \begin{pmatrix} \frac{\lambda}{\mathcal{E}_0} & -\left( \frac{\alpha'}{\mathcal{E}_0} + \frac{\lambda}{\mathcal{E}_0^3} \right) & 0 & 0 \\ -\frac{1+\mu}{\mu} j_{e0} & -\frac{\lambda}{\mu \mathcal{E}_0} & \frac{1}{\mu} & 0 \\ 0 & 0 & 0 & 0 \\ 0 & -\frac{1}{\mathcal{E}_0} & 0 & 0 \end{pmatrix} \cdot \begin{pmatrix} h \\ g \\ j_1 \\ \phi_1 \end{pmatrix} \quad (6.36)$$

The boundary conditions (6.32) and (6.33) at  $z = 0$  can be written as orthogonality relations

$$\begin{pmatrix} j_0 \\ \frac{\lambda}{\varepsilon_0(0)} \\ -1 \\ 0 \end{pmatrix} \cdot \begin{pmatrix} h \\ g \\ j_1 \\ \phi_1 \end{pmatrix}_0 = 0, \quad \begin{pmatrix} 0 \\ 0 \\ 0 \\ 1 \end{pmatrix} \cdot \begin{pmatrix} h \\ g \\ j_1 \\ \phi_1 \end{pmatrix}_0 = 0. \quad (6.37)$$

The general solution  $\vec{v}(z)$  of (6.36) is therefore a superposition of two independent solutions  $\vec{v}_1(z)$  and  $\vec{v}_2(z)$  of (6.36) that both obey (6.37) in  $z = 0$ :

$$\vec{v}(z) = \begin{pmatrix} h(z) \\ g(z) \\ j_1(z) \\ \phi_1(z) \end{pmatrix} = C_1 \vec{v}_1(z) + C_2 \vec{v}_2(z). \quad (6.38)$$

As initial conditions, one can choose, e.g.,

$$\vec{v}_1(0) = \begin{pmatrix} 1/j_0 \\ 0 \\ 1 \\ 0 \end{pmatrix}, \quad \vec{v}_2(0) = \begin{pmatrix} 0 \\ \frac{\varepsilon_0(0)}{\lambda} \\ 1 \\ 0 \end{pmatrix}. \quad (6.39)$$

The components of the two solutions are denoted as  $\vec{v}_i(z) = (h_i(z), g_i(z), j_{1,i}(z), \phi_{1,i}(z))$ .

The boundary conditions (6.34) and (6.35) at  $z = L$  also have the form of orthogonality relations

$$\begin{pmatrix} j_0 \\ \frac{\lambda}{\varepsilon_0(L)} \\ -1 \\ 0 \end{pmatrix} \cdot \begin{pmatrix} h \\ g \\ j_1 \\ \phi_1 \end{pmatrix}_L = 0, \quad \begin{pmatrix} 0 \\ 0 \\ -\mathcal{R}_s \\ 1 + \lambda\tau_s \end{pmatrix} \cdot \begin{pmatrix} h \\ g \\ j_1 \\ \phi_1 \end{pmatrix}_L = 0. \quad (6.40)$$

Now each one of these two conditions determines the ratio  $C_1/C_2$  of the general solution (6.38):

$$C_1 \left[ j_0 h_1(L) + \frac{\lambda}{\varepsilon_0(L)} g_1(L) - j_{1,1}(L) \right] + C_2 \left[ j_0 h_2(L) + \frac{\lambda}{\varepsilon_0(L)} g_2(L) - j_{1,2}(L) \right] = 0, \quad (6.41)$$

$$C_1 \left[ -\mathcal{R}_s j_{1,1}(L) + (1 + \lambda\tau_s) \phi_{1,1}(L) \right] + C_2 \left[ -\mathcal{R}_s j_{1,2}(L) + (1 + \lambda\tau_s) \phi_{1,2}(L) \right] = 0, \quad (6.42)$$

where  $j_{1,1}(L) = 1 = j_{1,2}(L)$ , since these components have this value at  $z = 0$  according to (6.39):  $j_{1,1}(0) = 1 = j_{1,2}(0)$ , and since the equation of motion for  $j_1$  is  $\partial_z j_1 = 0$ . A nontrivial solution of both (6.41) and (6.42) requires the determinant

$$\Delta = \begin{vmatrix} j_0 h_1(L) + \frac{\lambda}{\varepsilon_0(L)} g_1(L) - 1 & j_0 h_2(L) + \frac{\lambda}{\varepsilon_0(L)} g_2(L) - 1 \\ -\mathcal{R}_s + (1 + \lambda\tau_s) \phi_{1,1}(L) & -\mathcal{R}_s + (1 + \lambda\tau_s) \phi_{1,2}(L) \end{vmatrix} \quad (6.43)$$

to vanish. This condition leads to a quadratic equation for the eigenvalue  $\lambda$ .

### 6.2.3 Rescaling with $\mu$ and numerical calculation

The eigenvalue  $\lambda$  can now be calculated numerically.

First, it should be noted, that the equation of motion (6.36) has matrix elements of very different size, since  $\mu$  is a very small parameter. However, this apparent stiffness of the problem can be removed by introducing the new parameters

$$\begin{aligned} \iota_e &= \frac{j_e}{\mu} \quad , \quad \iota = \frac{j}{\mu} \quad , \quad r_s = \mathcal{R}_s \mu, \\ \bar{\tau}_s &= \tau_s \mu \quad , \quad s = \frac{\lambda}{\mu}. \end{aligned} \quad (6.44)$$

The introduction of rescaled current density and time scale and resistivity has a direct physical motivation. Previous analysis of the stationary solutions [29, 85, 89] as well as the dynamical solutions of section 6.1 show that velocities should actually be measured on the time scale of the ions and not of the electrons. So the time scale should be measured in units of  $t_+ = 1/(\alpha_0 \mu_+ E_0) = t_0/\mu$  rather than in units of  $t_0 = 1/(\alpha_0 \mu_e E_0)$ . The rescaling (6.44) directly follows from this consideration.

Now the eigenvalue  $s$  can be calculated numerically as follows: First an initial estimate  $s_0$  is chosen. Then the two initial conditions (6.39) at  $z = 0$  are integrated numerically with (6.36) up to  $z = L$ . Generically, the determinant  $\Delta$  (6.43) will then be non-vanishing. The request that the determinant does vanish, fixes a new value for  $s$  that is used for the next step of the iteration within an under-relaxation method that guarantees the stability of the convergence. This procedure is repeated until an accuracy of

$$\left| \frac{s_{k+1} - s_k}{s_{k+1}} \right| < 10^{-6} \quad (6.45)$$

is reached.

The eigenvalue  $s$  is in general a complex parameter whose real part describes the growth or decay of the oscillation amplitude while its imaginary part describes the oscillation frequency. Since  $s$  is a parameter in the equation of motion (6.36), also the vector  $\vec{v}(z)$  has complex entries. Therefore 16 real functions  $\text{Re } h_1(z)$ ,  $\text{Im } h_1(z)$  etc. have to be integrated over  $z$ . It is convenient to also integrate the two real functions  $j_{e0}$  and  $\mathcal{E}_0$  that enter the matrix (6.36) together with the perturbations. The iteration program is written in fortran 90 with complex variables. For the integration of equations, a 4th order Runge-Kutta method is used. The number of grid points used was 500, since 1000 or 2000 grid points give essentially the same result.

## 6.3 Stability Analysis: Results

In the present section, the validity of the stability analysis results are confirmed by comparison with numerical solutions of the full dynamical problem. The



stability analysis is then used to determine the phase diagram for the onset of oscillating solutions.

### 6.3.1 The structure of the results

The stability analysis determines not only the complex eigenvalue  $\lambda$ , but also the whole linear correction

$$\vec{v}(z) = C_1 \left[ \vec{v}_1(z) - \frac{\mathcal{R}_s + (1 + \lambda\tau_s) u_{1,2}(L)}{\mathcal{R}_s + (1 + \lambda\tau_s) u_{1,1}(L)} \vec{v}_2(z) \right], \quad (6.46)$$

up to the arbitrary complex constant  $C_1$ .

This  $\vec{v}(z)$  determines the evolution of current and voltage in linear approximation about the stationary solution  $(j_0, u_0)$ :

$$j(\tau) = j_0 + j_1 e^{\lambda\tau} + c.c., \quad (6.47)$$

$$u(\tau) = u_0 + u_1 e^{\lambda\tau} + c.c., \quad (6.48)$$

where c.c. denotes the complex conjugate. The ratio between  $u_1$  and  $j_1$  is fixed through the boundary condition (6.35) to the value

$$u_1 = -\frac{j_1}{(1 + \lambda\tau_s)/\mathcal{R}_s} = r e^{i\alpha} j_1, \quad (6.49)$$

$$\text{where } r = \frac{\mathcal{R}_s}{|1 + \lambda\tau_s|} \text{ and} \quad (6.50)$$

$$\cos \alpha = -\frac{1 + \text{Re } \lambda\tau_s}{|1 + \lambda\tau_s|}, \quad \sin \alpha = \frac{\text{Im } \lambda\tau_s}{|1 + \lambda\tau_s|}.$$

The final result is

$$j(\tau) = j_0 + c \mu e^{\text{Re } \lambda\tau} \cos(\text{Im } \lambda\tau + \alpha_0), \quad (6.51)$$

$$u(\tau) = u_0 - c r e^{\text{Re } \lambda\tau} \cos(\text{Im } \lambda\tau + \alpha + \alpha_0) \quad (6.52)$$

where the amplitude  $c$  and absolute phase  $\alpha_0$  reflect the arbitrary factor  $C_1$  in (6.46) and are adjustable while all other parameters are fixed.

### 6.3.2 Comparison with solutions of the full PDE's

As a check of accuracy, these solutions are now first compared with numerical solutions of the full PDE problem.

For the set of parameters from Figs. 6.2, 6.3 and 6.4, the stationary solution is  $(j_0, u_0) = (1.49 \cdot 10^{-5}, 13.583)$ , and the eigenvalue  $\lambda$  has the complex value  $\lambda = -2.913 \cdot 10^{-6} \pm i 4.822 \cdot 10^{-5}$ . As  $\tau_s = 340/\mu$  and  $\mathcal{R}_s = 1400/\mu$ , the ratio of current and voltage amplitude  $r = 295/\mu$  and the phase shift  $\alpha = 98.69^\circ$  are determined through Eq. (6.50).

The comparison of these predictions from the stability analysis with numerical solutions of the full PDE problem are shown in Fig. 6.9. Here the free

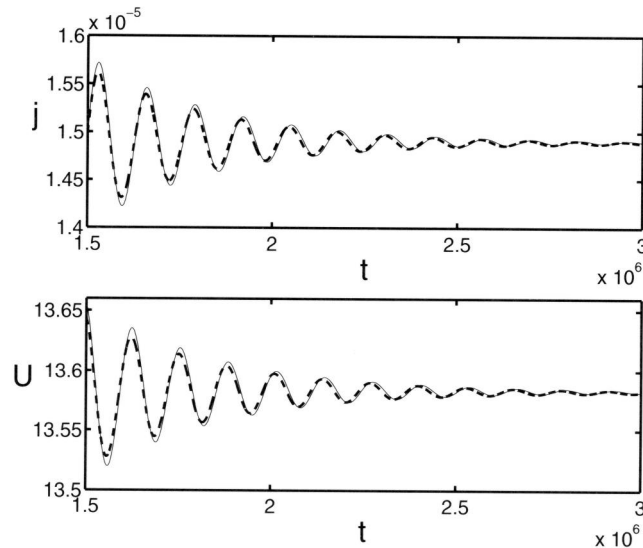


Figure 6.9: Comparison of  $j(\tau)$  and  $u(\tau)$ ) from the stability analysis (solid lines) with the result from the simulation (dashed lines) for the parameter values of Figs. 6.3-6.5.

parameters for the total amplitude  $c$  and the absolute phase  $\alpha_0$  were chosen such as to fit the PDE-data well.

This visual agreement can be tested in more detail. In particular, we used the PDE-data in the time interval  $5 \cdot 10^5 < \tau < 6.5 \cdot 10^5$  to determine the phase shift  $\alpha$  between  $u_1$  and  $j_1$ . It is  $\alpha = (100 \pm 0.4)^\circ$ , convincingly close to the predicted value of  $\alpha = 98.69^\circ$ .

Increasing the total applied voltage  $u_t$ , the real part of the eigenvalue  $\lambda$  grows until it becomes positive. This means that the stationary solution becomes linearly unstable and perturbations will grow. An example of such behavior occurs for  $u_t = 24$  with all other parameters as before. The stationary solution is then  $(j_0, u_0) = (2.64 \cdot 10^{-5}, 13.441)$ , the eigenvalue is  $\lambda = 2.493 \cdot 10^{-6} \pm i 7.375 \cdot 10^{-5}$ , the ratio of current and voltage amplitude is  $r = 192/\mu$  and the phase shift is  $\alpha = 99.83^\circ$ .

Fig. 6.10 shows again the comparison between these results and the numerical solutions of the full PDE's. Again, the agreement is very convincing.

Of course, the predictive power of linear stability analysis is limited to small perturbations with  $j_1 \ll j_0$  and  $u_1 \ll u_0$ . When the amplitude of the oscillation from Fig. 6.7 increases further, nonlinear couplings set in and the system finally reaches a limit cycle as shown in Fig. 6.8.

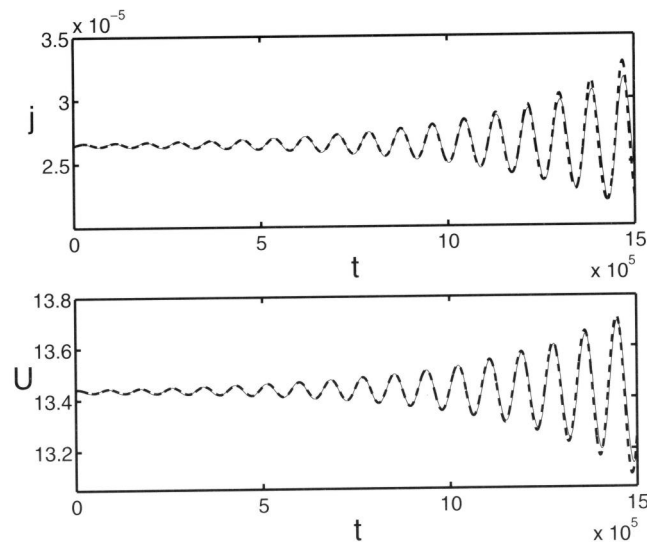


Figure 6.10: Comparison of  $j(\tau)$  and  $u(\tau)$  from the stability analysis (solid lines) with the result from the simulation (dashed lines) for the parameter values of Figs. 6.5-6.6 where the stationary solution is unstable.

### 6.3.3 Calculation of phase diagrams

The stability analysis now allows one to derive the bifurcation line where a homogeneous stationary state loses its stability. Fig. 6.11 shows this bifurcation line for the parameters (6.2) as a function of applied voltage  $u_t$  and conductivity  $1/\mathcal{R}_s$  for three different values of  $\gamma$ . Besides the value  $\gamma = 0.08$  used everywhere else in the paper, also results for  $\gamma = 0.04$  and  $0.16$  are shown to illustrate the sensitivity of theoretical predictions from this parameter. For  $\text{Re } \lambda < 0$ , the stationary state is linearly stable, while for  $\text{Re } \lambda > 0$ , the system is always in the oscillating state.

Comparison with the experimental phase diagram for the gas gap with a corresponding width of  $d = 1$  mm [12] (given by Fig. 3.3(b) in Chapter 3) shows qualitative and quantitative correspondences, but also deviations. Experiments in the 1 mm gap for  $U_t < 585$  V ( $u_t = 20.5$ ) do not exhibit oscillations. In detail, the raising phase transition line on the left hand side of the diagram is straighter than in the 0.5 mm case from [11] (given by Fig. 3.3(a)), it raises with positive slope from  $(U_t, \sigma_s) = (585 \text{ V}, 0.7 \cdot 10^{-7}/(\Omega \text{ cm}))$  to  $(610 \text{ V}, 2.0 \cdot 10^{-7}/(\Omega \text{ cm}))$ , where the slope has changed gradually to being parallel to the  $\sigma_s$  axis. The bifurcation line then continues with negative slope up to  $(600 \text{ V}, 2.8 \cdot 10^{-7}/(\Omega \text{ cm}))$ . In dimensionless units, these points on the raising bifurcation line are  $(u_t, 1/\mathcal{R}_s) = (20.5, 0.7 \cdot 10^{-6})$ ,  $(21.4, 2.1 \cdot 10^{-6})$  and  $(21, 2.9 \cdot 10^{-6})$ . The upper part of this experimental transition line is rather well described by

the theoretical curve for the somewhat large value  $\gamma = 0.16$ . In the lower part, the shape of experimental and theoretical curve deviate.

Furthermore, the experiment shows another bifurcation line almost parallel to the  $U_t$  axis at values of  $\sigma_s$  between  $0.7 \cdot 10^{-7}/(\Omega \text{ cm})$  and  $0.5 \cdot 10^{-7}/(\Omega \text{ cm})$  that intersects with the raising line. In dimensionless units this corresponds to a plateau at values of  $1/\mathcal{R}_s$  between  $0.7 \cdot 10^{-6}$  and  $0.5 \cdot 10^{-6}$ . An approach to such a plateau can also be seen in the calculated phase diagram. However, the theoretical curve crosses over continuously to this plateau, while the experimental curve seems to show the intersection of two bifurcation lines with quite distinct slope. We have no explanation for this deviation.

It is remarkable that the bifurcation theory also covers the almost horizontal bifurcation line for small  $1/\mathcal{R}_s$ . Another explanation for this experimentally observed feature of the phase diagram would have been a breakdown of the continuum approximation: the recovery phase of the oscillation would have carried such a low current that the discreteness of the electrons would have to be taken into account.

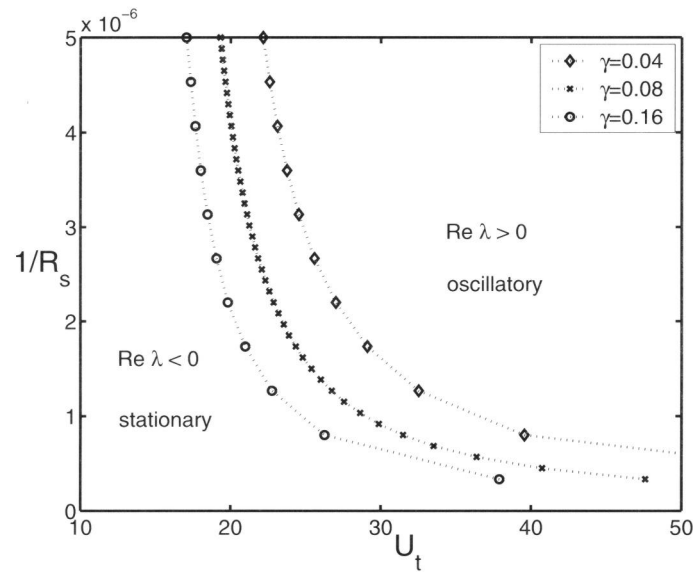


Figure 6.11: Bifurcation diagram for the parameters from (6.2) (where  $L = 36$ ) and 3 different values of  $\gamma$ . The lines separate regions with  $\text{Re } \lambda < 0$  where the stationary state is linearly stable from regions with  $\text{Re } \lambda > 0$  where the homogeneous stationary state loses its stability.

Finally, it was observed experimentally [11, 12] that increasing the system size  $L$  while keeping other conditions unchanged, the frequency decreases and oscillations set in at higher voltages. This agrees with our calculated phase diagram in Fig. 6.12. Indeed, for  $u_t < 22.5$ , the homogeneous stationary state

is stable for  $L = 72$ .

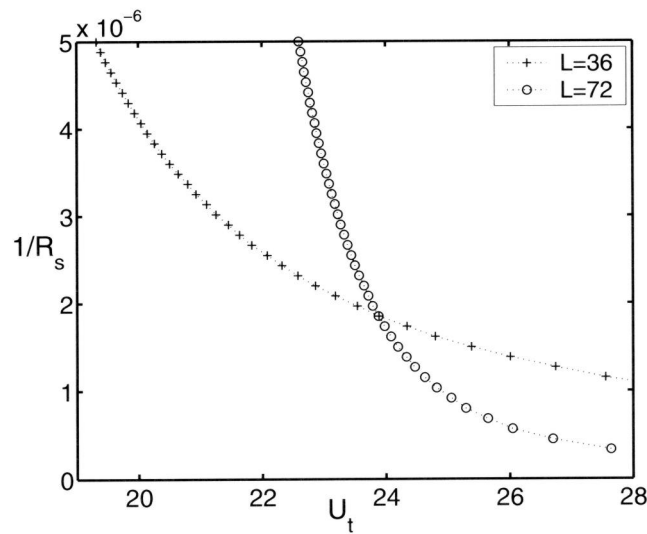


Figure 6.12: Bifurcation diagram for  $\gamma = 0.08$ ,  $L = 36$  and  $L = 72$ .

## 6.4 Conclusion

The simplest model for a one-dimensional short gas discharge coupled to an external circuit with resistor, capacitance and stationary voltage has been analyzed. This analysis is directly applicable to experiments performed in [11, 12].

We have presented fully numerical solutions as well as a linear stability analysis of the stationary state of the system which are in very good mutual agreement. The numerical solutions reproduce experimental observations of bistability and oscillations in a semi-quantitative manner, though the model is minimal and no attempt of parameter fitting has been made. The stability analysis allows us to derive bifurcation diagrams in a simple manner, they also agree overall with experimentally obtained bifurcation diagrams.

It should be remarked that we have constrained the analysis to the gap of 1 mm wide; the gap of 0.5 mm is so sensitive to the actual value of secondary emission  $\gamma$  that quantitative analysis based on a fixed value of  $\gamma$  seemed doubtful.

We have reproduced a number of experimental observations up to the dependence of oscillation amplitude on applied potential and of the oscillation frequency on the conductivity of the semiconductor layer, while discrepancies of other observables will stay a subject of investigation. This opens up the way to investigate now the spatial and spatio-temporal patterns in the next step.

## Chapter 7

# Period doubling cascade and relation to reaction diffusion models

Short planar glow discharges coupled to a resistive layer exhibit a wealth of spontaneous spatio-temporal patterns. Similarities with other pattern forming systems suggest to apply reaction-diffusion models, and several authors motivated them from discharge physics. We investigate the temporal oscillations of the discharge system and find a cascade of period doubling events. This shows that the inner structure of the discharge is more complex than can be described by a reaction-diffusion-model with negative differential conductivity. We even find an example where an oscillation coincides with fully positive differential conductivity, and we derive an alternative reduced model.

### 7.1 Introduction

The theory for the previously described experiments has largely focussed on effective reaction-diffusion models in the two transversal directions, and on the negative differential conductivity of the glow discharge as the driving force of pattern formation. The similarity with patterns in other systems actually suggests the use of such effective models. A number of authors [5, 9, 15, 18, 19, 22, 26–28] actually have aimed at deriving such models from gas discharge physics. On the other hand, the observation of unconventional patterns like zigzag-destabilized spirals raises doubts whether reaction-diffusion models are sufficient to understand the observed patterns.

In the present chapter, we examine the concepts of reaction-diffusion models and negative differential conductivity on the particular case of a short DC driven glow discharge in a parameter range that exhibits spontaneous temporal oscillations but no spatial structures transverse to the current [11]. In short, we

find

- (i) that a discharge on the transition from Townsend to glow discharge can combine a positive local differential conductivity with a negative global differential conductivity;
- (ii) that a glow discharge in a simple electric circuit shows more complex behavior than can be expected from the proposed reaction-diffusion models [5, 9, 15, 18, 19, 22, 26–28] for voltage  $U$  and current  $J$  with (global) negative differential conductivity  $dU/dJ < 0$ ;
- (iii) in particular, that the system can show a cascade of period doubling bifurcations. Period doubling actually has been observed experimentally in glow discharges, but in more complex geometries and in longer systems [61, 62].
- (iv) We derive a new effective dynamical model in terms of a parameter and a function by adiabatic elimination of the electrons. There is no systematic way to reduce this model to a simpler one [5, 9, 15, 18, 19, 22, 26–28] with two scalar parameters like voltage  $U$  and current  $J$ . We draw this conclusion both from direct analysis and from the occurrence of period doubling in the numerical solutions.
- (v) Finally, we present an example where local and global positive differential conductivity nevertheless allow for current oscillations.

## 7.2 Predictions of a reaction-diffusion model

In the experiments of [8–11, 57, 67–73], a planar glow discharge layer with short length in the forward direction and wide lateral dimensions is coupled to a semiconductor layer with low conductivity. The whole structure is sandwiched between two planar electrodes to which a DC voltage  $U_t$  is applied. Theoretical predictions on how the different spatio-temporal patterns depend on the parameters of the gas discharge, hardly exist. In [9, 15, 27, 28], an effective reaction-diffusion model in the two dimensions transversal to the current is proposed. Roughly, it consists of two nonlinear partial differential equations for the current  $J$  and the voltage  $U$  of the form

$$\partial_t U(x, y, t) = \mathcal{F}(U, J) \quad , \quad \partial_t J(x, y, t) = \mathcal{G}(U, J) \quad , \quad (7.1)$$

where the nonlinear operators  $\mathcal{F}$  and  $\mathcal{G}$  contain spatial derivatives  $\partial_x$ ,  $\partial_y$  and possibly also integral kernels. The model is of reactor-inhibitor form as studied extensively in the context of chemical and biological systems in the past decades. If applicable to gas discharges, this identification lays a connection to a realm of analytical and numerical results on reaction-diffusion systems.

To test whether a model like (7.1) is applicable to the gas discharge system, we will focus on its temporal oscillations that can occur in a spatially completely

homogeneous mode [11]; hence a one-dimensional approximation is appropriate. Similar oscillations have been observed in [16, 18, 19, 23], and similar effective models for current  $J$  and voltage  $U$  of the general form (7.1) have been proposed in [5, 18, 19, 22, 26].

Why have different authors come up with the same type of model? The equation for  $U$  directly results from the simplest form of an external electric circuit: a semiconductor layer of thickness  $d_s$ , linear conductivity  $\sigma_s$  and dielectricity constant  $\epsilon_s$  will evolve as

$$\partial_t U = \frac{U_t - U - R_s J}{T_s} \quad (7.2)$$

where  $U_t$  is the voltage on the total system,  $J$  is the total current, and  $U = \int_0^{d_g} E dz$  is the voltage over the gas discharge which is the electric field  $E$  integrated in the  $z$  direction over the height  $d_g$  of the discharge. For the experiments in [11],  $R_s = d_s/\sigma_s$  is the resistance of the whole semiconductor layer, and  $T_s = \epsilon_s \epsilon_0 / \sigma_s = C_s R_s$  is the Maxwell relaxation time of the semiconductor. In other experimental systems, the quantities  $R_s$  and  $T_s$  can have different realizations. Hence the form of the equation for  $U$  in a reaction-diffusion model (7.1) is clear.

However, the equation for  $J$  in a reaction-diffusion model as (7.1) is based on the plausibility of such a model due to analogies with other pattern forming systems and on various attempts to derive such a form with ad hoc assumptions from gas discharge physics. Different choices have been suggested by different authors, but one feature is generic: to be physically meaningful, the current-voltage characteristics of the glow discharge has to be a stationary solution, so  $\mathcal{G}(U, J) = 0$  on the characteristics. Beyond that, there are different suggestions for the functional form of  $\mathcal{G}$  and the intrinsic time scale.

Let us investigate the predictions on oscillations within a reaction-diffusion model in its simplest form. Assume that the model is defined as:

$$\begin{aligned} \partial_t U &= \frac{U_t - U - R_s J}{T_s} , \\ \partial_t J &= a (U - U_{CVC}(J)) . \end{aligned} \quad (7.3)$$

$T_s$  is the Maxwell time scale of the semiconductor layer, while  $1/a$  is the other time scale coming from gas discharge part. The stationary solution of (7.2) is the load line, and the stationary solution of (7.3) has to be the current-voltage characteristic of the gas discharge  $U = U_{CVC}(J)$ . The intersection of these two lines is the stationary solution of the equations above. Linearizing about this stationary solution, we find the stability matrix:

$$\partial_t \begin{pmatrix} \delta U \\ \delta J \end{pmatrix} = \mathbf{A} \cdot \begin{pmatrix} \delta U \\ \delta J \end{pmatrix} , \quad \mathbf{A} = \begin{pmatrix} -1/T_s & -R_s/T_s \\ a & -a U' \end{pmatrix} , \quad (7.4)$$

where

$$U' = \left. \frac{\partial U_{CVC}(J)}{\partial J} \right|_{\text{stat. point}} \quad (7.5)$$



is a short notation of the first derivative of the current-voltage characteristic at the stationary point.

The question that we would like to answer is: how does the stability of the stationary point depend on the slope of load line and J-U characteristics; that is: in which parameter range of  $R_s$  and  $U'$  can we expect to find oscillations.

First, the analysis of the stability matrix shows that the stationary point is dynamically stable and does not exhibit oscillations, if  $U'$  is positive. In other words, negative differential conductivity is a necessary condition for the onset of oscillations.

Second, in the case of negative differential conductivity  $U' < 0$ , we restrict the analysis to the case of the previous and present chapter where the characteristics of the gas discharge in the intersection point has a larger slope than the load line; this means that

$$U' + R_s > 0. \quad (7.6)$$

The stability of the stationary point then depends on

$$\text{sign}(U' + r) \quad , \quad r = \frac{1}{aT_s}. \quad (7.7)$$

If  $|U'| < r$ , the stationary point is linearly stable, while for  $|U'| > r$ , it is unstable (and the character of the instability then depends on the sign of  $(|U'| + r)^2/r - 4R_s$ ). For negative differential conductivity, the stability therefore depends on the unknown time scale  $1/a$  which would have to be determined from the full model. However, we will see below that the full model gives results in contradiction with a reaction-diffusion model of type (7.1) or (7.3).

If a model like (7.1) or (7.3) is applicable to oscillations in glow discharge systems, then the following predictions apply:

- 1) an oscillation can only occur in a region of negative differential conductivity of the glow discharge characteristics,
- 2) only a single period can be formed, period doubling is not possible, since this requires at least three independent parameters,
- 3) in a phase space plot in  $U$  and  $J$ , the trajectory of an oscillation can intersect the load line  $U = U_t - R_s J$  only parallel to the  $J$ -axis (since  $\partial_t U = 0$  and  $\partial_t J \neq 0$ ), and it can intersect the characteristics of the glow discharge  $U = U(J)$  only parallel to the  $U$ -axis (since  $\partial_t U \neq 0$  and  $\partial_t J = 0$ ).

### 7.3 A period doubling cascade

We now return to our classical glow discharge model [13,29,85] from the previous chapter, solve it numerically and confront its results with the predictions above.

Though our choice of parameters was guided by the experiments in [11], we explored the parameter space beyond experimental limits. While the parameters characterizing the gas discharge remained the same, system size and resistivity of the semiconductor layer differ from the values of the previous chapter by a factor 2 and by an order of magnitude, respectively. The explicit parameters are: the secondary emission coefficient  $\gamma = 0.08$ , the mobility ratio  $\mu = 0.0035$  for nitrogen and the dimensionless system size  $L = 50$  which amounts to 1.4 mm at a pressure of 40 mbar. The external circuit has  $\mathcal{R}_s = 30597$ ,  $\tau_s = 7435$  and a dimensionless total voltage  $u_t$  in the range between 18 and 20. This corresponds to a GaAs layer with  $\epsilon_s = 13.1$ , conductivity  $\sigma_s = (2.6 \cdot 10^5 \Omega \text{cm})^{-1}$  and thickness  $d_s = 1.5 \text{mm}$ , and a voltage range between 513 and 570 V.

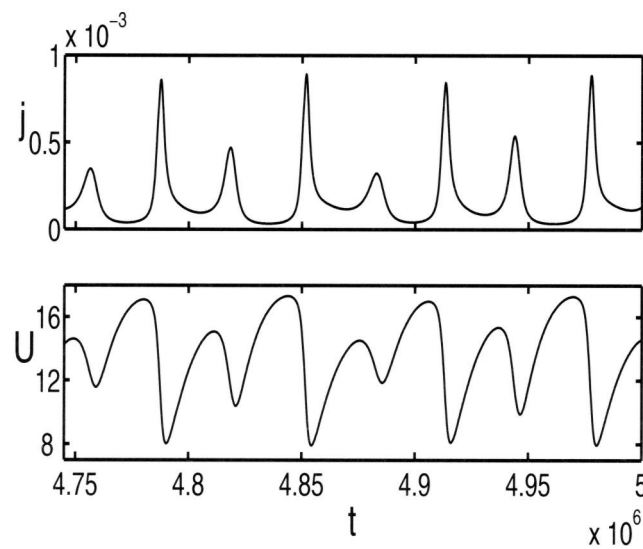


Figure 7.1: Spontaneous oscillations of current  $j$  and voltage  $u$  as a function of time  $\tau$  for  $\gamma = 0.08$ ,  $\mu = 0.0035$ ,  $L = 50$ ,  $\mathcal{R}_s = 30597$ ,  $\tau_s = 7435$ , and applied total voltage  $u_t = 19$ .

Fig. 7.1 shows electric current  $j$  and voltage on the gas discharge  $u$  as a function of time for a total stationary voltage  $u_t = 19$  applied to the complete system of gas discharge and semiconductor layer. The system exhibits spontaneous oscillations with sharp current peaks: when the voltage  $u$  on the gas layer becomes high enough, the discharge ignites. The conductivity of the gas increases rapidly and produces a current pulse that deposits a surface charge on the gas-semiconductor interface. Therefore the voltage  $u$  over the gas layer

breaks down. Due to the low conductivity of the semiconductor, the voltage  $u$  recovers only slowly. Eventually the gas discharge ignites again, and the cycle is repeated.

Note that the oscillations in Fig. 7.1 are not quite periodic. This is not due to initial transients since the system is observed after the long relaxation time  $\tau = 4.745 \cdot 10^6$ . The nature of this temporal structure becomes clear when the trajectory is plotted in the plane spanned by current  $j$  and voltage  $u$  in Fig. 7.2(c). The figure contains the data of the time span from  $\tau = 3 \cdot 10^6$  to  $6 \cdot 10^6$  which amounts to approximately 90 current pulses. The phase space plot shows that the system is actually periodic, with a period of 8 current pulses. Fig. 7.1 shows precisely one period.

This discovery raises the question whether our system actually follows the well-known scenario of period doubling. Indeed, it does. Fig. 7.2(a) for  $u_t = 18$  shows an oscillation where one current pulse is repeated periodically as observed experimentally in [11]. For  $u_t = 18.5$ , a period consists of two current pulses as can be seen in Fig. 7.2(b). For  $u_t = 19$ , the period is 8 pulses as in Fig. 7.1 and Fig. 7.2(c). For  $u_t = 20$ , the system seems to have reached the chaotic state as can be seen in Fig. 7.2(d).

A more detailed comparison of the experiments in [11] with simple oscillations as in Fig. 7.2(a) has been given in previous chapter, and we only state here that there is semi-quantitative agreement of several features. Here we emphasize that period doubling events in glow discharges have been observed experimentally in other systems [61–66]. However, this was always in systems with more complicated geometries like long narrow tubes, and the authors allude to general knowledge on nonlinear dynamics rather than to solutions of explicit models. We state that period doubling can be a generic feature of a simple, strictly one-dimensional glow discharge when coupled to the simple circuit (7.2). We propose to search experimentally for a period doubling route to chaos in such simple systems which would then allow quantitative comparison with theory.

## 7.4 Local versus global differential conductivity and the validity of a reaction-diffusion approximation

Let us return to the initial question: is a 2-component reaction diffusion model like (7.1) with negative differential conductivity appropriate for the present system? At the end of section 7.2, we gave a list of predictions for the reaction diffusion model (7.1) to be applicable. Prediction 2 is falsified by the observation of period doubling. Prediction 3 is also falsified by a simple check of either of the four figures in Fig. 7.2: the trajectories definitely do not intersect with the characteristics with the angle prescribed by (7.1) in the upper part of the figures that represent the rapid current pulses.

There rests prediction 1: is negative differential conductivity required for the oscillations to occur? First of all, we note that the characteristics is a global

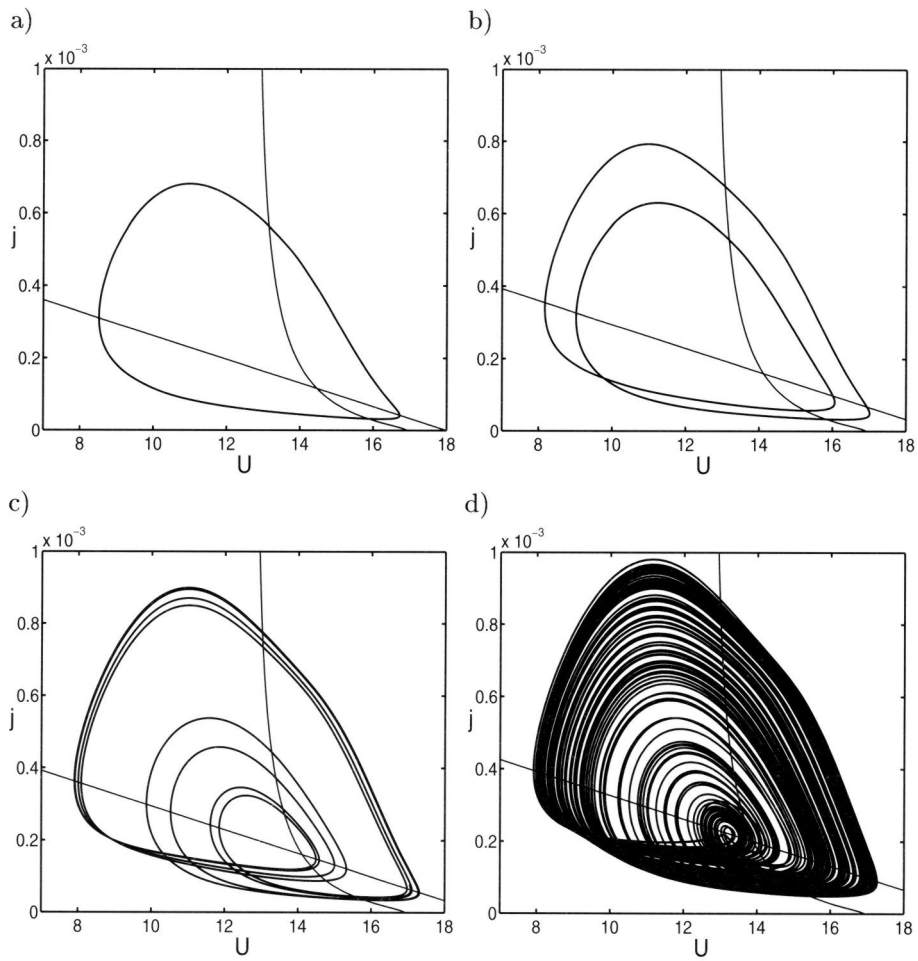


Figure 7.2: Phase space plots of the trajectories of the oscillations in the plane of current  $j$  and voltage  $u$ . The time range is  $3 \cdot 10^6 \leq \tau \leq 6 \cdot 10^6$  in all figures. Shown are the orbits, the straight load line  $u = u_t - \mathcal{R}_s j$  and the curved current voltage characteristics  $u = u(j)$  of the gas discharge [28]. The intersection of load line and characteristics marks the stationary solution of the system. (c) represents the data of Fig. 7.1 with total voltage  $u_t = 19$ , (a) is for  $u_t = 18$ , (b) for  $u_t = 18.5$ , (d) for  $u_t = 20$ .

property of the whole discharge layer with its boundary conditions [85]. In our model, negative differential conductivity (NDC) seems to exist only at the global level while the local differential conductivity in our model is always positive: the field dependent stationary ionization is  $n_+ = |\mu_e E| \alpha_0 e^{-E_0/|E|} / \beta$  according to (4.6); hence the local conductivity increases monotonically with the applied field  $|E|$  (in the equilibrium state homogeneous solutions gives  $|E| \alpha(|E|) / \beta$  for the conductivity). The global negative differential conductivity is due to electrode effects being much stronger than bulk recombination  $\beta$ . Anyway, the equilibrium current is a monotonically increasing function of  $E$  (proportional to  $|E|^2 \alpha(|E|)$ ) and it is obvious that there is no NDC of the current-voltage characteristic on the local level of description, so oscillations definitively coexist with a local positive differential conductivity.

But the reaction-diffusion approximation (7.3) would predict that global negative differential conductivity  $\partial_j U < 0$  is required for the stationary state to evolve into oscillations. In the next subsection, we give an example of the oscillations emerging in the full gas discharge model in the presence of both local and global positive differential conductivity.

#### 7.4.1 Oscillations despite local and global positive differential conductivity

Throughout this thesis, the system with the gas discharge region of 0.5mm was not investigated, though experimentally it shows oscillations as well, and similar behavior as the other - larger system of 1mm. The reason for that lies in the sensitivity of current-voltage characteristic on secondary emission coefficient, as it has been already explained in Chapter 6.

We were interested to see if that system with current-voltage characteristics of ‘mix<sub>I</sub>’ type (for ‘experimental’  $\gamma$ ), can nevertheless give oscillations. Indeed, it has been found that the system bifurcates to oscillatory regime, for the range of parameters corresponding to experimental values, except for voltages which are substantially larger. Physically, these voltages are high enough to destroy the experimental cell. Nevertheless, this simulation (Figs.7.3 and 7.4) is very important, since it confronts the established theoretical concepts.

For the set of parameters ( $\gamma = 0.08$ ,  $\mu = 0.0035$ ,  $L = 18$ ,  $\mathcal{R}_s = 5 \cdot 10^5$ ,  $\tau_s = 121500$ , and  $u_t = 529.4$ ), the stationary solution is  $(j_0, u_0) = (1.04 \cdot 10^{-3}, 9.406)$ , and the eigenvalue is the complex number  $\lambda = 3.76 \cdot 10^{-6} \pm i 1.19 \cdot 10^{-3}$  with the small positive real part. That implies that the stationary solution is linearly unstable and that small perturbations will grow. Indeed, starting from the stationary state the build up and growth of the oscillations with the slow rate can be seen in Fig. 7.3 (solid line).

The dashed line of Fig. 7.3 represents the result of the perturbation theory (Chapter 6) given by equations (6.51) and (6.52) where amplitude  $c$  and absolute phase  $\alpha_0$  are adjustable while all other parameters are fixed ( $\alpha = 90.84$  and  $r = 3449.3$ ). The agreement between results of the linear stability analysis and numerics is convincing.

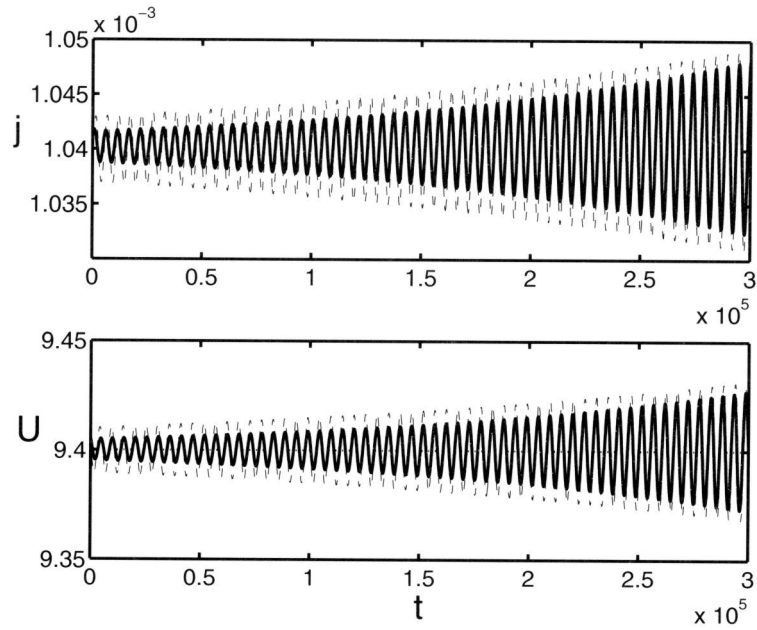


Figure 7.3: Spontaneous oscillations of current  $j$  and voltage  $u$  as a function of time  $\tau$  for  $\gamma = 0.08$ ,  $\mu = 0.0035$ ,  $L = 18$ ,  $\mathcal{R}_s = 5 \cdot 10^5$ ,  $\tau_s = 121500$ , and applied total voltage  $u_t = 529.4$  (solid lines) compared to the stability analysis result (dashed lines).

With the time, the amplitude of the oscillations grows and for  $\tau = 7 \cdot 10^5$  the limit cycle is reached. The phase space plot of these oscillations is presented in Fig. 7.4. It can be clearly seen that the load line intersects current-voltage characteristic in the part where current increases with the voltage. So, despite the positive differential conductivity of the current-voltage characteristics, oscillations do exist so as the limit cycle. Therefore, this numerical example directly confirmed that reaction-diffusion approximation is not applicable to our complex system, and that oscillations are possible even in the presence of global positive differential conductivity.

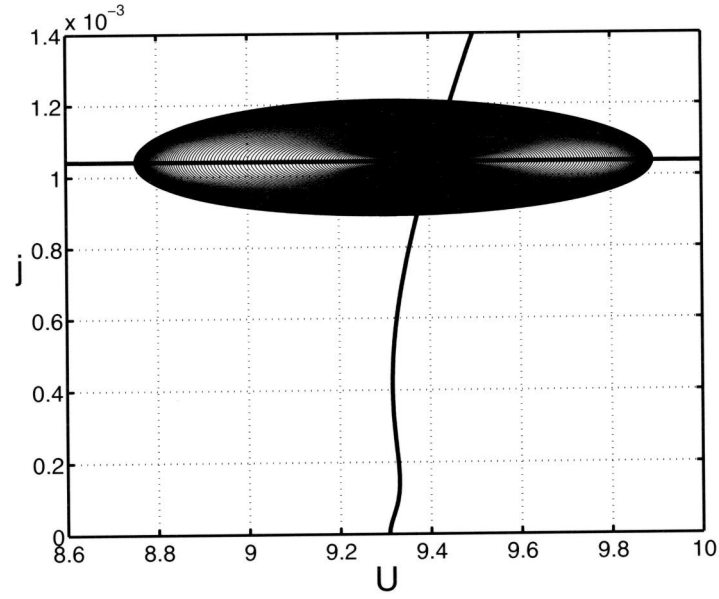


Figure 7.4: Phase space plot of the data from Fig. 7.3 but for the longer time  $\tau = 7 \cdot 10^5$  and with current-voltage-characteristics and load line

## 7.5 A systematic model reduction

For the model reduction, we return to the model representation of Chapter 4. The gas discharge is modeled as

$$\partial_\tau \sigma = \partial_z(\mathcal{E}\sigma) + \sigma\mathcal{E}\alpha(\mathcal{E}), \quad (7.8)$$

$$\partial_\tau \rho = -\mu\partial_z(\mathcal{E}\rho) + \sigma\mathcal{E}\alpha(\mathcal{E}), \quad (7.9)$$

$$\rho(0, \tau) = 0, \quad (7.10)$$

$$\sigma(L, \tau) = \gamma\mu\rho(L, \tau), \quad (7.11)$$

$$\rho - \sigma = \partial_z \mathcal{E}, \quad (7.12)$$

while the external circuit is described by

$$\partial_\tau u(\tau) = \frac{u_t - u(\tau) - \mathcal{R}_s j(\tau)}{\tau_s}, \quad (7.13)$$

$$u(\tau) = \int_0^L \mathcal{E}(z, \tau) dz \quad (7.14)$$

with the Maxwell time of the semiconductor  $\tau_s = C_s \mathcal{R}_s$  and with a spatially conserved total current [which follows in the standard way from (7.8), (7.9) and (7.12)]

$$j(\tau) = \partial_\tau \mathcal{E} + \mu\rho\mathcal{E} + \sigma\mathcal{E}, \quad \partial_z j(\tau) = 0. \quad (7.15)$$

### 7.5.1 Adiabatic elimination of the electrons

Now consider that in the stationary case, the total particle current is conserved, but accordingly to the boundary condition (7.10), at  $z \rightarrow 0$  it is mainly carried by the electrons and at  $z \rightarrow L$ , it is mainly carried by the ions (7.11). The electric field stays of order unity throughout the system. Therefore  $\mu\rho$  should scale like  $\sigma$ :  $O(\mu\rho) = O(\sigma)$ . Now the field  $\mathcal{E}$  and the system size  $L$  are of order unity, and therefore also  $\partial_z \mathcal{E} = \rho - \sigma$ . The conclusion is that  $\rho = O(1)$ , and hence  $\sigma = O(\mu)$ . Therefore we substitute  $s = \sigma/\mu$  where  $s$  is now of order unity. This expresses more clearly that the electrons contribute to the current in order unity, but to the space charge only in order  $\mu$ . To focus on the dynamics of the ions, a new time scale  $\bar{\tau} = \mu\tau$  is chosen. Then the model attains the form

$$\mu \partial_{\bar{\tau}} s = \partial_z(\mathcal{E}s) + s\mathcal{E}\alpha(\mathcal{E}) , \quad (7.16)$$

$$\partial_{\bar{\tau}} \rho = -\partial_z(\mathcal{E}\rho) + s\mathcal{E}\alpha(\mathcal{E}) , \quad (7.17)$$

$$\rho(0, \bar{\tau}) = 0 , \quad (7.18)$$

$$s(L, \bar{\tau}) = \gamma\rho(L, \bar{\tau}) , \quad (7.19)$$

$$\rho - \mu s = \partial_z \mathcal{E} . \quad (7.20)$$

This rescaling now allows to take two essential approximations in the limit of small  $\mu$ : First,  $s$  evolves on the short time scale  $\tau = \bar{\tau}/\mu$  while  $\rho$  evolves on the long time scale  $\bar{\tau}$ . For small  $\mu$ , the electrons therefore can be eliminated adiabatically from the ion motion. Hence on the ion time scale  $\bar{\tau}$ , the electron distribution is equilibrated or ‘slaved’ and we can approximate

$$\left( \partial_z + \alpha(\mathcal{E}) \right) [s\mathcal{E}] \approx 0 . \quad (7.21)$$

Second, the contribution of the electrons to the space charge is negligible for small  $\mu$ :

$$\rho \approx \partial_z \mathcal{E} . \quad (7.22)$$

This can also be understood as follows: electrons and ions are generated in equal amounts, but the electrons rapidly leave the system while the ions move slowly and therefore reach much higher concentrations.

As a consequence of the differential equation (7.21) and the boundary condition (7.19), the electron density at position  $z$  now can be completely expressed by the instantaneous ion density at the boundary  $L$  and the field  $\mathcal{E}$  between  $z$  and  $L$  as

$$[s\mathcal{E}](z) = \gamma [\rho\mathcal{E}](L) e^{\int_z^L \alpha(\mathcal{E}(z)) dz} . \quad (7.23)$$

Using (7.17) and (7.21), the equation of motion for the ions becomes

$$\partial_{\bar{\tau}} \rho = -\partial_z \left( \rho\mathcal{E} + s\mathcal{E} \right) , \quad (7.24)$$

$$\rho = \partial_z \mathcal{E} \quad (7.25)$$

with  $s\mathcal{E}$  from (7.23). The gas dynamics is now expressed only by the fields  $\rho$  and  $\mathcal{E}$  that are related by  $\rho = \partial_z \mathcal{E}$ .



The equations for  $\rho$  can be integrated once to give  $\partial_{\bar{\tau}}\mathcal{E} + \rho\mathcal{E} + s\mathcal{E} = j(\bar{\tau})$  with  $\partial_z j(\bar{\tau}) = 0$  so the complete system can be expressed in terms of  $\mathcal{E}$  as

$$\partial_{\bar{\tau}}\mathcal{E} + \partial_z \frac{\mathcal{E}^2}{2} + s\mathcal{E} = j(\bar{\tau}) , \quad (7.26)$$

$$\partial_z [s\mathcal{E}] = -\alpha(\mathcal{E})s\mathcal{E} , \quad [s\mathcal{E}]|_L = \gamma \partial_z \frac{\mathcal{E}^2}{2} \Big|_L , \quad (7.27)$$

$$\partial_{\bar{\tau}}u(\bar{\tau}) = \frac{u_t - u(\bar{\tau}) - R_s j(\bar{\tau})}{\mu\tau_s} , \quad (7.28)$$

$$u(\bar{\tau}) = \int_0^L \mathcal{E}(z, \bar{\tau}) dz , \quad (7.29)$$

$$\text{where} \quad j(\bar{\tau}) = \partial_{\bar{\tau}}\mathcal{E}|_L + (1 + \gamma) \partial_z \frac{\mathcal{E}^2}{2} \Big|_L . \quad (7.30)$$

As the involved fields are related as  $\rho = \partial_z\mathcal{E}$ ,  $\mathcal{E} = \partial_z\phi$ , where  $u(\bar{\tau}) = \phi(L, \bar{\tau}) - \phi(0, \bar{\tau})$ , we have the choice whether to express the equations by integrals over  $\rho$  or by differentials of  $\phi$  or by integrals and differentials of  $\mathcal{E}$ . We choose  $\mathcal{E}$  as the independent variable since the notation becomes the most compact.

The physical dynamics is the one of the ions, furthermore the complete potential changes due to the external circuit. This dynamics can be accounted for by splitting the field into its value

$$\mathcal{E}_L(\bar{\tau}) = \mathcal{E}(L, \bar{\tau}) \quad (7.31)$$

at the cathode  $z = L$  as the dynamically most relevant place and the correction of the field due to the ions

$$\mathcal{E}(z, \bar{\tau}) = \mathcal{E}_L(\bar{\tau}) + \epsilon(z, \bar{\tau}) \quad \text{with} \quad \epsilon|_L = 0 , \quad (7.32)$$

where the ion density can be recovered through  $\partial_z\epsilon = \rho$ . The equation of motion for  $\epsilon$  becomes

$$\begin{aligned} \partial_{\bar{\tau}}\epsilon &= \mathcal{E}_L \partial_z \epsilon|_L - \mathcal{E}_L \partial_z \epsilon - \epsilon \partial_z \epsilon \\ &+ \gamma \mathcal{E}_L \partial_z \epsilon|_L \left( 1 - e^{\int_z^L dy \alpha(\mathcal{E}_L + \epsilon)} \right) . \end{aligned} \quad (7.33)$$

Note that if  $\epsilon(L, t) = 0$  initially at  $t = 0$ , then the equation of motion for  $\epsilon$  conserves this property for all times. For the equation of motion for  $\mathcal{E}_L$ , first the potential  $u(\bar{\tau})$  has to be expressed in terms of  $\mathcal{E}_L$  and  $\epsilon$

$$u(\bar{\tau}) = L \mathcal{E}_L(\bar{\tau}) + \int_0^L dz \epsilon(z, \bar{\tau}) . \quad (7.34)$$

In particular, the derivation of  $\partial_{\bar{\tau}}u$  in (7.28) requires to calculate

$$\begin{aligned} \int_0^L dz \partial_{\bar{\tau}}\epsilon &= \frac{\epsilon^2|_0}{2} + \mathcal{E}_L \epsilon|_0 \\ &+ L \mathcal{E}_L \rho_L \left( 1 + \gamma - \gamma \int_0^L \frac{dz}{L} e^{\int_z^L dy \alpha(\mathcal{E}_L + \epsilon)} \right) \end{aligned} \quad (7.35)$$

where we introduced the short hand notation

$$\rho_L = \partial_z \epsilon \Big|_L. \quad (7.36)$$

Introducing the small parameter  $k = L\mu\tau_s/\mathcal{R}_s$ , we find for  $\mathcal{E}_L$

$$\begin{aligned} \partial_{\bar{\tau}} \mathcal{E}_L = & -(1 + \gamma) \mathcal{E}_L \rho_L + \frac{u_t - L\mathcal{E}_L - \int_0^L dz \epsilon}{(1 + k) \mathcal{R}_s} \\ & + \frac{k}{1 + k} \left( \mathcal{E}_L \rho_L \gamma \int_0^L \frac{dz}{L} e^{\int_z^L dy \alpha} - \frac{\epsilon^2 \Big|_0 + 2\mathcal{E}_L \epsilon \Big|_0}{2L} \right). \end{aligned} \quad (7.37)$$

The parameter  $k$  is actually the ratio of capacitance of semiconductor and gas discharge layers. In more details:

$$k = L \frac{\mu\tau_s}{\mathcal{R}_s} = \epsilon_s \frac{\mu_+ d_g}{\mu_e d_s} = \frac{C_s}{C_g}, \quad (7.38)$$

$$C_s = \frac{\epsilon_0 \epsilon_s}{d_s}, \quad C_g = \frac{\tau_g}{\mathcal{R}_g} = \frac{(\alpha_0 \mu_+ E_0)^{-1}}{d_g / (\mu_e q_0)}. \quad (7.39)$$

When the thickness of gas discharge and semiconductor layer are of the same order of magnitude  $d_g/d_s = O(1)$ , the parameter  $k = \epsilon_s \mu d_g/d_s$  is a small parameter, since  $\epsilon_s = 13.1$ ,  $\mu = 0.0035$ , and therefore  $\mu\epsilon_s = 0.046$ .

As a result, the structure of explicit (but somewhat lengthy) equations (7.33) and (7.37) is

$$\partial_{\bar{\tau}} \epsilon(z, \bar{\tau}) = F(\epsilon, \mathcal{E}_L) \quad \text{and} \quad \partial_{\bar{\tau}} \mathcal{E}_L(\bar{\tau}) = G(\epsilon, \mathcal{E}_L).$$

So this is not a system of two scalars like previous authors have suggested, but a system of the scalar  $\mathcal{E}_L$  and the function  $\epsilon$ .

## 7.5.2 Comparison with a two-component reaction-diffusion system

The electric field  $\mathcal{E}_L$  at the cathode  $z = L$  determines the local bulk ionization rate  $\alpha$ , and it is closely related to the potential  $u$  over the gas discharge. We therefore take it as the first characteristic scalar variable for the state of the system. A second such scalar variable could be the ion density  $\rho_L$  at the cathode, since it characterizes the conductivity and therefore also the electric particle current  $\rho_L \mathcal{E}_L + [s\mathcal{E}]|_L = (1 + \gamma)\rho_L \mathcal{E}_L$  at the cathode. A two-component reaction-diffusion model could therefore consist of equations for the two scalars  $\mathcal{E}_L$  and  $\rho_L$ . But can it be derived from the present equations?

Taking the spatial derivative of (7.33) at  $L$ , we find the equation of motion for  $\rho_L$

$$\partial_{\bar{\tau}} \rho_L = -\rho_L^2 - \mathcal{E}_L \partial_z \rho \Big|_L + \gamma \rho_L \mathcal{E}_L \alpha(\mathcal{E}_L). \quad (7.40)$$

The evolution of  $\rho_L$  depends on its local value, on the value of the local field  $\mathcal{E}_L$  and also on the local derivative of  $\rho$ . If this derivative  $\partial_z \rho|_L = \partial_z^2 \epsilon|_L$  could be neglected, we would have derived a two-component model.

However, it is not possible to neglect  $\partial_z \rho|_L$ . This can be easily seen in the Townsend limit of very small space charges where the term  $-\rho_L^2$  in (7.41) can be neglected. Whether  $\rho_L$  grows or decays, therefore depends on the sign of  $\gamma \rho_L \alpha(\mathcal{E}_L) - \partial_z \rho|_L$ , i.e., on the local balance of generation and transport of ions.

An equation of motion for  $\partial_z \rho|_L$  in turn would depend on  $\partial_z^2 \rho|_L$  etc., so an infinite hierarchy of equations would have to be considered. The observation that a systematic reduction to a two-component problem is not possible, corresponds to the fact that the state of the gas discharge has been characterized by the full function  $\epsilon(z, \bar{\tau})$  or  $\rho(z, \bar{\tau})$  throughout the gas gap.

### 7.5.3 Summary of the derivation

To summarize, we have derived an analytical approximation of the our full model (7.8)–(7.15) that can be confronted with the suggested form (7.1). Electron and ion current in the gas are of the same order of magnitude. Since the electrons are much more mobile, their density is appropriately lower. Rescaling this density like  $s = \sigma/\mu$  and time like  $\bar{\tau} = \mu\tau$ , the electrons can be eliminated adiabatically in the limit of  $\mu \rightarrow 0$ . Space charges in the gas discharge are then due to the ions only  $\rho = \partial_z \mathcal{E}$ , and  $\rho$  can be expressed by  $\mathcal{E}$ . Splitting the field  $\mathcal{E}(z, t) = \mathcal{E}_L(t) + \epsilon(z, t)$  into the field on the cathode  $\mathcal{E}_L$  and a correction  $\epsilon$  with  $\epsilon(L, t) = 0$ , the complete system for  $\mu \rightarrow 0$  can be expressed by two dynamic equations

$$\partial_{\bar{\tau}} \mathcal{E}_L(t) = F(\mathcal{E}_L, \epsilon) \quad , \quad \partial_{\bar{\tau}} \epsilon(z, t) = G(\mathcal{E}_L, \epsilon) \quad . \quad (7.41)$$

While the equation for the time dependent parameter  $\mathcal{E}_L$  corresponds to the equation for  $U$  in (7.1), the space dependent field correction  $\epsilon$  within the gas layer cannot be reduced to a single component like the current  $J$  in (7.1) or the ion density at the cathode.

It is not justified to neglect all of  $\epsilon$  except for the dynamics of  $\rho_L$ . In the approximation of  $\epsilon \ll 1$ , the field at the cathode  $\mathcal{E}_L$  is simply proportional to the voltage  $u = L\mathcal{E}_L$ , and the ion density  $\rho_L$  is proportional to the conductivity  $(1 + \gamma)\rho_L$  at the cathode. But to neglect  $\partial_z \rho$  is not systematic at all, and obviously wrong, as can be seen from the results, presented previously.

Therefore, a two component reaction-diffusion equation for  $\rho_L$  and  $\mathcal{E}_L$  could result only from the completely unsystematic approximation  $(\partial_z \rho)|_L = 0$ . Rather the transport of ions  $\rho$  from the bulk of the gas towards the cathode is a central feature of the system. The field  $\epsilon(z, t)$  in (7.41) indeed accounts for the ion distribution within the gas gap with its intricate dynamics.

## Chapter 8

# 2D solutions: Spatio-temporal patterns

In this chapter, the system is finally investigated in two spatial dimensions. This means that next to the longitudinal direction through the layers, one transversal spatial direction is included. This 2D setting is sufficient for a full linear stability analysis of states that are homogeneous and isotropic in the transversal directions, since arbitrary 3D perturbations can be decomposed into 2D Fourier modes. In full numerical calculations, the 2D results give a reasonable indication for the full 3D behavior. The main aim is, of course, to understand the spatial and spatio-temporal patterns described in Chapter 3.

In Section 8.1, this is again done by linear stability analysis of the homogeneous stationary solution. Including transversal Fourier modes, and staying within the same parameter regime as in the previous chapters, either the purely temporal Hopf-bifurcation of Chapter 6 is preserved, or the bifurcation is of Turing-Hopf type as discussed in Chapter 2. This means that a state with some non-vanishing wave number grows more rapidly than the homogeneous one while also oscillating in time. This transition from a Hopf- to a Turing-Hopf-instability is in qualitative agreement with the experiments that show a transition from homogeneous oscillations to ‘blinking filaments’.

Next to the stability analysis, also the full time dependent 2D behavior is studied numerically. In Section 8.2, details of the numerical solution procedure are given, and in Section 8.3, some preliminary results are presented. They agree approximately with the stability analysis results during their linear growth phase, and then exhibit new dynamical features in the nonlinear and saturating regime. Finally, an outlook on open questions and possible future investigations is given.

## 8.1 Stability analysis

### 8.1.1 Formulation of the problem

The full model has been described in Chapter 4.3. To reduce the computational effort for the 2D dynamical problem, the electrons are eliminated adiabatically, as discussed in Section 7.5. In the limit of  $\mu \rightarrow 0$ , the gas discharge part of the system is described by the equations

$$\partial_x(s\mathcal{E}_x) + \partial_z(s\mathcal{E}_z) = -s|\mathcal{E}|\alpha(\mathcal{E}), \quad (8.1)$$

$$\partial_{\bar{\tau}}\rho + \partial_x(\rho\mathcal{E}_x) + \partial_z(\rho\mathcal{E}_z) = s|\mathcal{E}|\alpha(\mathcal{E}), \quad (8.2)$$

$$\Delta\phi = -\rho, \quad \mathcal{E} = -\nabla\phi, \quad (8.3)$$

with the boundary conditions for the glow discharge:

$$\rho(x, 0, \bar{\tau}) = 0, \quad s(x, L, \bar{\tau}) = \gamma\rho(x, L, \bar{\tau}). \quad (8.4)$$

For the semiconductor layer, the following equations apply:

$$\Delta\phi = 0, \quad j_s = \frac{\sigma_s}{\mu}\mathcal{E}, \quad D = \epsilon_s\mathcal{E}. \quad (8.5)$$

Across the boundary between gas layer and semiconductor layer, the electric potential is continuous while the jump in the  $z$  component of the electric field is determined by the surface charge as discussed in Section 4.2. Therefore, on the interface  $z = L$ , all  $z$  components of the vector fields from the left side  $L^-$  (gas discharge part) of the interface, and from the right side  $L^+$  (semiconductor layer) have to satisfy the boundary condition (4.19) for all  $x, y$  and  $\bar{\tau}$ , that is

$$\begin{aligned} \epsilon_s\mathcal{E}(L^+) - \mathcal{E}(L^-) &= -\epsilon_s\partial_z\phi|_{z=L^+} + \partial_z\phi|_{z=L^-} \\ &= q_s(\bar{\tau} = 0) + \int_0^{\bar{\tau}} d\bar{\tau} \left[ (1 + \gamma)(\rho\mathcal{E})(L^-) - \frac{\sigma_s}{\mu}\mathcal{E}(L^+) \right]. \end{aligned} \quad (8.6)$$

In the numerical procedure as well as in the perturbation analysis, the time derivative of this 'jump' condition is used:

$$\partial_{\bar{\tau}}\left(\epsilon_s\mathcal{E}(x, L^+, \bar{\tau}) - \mathcal{E}(x, L^-, \bar{\tau})\right) = \left[ (1 + \gamma)(\rho\mathcal{E})(x, L^-, \bar{\tau}) - \frac{\sigma_s}{\mu}\mathcal{E}(x, L^+, \bar{\tau}) \right]. \quad (8.7)$$

### 8.1.2 Linear perturbation analysis for transversal Fourier modes

Linear perturbation analysis is again performed about the stationary solutions which are obtained from the previous 1D calculations and denoted with the index 0. Therefore the ansatz is:

$$s(x, z, \bar{\tau}) = s_0(z) + s_1(z) e^{ikx + \lambda\bar{\tau}}, \quad (8.8)$$

$$\rho(x, z, \bar{\tau}) = \rho_0(z) + \rho_1(z) e^{ikx + \lambda\bar{\tau}}, \quad (8.9)$$

$$\mathcal{E}(x, z, \bar{\tau}) = \mathcal{E}_0(z) + \mathcal{E}_1(z) e^{ikx + \lambda\bar{\tau}}, \quad (8.10)$$

$$\phi(x, z, \bar{\tau}) = \phi_0(z) + \phi_1(z) e^{ikx + \lambda\bar{\tau}}. \quad (8.11)$$

The index 1 denotes a small linear perturbation about this stationary solution. In contrast to the ansatz used in Section 6.2.2, the system is also extended in the  $x$  direction. The wavelength of the distribution is characterized by the wavenumber  $k$ .

After insertion of the ansatz into the equation for the gas discharge, the system reads:

$$\begin{aligned}\partial_z s_1 &= -\left(\alpha(\mathcal{E}_0) + \frac{\partial_z \mathcal{E}_0}{\mathcal{E}_0}\right) s_1 - \frac{s_0}{\mathcal{E}_0} \rho_1 - \left(\frac{s_0}{\mathcal{E}_0} \alpha(\mathcal{E}_0) + \frac{\partial_z s_0}{\mathcal{E}_0} + s_0 \alpha'(\mathcal{E}_0)\right) \mathcal{E}_{1z} , \\ \partial_z \rho_1 &= \alpha(\mathcal{E}_0) s_1 - \left(\frac{\lambda + \rho_0 + \partial_z \mathcal{E}_0}{\mathcal{E}_0}\right) \rho_1 + \left(\frac{s_0}{\mathcal{E}_0} \alpha(\mathcal{E}_0) - \frac{\partial_z \rho_0}{\mathcal{E}_0} + s_0 \alpha'(\mathcal{E}_0)\right) \mathcal{E}_{1z} , \\ \partial_z \mathcal{E}_{1z} &= \rho_1 - k^2 \phi_1 , \\ \partial_z \phi_1 &= -\mathcal{E}_{1z} .\end{aligned}\tag{8.12}$$

The boundary conditions are:

$$\rho_1(0) = 0 , \quad \phi_1(0) = 0 , \quad s_1(L) = \gamma \rho_1(L) ,\tag{8.13}$$

where  $z = L$  is the boundary between gas layer and semiconductor layer.

In the semiconductor layer, the equation  $\Delta \phi = 0$  with the boundary condition  $\phi(L + L_s) = -u_t$  at the position of the cathode  $z = L + L_s$  has to be solved. For  $\phi_1$ , this means that we have to solve  $\Delta \phi_1 = 0$  with  $\phi_1(L + L_s) = 0$ . This problem has the explicit solution for  $L \leq z \leq L + L_s$ :

$$\phi_1(z) = C_1 \sinh(k(z - L - L_s)) ,\tag{8.14}$$

with the arbitrary amplitude  $C_1$ .

The 'jump' condition (8.7) can be expressed as

$$-C_1 k \cosh(kL_s) [\lambda \epsilon_s + \sigma_s / \mu] = \left[ (1 + \gamma)(\rho_0 \mathcal{E}_{1z} + \mathcal{E}_0 \rho_1) + \lambda \mathcal{E}_{1z} \right]_L .\tag{8.15}$$

Using the fact that the potential (8.14) is continuous on the boundary of the gas discharge region, we get

$$\phi_1(L) = -C_1 \sinh(kL_s) .\tag{8.16}$$

Now  $C_1$  in (8.15) can be substituted by  $\phi_1(L)$  through (8.16). The result is the second boundary condition at  $z = L$

$$\phi_1(L) = \frac{(1 + \gamma)(\rho_0 \mathcal{E}_{1z} + \mathcal{E}_0 \rho_1) + \lambda \mathcal{E}_{1z}}{\lambda \epsilon_s + \sigma_s / \mu} \frac{\tanh(kL_s)}{k} .\tag{8.17}$$

Now the semiconductor is integrated out, and we are left with four linear differential equations (8.12) and four boundary conditions (8.13), (8.17) that together determine the eigenvalue problem  $\lambda = \lambda(k)$ .

It is convenient to write the equations (8.12) again in terms of variables  $h$  and  $g$

$$h = \frac{s_1}{s_0} + \frac{\mathcal{E}_{1z}}{\mathcal{E}_0} \quad \text{and} \quad g = \mathcal{E}_0 \mathcal{E}_{1z} . \quad (8.18)$$

Now, we arrive at the compact form of the system:

$$\partial_z h = -\frac{\alpha'}{\mathcal{E}_0} g - \frac{k^2}{\mathcal{E}_0} \phi_1 , \quad (8.19)$$

$$\partial_z g = -\mathcal{E}_0 s_0 h - \frac{\lambda}{\mathcal{E}_0} g + j_{1z} - k^2 \phi_1 , \quad (8.20)$$

$$\partial_z j_{1z} = -k^2 \left( \lambda + \frac{J_0}{\mathcal{E}_0} \right) \phi_1 , \quad (8.21)$$

$$\partial_z \phi_1 = -\frac{1}{\mathcal{E}_0} g . \quad (8.22)$$

In the limit of  $k \rightarrow 0$  these equations should reproduce the equations (6.28)-(6.31) derived for the 1D case in the limit of  $\mu \rightarrow 0$ . And indeed, they do.

One should take care here with the generalization of the total current. From the charge conservation law, we have:

$$\nabla \cdot (\partial_{\bar{\tau}} \mathcal{E} + s\mathcal{E} + \rho\mathcal{E}) = \partial_z j_{1z} + \partial_x j_{1x} = 0 ,$$

where the component in  $z$  direction is

$$j_{1z} = \lambda \mathcal{E}_{1z} + s_1 \mathcal{E}_0 + s_0 \mathcal{E}_{1z} + \rho_0 \mathcal{E}_{1z} + \rho_1 \mathcal{E}_0 ,$$

while the component in the  $x$  direction is

$$j_{1x} = \lambda \mathcal{E}_{1x} + s_0 \mathcal{E}_{1x} + \rho_0 \mathcal{E}_{1x} \quad \text{with} \quad \mathcal{E}_{1x} = -i k \phi_1 .$$

The boundary conditions (8.13) and (8.17) can be rewritten as:

$$\phi_1(0) = 0 , \quad (8.23)$$

$$j_{1z}(0) = \frac{\lambda}{\mathcal{E}_0(0)} g(0) + J_0 h(0) , \quad (8.24)$$

$$j_{1z}(L) = \frac{\lambda}{\mathcal{E}_0(L)} g(L) + J_0 h(L) , \quad (8.25)$$

$$\phi_1(L) = \frac{j_{1z}(L)}{\lambda \epsilon_s + \sigma_s / \mu} \frac{\tanh(kL_s)}{k} \quad (8.26)$$

where

$$J_0 = (\mathcal{E}_0 s_0)(0) . \quad (8.27)$$

Here, one should note that in the definition of all these currents, scaling with  $\mu$  is already included since we work with  $s = \sigma/\mu$  and on the ion time scale  $\bar{\tau} = \mu\tau$ . In the limit of  $k \rightarrow 0$ , the appropriate boundary conditions from Section 6.2 are reproduced.

### 8.1.3 Formal solution and numerical implementation

The final set of the equations can be written in the form

$$\partial_z \begin{pmatrix} h \\ g \\ j_{1z} \\ \phi_1 \end{pmatrix} = M_\lambda(z) \begin{pmatrix} h \\ g \\ j_{1z} \\ \phi_1 \end{pmatrix}, \quad (8.28)$$

where the eigenvalue  $\lambda$  is a parameter and  $M_\lambda(z)$  is the matrix of the set of equations (8.19)-(8.22):

$$M_\lambda(z) = \begin{pmatrix} 0 & -\frac{\alpha'}{\varepsilon_0} & 0 & -\frac{k^2}{\varepsilon_0} \\ -J_e & -\frac{\lambda}{\varepsilon_0} & 1 & -k^2 \mathcal{E}_0 \\ 0 & 0 & 0 & -k^2(\lambda + \frac{J_0}{\varepsilon_0}) \\ 0 & -\frac{1}{\varepsilon_0} & 0 & 0 \end{pmatrix},$$

where  $J_0 = s_0 \mathcal{E}_0$ .

The boundary conditions (8.23) and (8.24) at  $z = 0$  can again be rewritten as orthogonality relations:

$$\begin{pmatrix} J_0 \\ \frac{\lambda}{\varepsilon_0(0)} \\ -1 \\ 0 \end{pmatrix} \cdot \begin{pmatrix} h \\ g \\ j_{1z} \\ \phi_1 \end{pmatrix}_0 = 0, \quad \begin{pmatrix} 0 \\ 0 \\ 0 \\ 1 \end{pmatrix} \cdot \begin{pmatrix} h \\ g \\ j_{1z} \\ \phi_1 \end{pmatrix}_0 = 0. \quad (8.29)$$

The general solution  $\vec{v}(z)$  of (8.28) is therefore a superposition of two independent solutions  $\vec{v}_1(z)$  and  $\vec{v}_2(z)$  of (8.28), that both obey (8.29) at  $z = 0$ :

$$\vec{v}(z) = \begin{pmatrix} h(z) \\ g(z) \\ j_{1z}(z) \\ \phi_1(z) \end{pmatrix} = c_1 \vec{v}_1(z) + c_2 \vec{v}_2(z). \quad (8.30)$$

As initial conditions, one can choose, e.g.,

$$\vec{v}_1(0) = \begin{pmatrix} 1/J_0 \\ 0 \\ 1 \\ 0 \end{pmatrix}, \quad \vec{v}_2(0) = \begin{pmatrix} 0 \\ \frac{\varepsilon_0(0)}{\lambda} \\ 1 \\ 0 \end{pmatrix}. \quad (8.31)$$

The components of the two solutions are denoted as  $\vec{v}_i(z) = (h_i(z), g_i(z), j_{1z,i}(z), \phi_{1,i}(z))$ .

The boundary conditions (8.25) and (8.26) at  $z = L$  also have the form of orthogonality relations

$$\begin{pmatrix} J_0 \\ \frac{\lambda}{\varepsilon_0(L)} \\ -1 \\ 0 \end{pmatrix} \cdot \begin{pmatrix} h \\ g \\ j_{1z} \\ \phi_1 \end{pmatrix}_L = 0, \quad \begin{pmatrix} 0 \\ 0 \\ 1 \\ -\frac{kL_s(1+\lambda\bar{r}_s)}{r_s \tanh(kL_s)} \end{pmatrix} \cdot \begin{pmatrix} h \\ g \\ j_{1z} \\ \phi_1 \end{pmatrix}_L = 0. \quad (8.32)$$



Now, each one of these two conditions determines the ratio  $C_1/C_2$  of the general solution (8.30):

$$\begin{aligned} C_1 \left[ j_{1z}^{(1)}(L) - \frac{\lambda}{\varepsilon_0(L)} g_1(L) - J_0 h_1(L) \right] + \\ C_2 \left[ j_{1z}^{(2)}(L) - \frac{\lambda}{\varepsilon_0(L)} g_2(L) - J_0 h_2(L) \right] &= 0, \\ C_1 \left[ j_{1z}^{(1)}(L) - \frac{kL_s (1 + \lambda\bar{\tau}_s)}{r_s \tanh(kL_s)} \phi_1^{(1)}(L) \right] + \\ C_2 \left[ j_{1z}^{(2)}(L) - \frac{kL_s (1 + \lambda\bar{\tau}_s)}{r_s \tanh(kL_s)} \phi_1^{(2)}(L) \right] &= 0. \end{aligned} \quad (8.33)$$

For the nontrivial solutions of (8.33), the determinant of the system

$$\Delta = \begin{vmatrix} j_{1z}^{(1)}(L) - \frac{\lambda}{\varepsilon_0(L)} g_1(L) - J_0 h_1(L) & j_{1z}^{(2)}(L) - \frac{\lambda}{\varepsilon_0(L)} g_2(L) - J_0 h_2(L) \\ j_{1z}^{(1)}(L) - \frac{kL_s (1 + \lambda\bar{\tau}_s)}{r_s \tanh(kL_s)} \phi_1^{(1)}(L) & j_{1z}^{(2)}(L) - \frac{kL_s (1 + \lambda\bar{\tau}_s)}{r_s \tanh(kL_s)} \phi_1^{(2)}(L) \end{vmatrix} \quad (8.34)$$

has to be equal to zero. This condition leads to a quadratic equation for the parameter  $\lambda$ .

Now the eigenvalue can be calculated numerically in the same way as in the 1D case. Again, we start with some initial estimate  $\lambda_0$ , solve the set of equations (8.19)-(8.22) obeying conditions (8.23)-(8.26), and calculate the next estimate of  $\lambda$  as a solution determined by the condition that determinant (8.34) has to be zero. This process has to be repeated until sufficient accuracy is reached. Actually, the condition

$$\left| \frac{\lambda_{k+1} - \lambda_k}{\lambda_{k+1}} \right| < 10^{-6}$$

is used in calculations to finish the iterations. For a faster convergence the under-relaxation is used. The iteration program is written in fortran 90 with complex variables; it is just an extension of the program used in the 1D case. Therefore, for the integration of the equations, a 4th order Runge-Kutta method is used. The number of grid points was usually 2000.

The solution of the set of the equations is now straightforward:

$$\vec{v}(z) = C \cdot \left[ \vec{v}_1(z) - \frac{r_s \tanh(kL_s) - kL_s(1 + \lambda\bar{\tau}_s)}{r_s \tanh(kL_s) - kL_s(1 + \lambda\bar{\tau}_s)} \frac{\phi_1^{(1)}(L)}{\phi_1^{(2)}(L)} \cdot \vec{v}_2(z) \right],$$

where  $C$  is a free constant.

### An improved numerical strategy

Unfortunately, using the same numerical method as in Chapter 6, only a partial result is obtained. For larger values of the wave number  $k \gg 1$ , the program did not give a result. Also, there was another problem: after the first bifurcation

in the dispersion relation, only one branch was found (see e.g., Fig. 8.1), while another one should exist as well. An explanation will be given later.

The reason why the previous algorithm did not succeed, was the poor accuracy of the integration routine which results from two sources. There is first the fact that the matrix of coefficients is poorly conditioned. This can be seen by noting that one column is much bigger than another one. A more precise measure of numerical ill-conditioning of a matrix is provided by computing the normalized determinant of the matrix. When the normalized determinant is small compared to one, the matrix is ill-conditioned. The normalized determinant is obtained by dividing the value of the determinant of the matrix by the square root of the product of the inner products of the vectors forming the rows of the matrix.

The second source is the so-called ‘build-up’ error. The difficulty arises because the resolution (8.30) requires combining numbers which are large compared to the desired solution; that is  $\vec{v}_1(z)$  and  $\vec{v}_2(z)$  were up to 3 orders of magnitude bigger than their linear combination, which is the actual solution. Hence significant digits are lost through subtraction. This error cannot be avoided by a more accurate integration unless all computations are carried out with higher precision. Godunov [93] proposed a method for avoiding the loss of significance which does not require multi-precision arithmetics and which is based on keeping the matrix of base solutions orthogonal at each step of the integration.

A modification of Godunov’s method [94], which is computationally more efficient and which yields better accuracy, is implemented in the new algorithm [95] which now gives results for all values of  $k$ . The main difference from the previous algorithm is that here we examine the base solutions (obtained by any standard integration method) at each mesh point and when they exceed certain nonorthogonality criteria we orthonormalize the base solution. We have to start with the initial conditions which are orthogonal to each other and not only to the boundary conditions:

$$\vec{v}_1(0) = \begin{pmatrix} -1 \\ -1 \\ -\frac{\lambda}{\varepsilon_0(0)} - J_0 \\ 0 \end{pmatrix}, \quad \vec{v}_2(0) = \begin{pmatrix} h_2 \\ 1 \\ \frac{\lambda}{\varepsilon_0(0)} + J_0 h_2 \\ 0 \end{pmatrix},$$

$$\text{where } h_2 = -\frac{1 + \frac{\lambda}{\varepsilon_0(0)}(J_0 + \frac{\lambda}{\varepsilon_0(0)})}{1 + J_0(\frac{\lambda}{\varepsilon_0(0)} + J_0)}.$$

Then using the method for the orthogonalization developed in [94] we are able to calculate the eigenfunctions very accurately, which allows us to find the eigenvalues. The correct eigenvalue is reached when the difference between  $\phi_1(L) = \phi_{1,1} + c\phi_{1,2}$  obtained by the integration as a superposition of two eigenfunctions, and the one given as the boundary condition  $\phi_1(L) =$

$\frac{j_{1z}(L) r_s \tanh(kL_s)}{kL_s (1+\lambda\bar{r}_s)}$  (8.26) is smaller than  $10^{-6}$ , where

$$c = -\frac{j_{1z}^{(1)}(L) - \frac{\lambda}{\varepsilon_0(L)} g_1(L) - J_0 h_1(L)}{j_{1z}^{(2)}(L) - \frac{\lambda}{\varepsilon_0(L)} g_2(L) - J_0 h_2(L)}$$

Otherwise, we could have used a slightly modified method for orthonormalization, and calculate the eigenvalues from the condition that the determinant of the coefficients vanishes, as before. Since we must solve equations (8.19)-(8.22) several times for different values of  $\lambda$ , we must insist that the orthonormalization is the same for all these solutions. In effect we must insist that the determinant is uniformly scaled in order for the successive approximations to  $\lambda$  to be consistent. Numerically this can be accomplished by determining the set of orthonormalization points and matrices to the solution corresponding to first initial guess for  $\lambda$  and thereafter applying the same matrices at the corresponding points for all succeeding solutions.

The program is written in C, and the integration method is one-step simple Runge-Kutta and on the domain  $L=36$  the number of grid points is varied from  $n=500$  to  $n=18000$  depending on  $k$  ( $k = 0 - 1000$ ).

#### 8.1.4 Results: dispersion relations

We now evaluate the dispersion relation  $\lambda = \lambda(k)$ . For certain parameter values, we expect to find some spatial structures. If they arise due to a linear instability, they will manifest themselves in the dispersion relation: there will be a band of Fourier modes with positive growth rate  $\text{Re}\lambda(k) > 0$ , with maximal growth rate for some non-vanishing wave number  $k$ , as already explained in Chapter 2.

The parameter sets at which the dispersion relation is evaluated, are chosen from the bifurcation diagram (Fig. 6.11) obtained from the one-dimensional perturbation analysis. Our aim here is to explore this range of parameters and see what happens if a transversal spatial dimension is added. On the bifurcation diagram given in Fig. 6.11, we choose three points in the upper, middle and lower part of the y-axis (corresponding to  $\mathcal{R}_s = 2 \cdot 10^5$ ,  $4 \cdot 10^5$ ,  $2 \cdot 10^6$ ) close to the line separating stable and unstable states and then explore these parameter values further, for higher values of the applied voltage.

Typically, we find that the dispersion relation function has a shape as presented in Fig. 8.1.

Here, we went to very large values of  $k$ , in a search for an instability for small wave length in a range of voltages  $u_t$  where the homogeneous  $k = 0$  mode is unstable. A logarithmic scale for the x-axis is used. For the same set of parameters  $L_s = 54$ ,  $L = 36$ ,  $\mathcal{R}_s = 2 \cdot 10^5$  (referred to as a position 1), but with  $u_t$  as a free parameter, the  $k = 0$  mode is always dominant; therefore no spatial structures are to be expected. Investigating the position 2 (where  $\mathcal{R}_s = 4 \cdot 10^5$  is the only difference) for different values of applied voltage, no essential change in the dispersion relation was observed, and the most unstable mode stays the homogeneous one with  $k = 0$ . Further increase of the semiconductor resistivity ( $\mathcal{R}_s = 2 \cdot 10^6$  - position 3) led to a finite wave length instability.

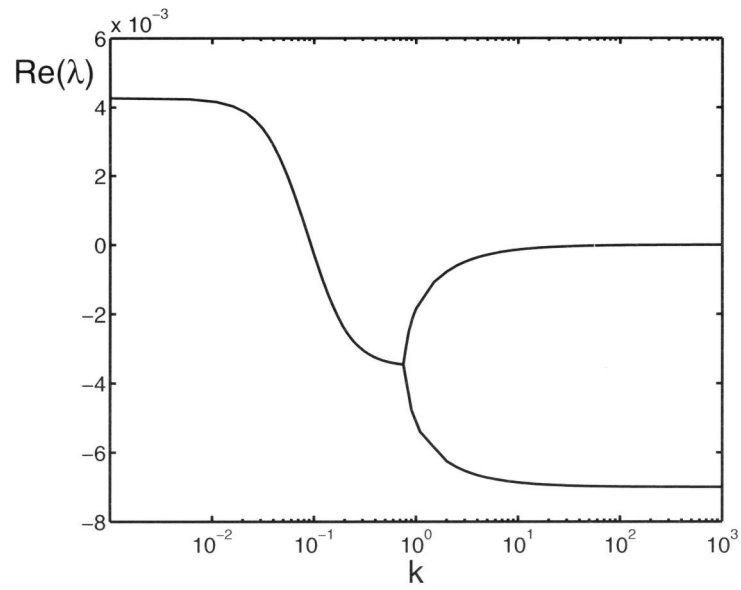


Figure 8.1: Real part of the dispersion relation for  $\mathcal{R}_s = 2 \cdot 10^5$  and  $u_t = 23$ . The system lengths  $L = 36$  and  $L_s = 54$  are kept fixed within the whole chapter.

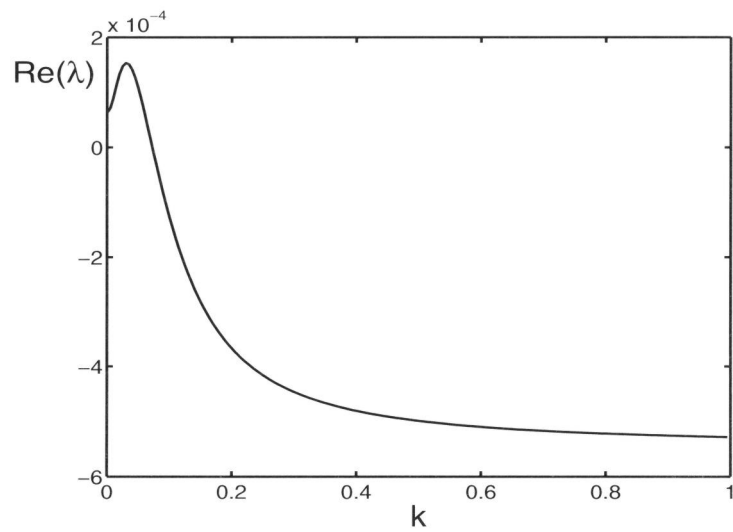


Figure 8.2: Real part of the dispersion relation for  $\mathcal{R} = 2 \cdot 10^6$  and  $u_t = 40$ .

Actually, for some non-vanishing, but very small value of  $k$ , a maximum of the real part of eigenvalue appears (see Fig. 8.2).

So far, we were concentrated on the real part of eigenvalue only, but in order to better understand the bifurcation of the dispersion relation we should investigate what happens with the imaginary part of the eigenvalue at that point.

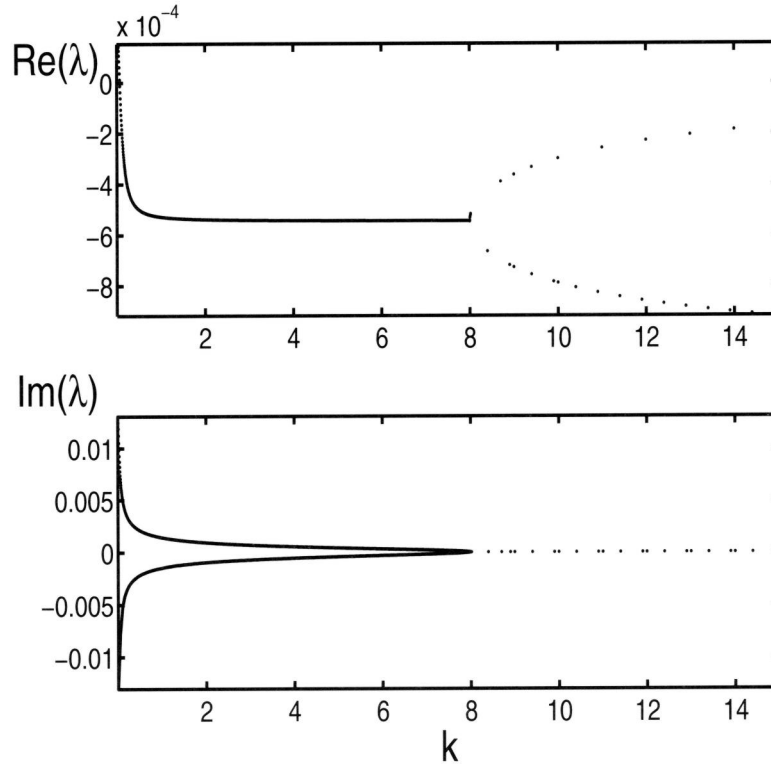


Figure 8.3: Real and imaginary part of the two branches of the dispersion relation for the same parameters as in Fig. 8.2 ( $\mathcal{R} = 2 \cdot 10^6$ ,  $u_t = 40$ ).

As can be seen in Fig. 8.3, up to some value of  $k_b$  the eigenvalue is a complex number (and since the complex conjugate is also a solution, there are always two solutions), and then at  $k_b$  the eigenvalue becomes purely real. Since eigenvalue branches should continue beyond  $k = k_b$ , we still should have two solutions for  $k > k_b$ , therefore the dispersion relation bifurcates into two real branches. The question is now whether a branch with purely real eigenvalues can become unstable (i.e., with  $\text{Re}\lambda(k) > 0$ ) for some  $k$ . For the parameters of Fig. 8.1, that does not happen as can be seen in Fig. 8.4.

For all parameter sets investigated, the branch with purely real eigenvalues never became dominant. Eigenvalues tend to approach (up to the investigated

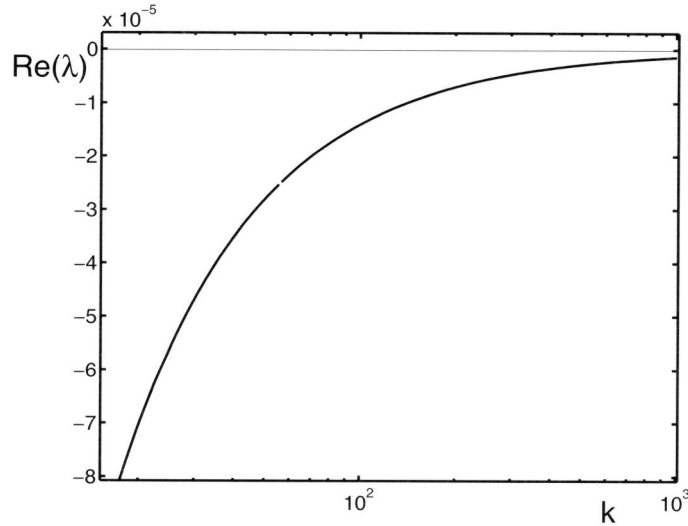


Figure 8.4: Real part of the dispersion relation in the limit of  $k \rightarrow \infty$  for the same parameters as in Figs. 8.2 and 8.3.

$k = 1000$ ) most often some value below zero or zero as shown on Fig. 8.4 i.e., they always stay negative. Furthermore, it has been observed (only twice) that even if the branch would reach positive values, the growth rate has been a way below the maximum value found for  $k \ll 1$ .

Beside the analysis of these 3 different positions in parameter space of resistivity and feeding voltage, where all other characteristics of the system were fixed and the only free parameter was the voltage, the influence of other parameters has been investigated as well. We choose position 1 for this investigation (corresponding to Fig. 8.1), therefore all parameters are kept fixed at the values  $L_s = 54$ ,  $L = 36$ ,  $\mathcal{R}_s = 2 \cdot 10^5$ ,  $j_0 = 3 \cdot 10^{-5}$ ,  $u_t = 23$  except for one that is being varied.

The following conclusions have been drawn:

**Dependence on  $L_s$ :** The most interesting observation is found when changing the width of the semiconductor layer. Increasing  $L_s$ , the  $k = 0$  mode stops being dominant and a maximum for very small values of the wavenumber ( $k < 0.1$ ) appears. In Fig. 8.5, the width of the semiconductor layer was changed from 10 to 150 in equal steps. In physical units, the width was changed from 0.27mm to 4.16mm. Keeping the rest of the parameters fixed as the dielectric constant  $\epsilon_s$  and resistivity  $\mathcal{R}_s$ , and only varying  $L_s$  actually means that the capacitance of the system is changed. So by decreasing the capacitance, long wave length instabilities can appear. Also the bifurcation point where the eigenvalues become purely real, moves considerably towards smaller  $k$ .

**Dependence on  $\mathcal{R}_s$ :** Increasing  $\mathcal{R}_s$ , the real part of the eigenvalue grows,

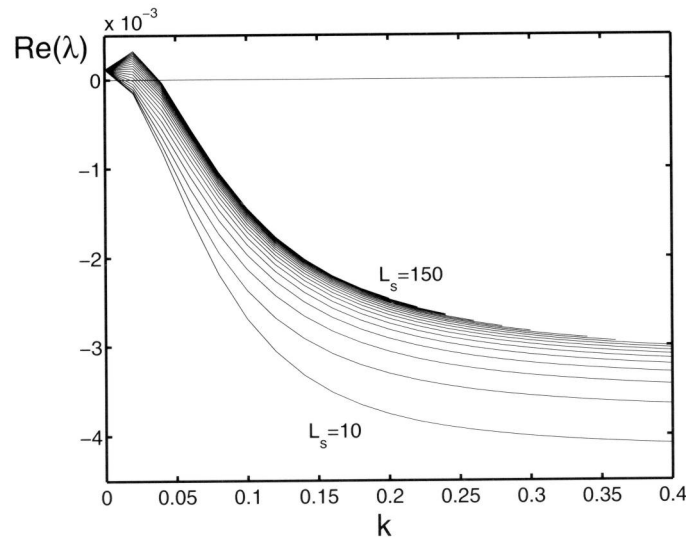


Figure 8.5: Dependence of the real part of the dispersion relation on the width of the semiconductor layer  $L_s$  for fixed parameters  $L = 36$ ,  $\mathcal{R} = 2 \cdot 10^5$  and  $u_t = 23$ , i.e., for the case of Fig. 8.1. The mode with maximal growth rate moves away from  $k = 0$  for increasing  $L_s$ .

though for this set of fixed parameters, the most unstable mode always stays at  $k = 0$ . The bifurcation point for complex versus real eigenvalues on the dispersion relation moves towards bigger wave-numbers, if the resistivity is increased.

**Dependence on  $L$ :**  $L$  is varied from 18 to 72. For the system sizes bigger than some critical value (approximately  $L = 30$ ), the real part of eigenvalue is positive and has a maximum for  $k = 0$  and for larger systems, the bifurcation point is shifted towards smaller wave-numbers. For the less interesting smaller system sizes, the real part of eigenvalue stays negative all the time, but the dispersion relation has a different form and up to  $k = 1$ , a bifurcation point was not observed.

**Dependence on  $j_0$ :** The current is varied by approximately two orders of magnitude and the real part of the eigenvalue went from negative to positive values, but always had a maximum at  $k = 0$ . The dispersion relation kept the same typical shape as in Fig. 8.1. The bifurcation point moves towards larger  $k$ , while decreasing the current. Physically, the increase of the current at the stationary point of the system corresponds to an increase of the applied total voltage.

**A remark on stationary spatial patterns:** The dispersion relation was not evaluated in the parameter range corresponding to the purely spatial patterns described in Section 3.4 (Chapter 3). If these patterns are described by

our model, we would expect the branch of purely real eigenvalues at  $k \geq k_b > 0$  to have a growth rate larger than the homogeneous  $k = 0$  mode.

## 8.2 2D computations: the numerical procedure

The problem is fully formulated in Section 8.1.1. For the numerical solution of these equations, a two-dimensional Cartesian coordinate system  $(x, z)$  is used, with a rectangular computational domain, which consists of two planar layers corresponding to the gas and the semiconductor layer.

### 8.2.1 Initial and boundary conditions

Computations are done in finite systems. Therefore lateral boundary conditions are required. On the lateral boundaries  $x = 0$  and  $x = L_x$ , either homogeneous Neumann conditions can be applied

$$\partial_x \rho(0, z, \bar{\tau}) = \partial_x s(0, z, \bar{\tau}) = \partial_x \phi(0, z, \bar{\tau}) = 0 , \quad (8.35)$$

$$\partial_x \rho(L_x, z, \bar{\tau}) = \partial_x s(L_x, z, \bar{\tau}) = \partial_x \phi(L_x, z, \bar{\tau}) = 0 , \quad (8.36)$$

or periodic boundary conditions

$$\rho(0, z, \bar{\tau}) = \rho(L_x, z, \bar{\tau}) , \quad s(0, z, \bar{\tau}) = s(L_x, z, \bar{\tau}) , \quad \phi(0, z, \bar{\tau}) = \phi(L_x, z, \bar{\tau}) , \quad (8.37)$$

for the densities  $s$  and  $\rho$  and the potential  $\phi$ .

When the system is considered infinitely extended in the  $x$  direction, Neumann boundary conditions create an axis with left-right-symmetry at their position while periodic boundary conditions create a periodic repetition of the structure. In both cases, the length imposed by these lateral boundary conditions should be accounted for in the analysis of the data. Typically we choose  $L_x$  several times larger than the expected wave length, and we work with periodic boundary conditions.

At the anode (on the line  $z=0$ ), the ion density vanishes according to (8.4), and the potential is set to zero as a gauge choice

$$\rho(x, 0, \bar{\tau}) = 0 , \quad \phi(x, 0, \bar{\tau}) = 0 ,$$

and at  $z = L_z$  (where  $L_z = L + L_s$  is a thickness of both layers together), we have

$$\phi(x, L_z, \bar{\tau}) = -u_t .$$

On the internal border between the gas and the semiconductor layer, we set

$$s(L, z, \bar{\tau}) = \gamma \rho(L, z, \bar{\tau}) \quad (8.38)$$

according to (8.4). On the border  $z = L$  between the two media, we also have to use the ‘jump condition’ (8.7)

$$\partial_{\bar{\tau}} \left( \epsilon_s \partial_z \phi|_{z=L^+} - \partial_z \phi|_{z=L^-} \right) = (1 + \gamma) \rho(x, L, \bar{\tau}) \partial_z \phi|_{z=L^-} - \frac{\sigma_s}{\mu} \partial_z \phi|_{z=L^+} . \quad (8.39)$$



As we are using the time differentiated form of the full boundary condition (8.6), we have to take care, that the full condition (8.6) is applied initially.

As the electrons are eliminated adiabatically, we need to specify the initial conditions only for the ion density  $\rho(x, z, 0)$  throughout the system including the surface charge at  $z = L$  in (8.6). In principle, any initial condition can be used like, e.g., any exponential function with a suitable choice of constants. However, as the system cannot deal with the large amplitudes, it is better to use the stationary solution as an initial condition. In this way, the program blow-up after a short time of integration is prevented. Still, for large times, very often  $\mathcal{E}_z$  becomes negative and then the program is terminated. More details about properties and limitations of the numerical procedure will be given later.

### 8.2.2 The numerical procedure

All equations are solved numerically using a finite-difference technique. The continuity equations are discretized in conservation form.

#### Grid

The computational domain is the rectangular region  $[0, L_x] \times [0, L_z]$  in the two dimensional Cartesian coordinate system  $(x, z)$ . It consists of two planar layers - gas and semiconductor (see Fig.8.6).

We use a uniform vertex-centered grid on the 'vertical'  $z$ -direction with nodes

$$z_j = j\Delta z, \quad \Delta z = L_z/N, \quad j = 0, 1, 2 \dots, N$$

and a uniform cell-centered grid with nodes

$$x_i = (i - \frac{1}{2})\Delta x, \quad \Delta x = L_x/M, \quad i = 1, 2, 3, \dots, M$$

on the 'horizontal'  $x$ -direction. The grid is spaced such that the internal border between semiconductor and gas region lies exactly on the grid line.

The densities  $s$  and  $\rho$  and the electric potential  $\phi$  are evaluated at the nodes of the grids, while the  $x$  and  $z$  components of the electric field ( $\mathcal{E}_x$  and  $\mathcal{E}_z$  respectively) are calculated at the edges of the computational cells.

#### Continuity equations

To obtain a finite-difference representation of equations (8.1) and (8.2), we first have to integrate them over the cell volume  $x_{i-1/2} \leq x \leq x_{i+1/2}$ ,  $z_{i-1/2} \leq z \leq z_{i+1/2}$ . Let us consider in detail only the equation for ions (8.2):

$$\frac{d\rho_{j,i}}{d\bar{t}} = \frac{(\mathcal{E}_x \rho)_{j,i-1/2} - (\mathcal{E}_x \rho)_{j,i+1/2}}{\Delta x} + \frac{(\mathcal{E}_z \rho)_{j,i-1/2} - (\mathcal{E}_z \rho)_{j,i+1/2}}{\Delta z} + f_{j,i}. \quad (8.40)$$

Note that subscripts  $j$  and  $i$  are related to 'vertical' and 'horizontal' directions respectively and  $f$  stands for the source term of the equation (8.2).

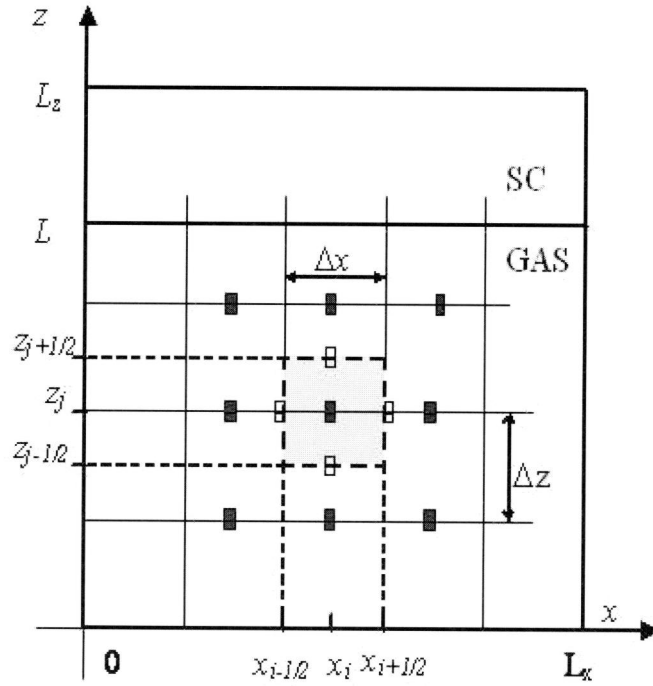


Figure 8.6: Computational domain and computational cell.

The choice of  $\rho_{j\pm 1/2, i\pm 1/2}$  at the corners of the computational cell determines the concrete discretization method of the convective terms of the equation (8.2). We used a third-order-upwind-biased scheme (see for example [96], p.83), which in the case of  $z$ -direction has the form

$$\rho_{j+1/2, i} = \frac{1}{6} \left[ \mathcal{E}_{z, j+1/2, i}^+ (-\rho_{j-1, i} + 5\rho_{j, i} + 2\rho_{j+1, i}) + \mathcal{E}_{z, j+1/2, i}^- (2\rho_{j, i} + 5\rho_{j+1, i} - \rho_{j+2, i}) \right], \quad (8.41)$$

where

$$\begin{aligned} \mathcal{E}_{z, j+1/2, i}^+ &= \max(0, \mathcal{E}_{z, j+1/2, i}), \\ \mathcal{E}_{z, j+1/2, i}^- &= \min(0, \mathcal{E}_{z, j+1/2, i}). \end{aligned} \quad (8.42)$$

The electric field components are calculated in the following way:

$$\mathcal{E}_{z, j+1/2, i} = \frac{\phi_{j, i} - \phi_{j+1, i}}{\Delta z}, \quad \mathcal{E}_{x, j, i+1/2} = \frac{\phi_{j, i} - \phi_{j, i+1}}{\Delta x}. \quad (8.43)$$

For the numerical time integration, we used the extrapolated second order BDF2 method (see for example [97], p.197)

$$\frac{3}{2}\rho^m - 2\rho^{m-1} + \frac{1}{2}\rho^{m-2} = \Delta\bar{\tau} F(\bar{\tau}_m, 2\rho^{m-1} - \rho^{m-2}), \quad m \geq 2, \quad (8.44)$$

where the superscript  $m$  denotes the time level  $\bar{\tau}_m = m\Delta\bar{\tau}$  with a step size  $\Delta\bar{\tau} > 0$ . Here  $F$  contains the discretized convective terms and the source term. Note that we have dropped spatial indices in Eq. (8.44). Since the two-step method needs  $\rho^0$  and  $\rho^1$  as starting values, the explicit Euler method

$$\rho^m = \rho^{m-1} + \Delta\bar{\tau} F(\bar{\tau}_m, \rho^{m-1}) \quad (8.45)$$

is used in the first step. Because of the explicit time integration, we are restricted by the standard CFL condition for the stability; see [96], Table 3.1.

The same space discretization technique (8.40)-(8.42) and the time integration method (8.44)-(8.45) are used also for the solution of the continuity equation for the electron density (8.1). Note that in this case the  $z$ -direction plays the role of time in (8.44) and (8.45), which is possible as long as  $\mathcal{E}_z > 0$ .

### The Poisson equation

To obtain a finite-difference approximation of Poisson's equation  $\Delta\phi = -\rho$  and  $\Delta\phi = 0$  we use the standard second order discrete scheme, so

$$\begin{aligned} \Delta\phi(x_i, z_j, \bar{\tau}_m) &\approx \frac{\phi_{j,i-1}^m - 2\phi_{j,i}^m + \phi_{j,i+1}^m}{(\Delta x)^2} + \frac{\phi_{j-1,i}^m - 2\phi_{j,i}^m + \phi_{j+1,i}^m}{(\Delta z)^2} \\ &+ O((\Delta x)^2, (\Delta z)^2). \end{aligned} \quad (8.46)$$

In the complete domain, we solve a single 'Poisson' equation with vanishing source term in the semiconductor and a source equal to  $\rho$  in the gas region

$$\frac{\phi_{j,i-1}^m - 2\phi_{j,i}^m + \phi_{j,i+1}^m}{(\Delta x)^2} + \frac{\phi_{j-1,i}^m - 2\phi_{j,i}^m + \phi_{j+1,i}^m}{(\Delta z)^2} = \begin{cases} 0, & \text{gas layer,} \\ \rho_{j,i}^m, & \text{SC layer.} \end{cases}$$

At the nodes which are lying on the border grid line between semiconductor and gas, instead of the Poisson equation, we solve the discrete version of the 'jump' condition (8.39). In every time step, we first solve the Poisson equation for the present distribution of the space charge; second, we calculate the electric field (hence, we find the source terms for the continuity equations - the ionization rates); then we find the densities of  $\rho$  and  $s$  for the next time step, and finally, the new value of the surface charge and induced jump of the field across the boundary is determined by equation (8.39).

The system of equations is solved with a symmetrical successive over-relaxation method (SSOR) (see for example [98], p.343). The iterations are stopped when the desired accuracy is reached and that is when the relative error is less than  $10^{-7}$ .

### 8.2.3 Testing the 2D program

When testing the 2D program on the results of the 1D program, one should keep the differences between 1D and 2D computations in mind:

- First of all, a 2D dynamical calculation is computationally more expensive than a 1D one.
- Second, in the 1D calculation the semiconductor layer with  $\Delta\phi = 0$  was completely integrated out and appeared only as a boundary condition  $u(L, \tau)$  for the gas discharge layer. In 2D, the computation  $\Delta\phi$  has to be done through both layers.
- Third, to reduce computation times, the electrons are eliminated adiabatically in the 2D computations. Therefore the initial electron distribution is not free which should be accounted for when comparing with programs without adiabatic elimination.

Different versions of the 1D program were used in order to test the correctness of the numerical results. The versions differ mostly in the form of the equations (describing the same model) and slightly in the numerical procedures which are applied. Here, a short overview of the programs, methods and results is presented:

$v_1$ : The first version of the 1D program is without adiabatic elimination of the electron dynamics. Therefore, the variables are not rescaled with mobility. The Poisson equation is solved on the whole interval  $[0, L + L_s]$ , and the jump condition is used on the internal border.

$v_2$ : The second version of the 1D program differs in the fact that the Poisson equation is solved only in the gas region, while the boundary value of  $\phi(L)$  is determined by the semiconductor dynamics described by Eq. (6.12).

This program was actually used for the computations presented in Chapters 6 and 7.

$v_3$ : The third version is simply the 1D reduction of the 2D program: it uses adiabatic elimination of the electrons and the Poisson equation is solved on the complete domain.

The numerical methods used in the different versions are almost the same (in spatial discretization and time integration), as the one already described above for the 2D program. We recall that for spatial discretization the third-order upwind-biased scheme is used for the convective terms. For the time integration, an extrapolated second order BDF2 method [97] is used, where, because of the explicit time integration, we are restricted by the standard Courant-Friedrichs-Levy Condition for stability. This means that the time step is calculated from step to step (adopting to the velocity of the particles  $\mathcal{E}$ ) by  $\Delta\bar{\tau} = \nu * \Delta z / \max |\mathcal{E}|$ , where  $\nu < 0.46$  guarantees the stability of our method.

Solving the Poisson equation requires a slightly different technique from the 2D case. The three-diagonal matrix which arises after the standard second order discretization is solved using the Thomas algorithm, whereas in the 2D case this problem is solved by an iterative method (SSOR). Of course, in the case of  $v_1$  and  $v_3$ , we solve a single 'Poisson' equation on the whole region (with vanishing source term in the semiconductor), and using the discrete version

of the jump condition on the boundary between gas and semiconductor. The difference between  $v_1$  and  $v_3$  is the calculation of the electron density. In  $v_3$ , the electron density is determined instantaneously, we compute it in explicit form by spatial integration.

As a first test, the 2D program was run with a planar  $z$ -dependent initial condition and only 4 grid points in the transversal  $x$  direction. The results coincided completely with the results of the  $v_3$  program. This was not at all surprising, but gave useful insight into which step size in  $z$  direction has to be used. Some examples are presented with more details in the next section. As we are using the (numerically derived) stationary solutions from Chapter 5 as a reference, all dynamical programs should reproduce these solutions. This comparison is done gradually; comparing first  $v_3$  with  $v_1$ , which confirmed that the adiabatic elimination is justified. Then  $v_1$  and  $v_2$  were compared, which showed that the role of the surface charge is properly taken into account and that the 'jump' condition is correctly derived. One should keep in mind that only starting from exactly the same initial condition (which was not obvious and straightforward to achieve), the solution is the same at each time instant, otherwise the system can end up in a different state if there are several stable solutions. The agreement between  $v_2$  and the stationary solutions from Chapter 5 was already tested in Chapters 6 and 7.

Since numerics is not the main topic of this thesis, all intermediate results and details of these analyses are skipped.

### 8.3 Preliminary results of the simulations

In this section, some results of the computations are reviewed. As a starting point, some properties of the numerical procedure are discussed. Furthermore, an example of the full PDE simulation is shown. Some conclusion are drawn both from the results on linear perturbation theory and a number of simulations within experimental range of parameters (see bifurcation diagram Fig. 6.11). The linearly unstable fastest growing mode is most often found only for  $k = 0$  or otherwise very small values of wave vector ( $k \ll 1$ ). For parameter regimes where  $k = 0$  is fastest growing, the previous results of linear stability analysis (developed for 1D case in Chapter 6) are applicable, and agreement 2D-1D shows consistency. New results are for  $k \neq 0$  fastest growing mode. Numerical simulations are compared to the prediction of stability analysis. Development of spatio-temporal structure is shown by one numerical example. In the last subsection, outlook and ideas for further investigations are outlined.

#### 8.3.1 Dependence on the numerical resolution

If the number of grid points is too small, this will influence the result, in particular, the amplitude of oscillations. For example, on a coarse grid of 200x90 points and for the complete parameter set  $\mathcal{R}_s = 2 \cdot 10^6$ ,  $L = 36$ ,  $L_s = 54$ ,  $u_t = 40$ ,  $\epsilon_s = 13.1$ ,  $\mu = 0.0035$ ,  $\gamma = 0.08$ , the amplitude of oscillations decreases

with time and the system relaxes to a state which is stationary in time and homogeneous in space. On the other hand, stability analysis gives a positive real part of the eigenvalue, so the system is not stable and small perturbation should grow. Therefore, the conclusion is that the grid used for this simulation is too coarse.

Fig. 8.7 shows this case. A word should be said about the presentation: Just like in Figs. 8.11, 8.13 and 8.14, the ion density  $\rho(x, L, \bar{\tau})$  on the gas semiconductor interface is shown as a function of transversal coordinate  $x$  and time  $\bar{\tau}$ . A comparison with full 2D profiles at a fixed instant of time as shown in Fig. 8.10 shows that the ion density on the boundary indeed represents the relevant spatial information very well.

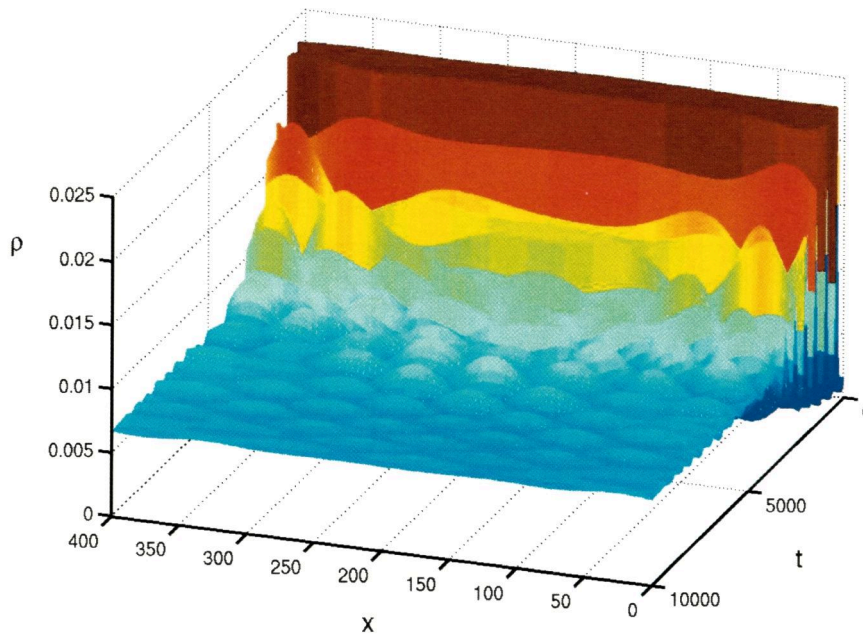


Figure 8.7: Evolution of the ion density  $\rho(x, L, \bar{\tau})$  on the gas semiconductor boundary for the parameters  $\mathcal{R} = 2 \cdot 10^6$  and  $u_t = 40$ , i.e., for the parameters explored previously in Figs. 8.2–8.4. The transversal length is  $L_x = 400$  and a coarse numerical grid of  $200 \times 90$  points is used.

Though the figure shows an erroneous decrease of the oscillation amplitude, it is shown nevertheless, since it is the only numerical example that we have found up to now where the system is initially completely homogeneous in the transversal direction and spontaneously creates a spatial pattern as it should according to its dispersion relation shown in Fig. 8.2. The computation shows a wave length 100 emerging spontaneously while the dispersion relation predicts the most unstable mode to have wave length 200. In all other cases, the theo-

retically predicted wave length was included as a very small perturbation in the initial conditions and then indeed amplified.

If the grid is fine enough (900x275), for the same set of parameters, the amplitude of oscillations grows as predicted from stability analysis. Interestingly enough, the temporal period of oscillations is the same in both cases and coincides with the one calculated from stability analysis.

This parameter set is investigated further in Subsection 8.3.4, while we here only emphasize the necessity of a sufficiently fine grid.

### 8.3.2 A limitation of the numerical algorithm

A major limitation of our numerical simulations is that the longitudinal electric field  $\mathcal{E}_z$  has to stay positive everywhere. When the amplitude of oscillations becomes too large, the field becomes negative at some points and the computations break down. Physically, this scenario is possible, but it leads to numerical problems in our present program. The way to avoid this is to start with stationary solutions and to choose the parameters in such a way that nonlinear saturation sets in at low values of the amplitude.

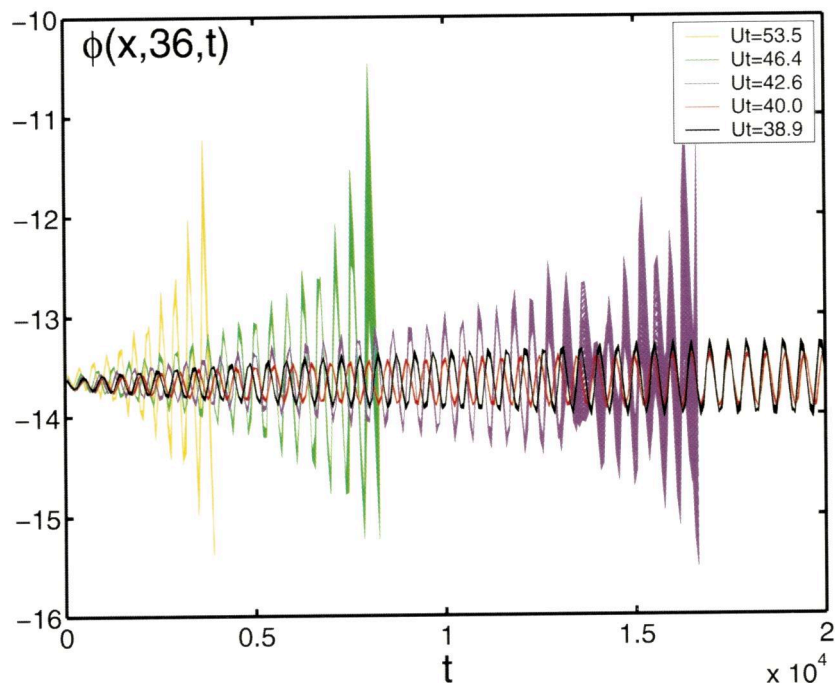


Figure 8.8: Potential as a function of time for  $\mathcal{R}_s = 2 \cdot 10^6$  and for applied voltages  $u_t = 53.5, 46.4, 42.6, 40.0, 38.9$ .

The consequences of different parameter choices are shown in Fig. 8.8. The figure shows the evolution of the potential  $\phi(x, L, \bar{\tau})$  on the internal border at  $z = L$  as a function of time. The potentials are actually plotted for all values of  $x$ , but the homogeneous oscillations are so predominant that the oscillations look similar to the 1D case. Nevertheless, we can observe the formation of spatial structures since on top of these temporal oscillations there is a spatial modulation, and one example will be discussed later in more detail.

It can be seen in Fig. 8.8 that for high values of the applied voltage  $u_t$ , the numerical procedure is terminated. This occurs when  $\mathcal{E}_z < 0$  somewhere in the system, as discussed above. The reason for the negative fields still remains an open question. It could be physical, but it could be of numerical nature as well: The growth of the variation of  $\mathcal{E}$  then would lead to the growth of numerical error and, finally, to the wrong  $\mathcal{E}$ . Indeed, by refining the grid, the electric field changes sign somewhat later, but the sign change can not be completely avoided. Even in the 1D rescaled case (called  $v_3$  previously), the electric field still changes sign (only that in 1D this does not impose a numerical problem). To keep the sign of the electric field fixed everywhere during the evolution constrains the physical situations that can be analyzed. But within this constraint, valuable physical solutions can be obtained.

It seems worth mentioning at this point that we have tested two versions of the commercial software package FEMLAB, but that the performance is much worse than that of our own program.

### 8.3.3 Analysis of numerical results and comparison with stability analysis

In spite of these numerical constraints, the obtained results can be analyzed: An increase of the total applied voltage  $u_t$  leads to

- a decrease of the wave number  $k$  of the leading mode,
- an increase of  $\text{Im}(\lambda)$   $\rightarrow$  a decrease of the oscillation period,
- an increase of  $\text{Re}(\lambda)$   $\rightarrow$  an increased growth rate of the oscillation amplitude.

These conclusions are drawn from the stability analysis and confirmed by the simulations.

In all these simulations, the initial condition is taken as

$$\rho(x, z, 0) = \rho_0(z) + C \rho_1(z) e^{ikx}, \quad (8.47)$$

where  $k$  is the wavenumber of the leading mode,  $\rho_0(z)$  is the stationary solution,  $\rho_1(z)$  is the eigenfunction of the linearized problem treated in Section 8.1, and the parameter  $C$  is chosen such that the perturbation  $C\rho_1$  is only about 1% of initial ion density  $\rho_0$ . The transversal modulation of the initial condition grows, when  $\text{Re}(\lambda)$  is positive with maximum for some  $k \neq 0$ , and spatial structures emerge. An example for  $u_t = 40$  is shown in Fig. 8.12a).



As can be seen in Fig. 8.8, the initial state of the simulation is not precisely the stationary state as oscillations with finite amplitude can be noted from the beginning. We have encountered similar effects of a non-ideal initial condition in Chapter 6. As the homogeneous  $k = 0$  mode is excited initially, it continues to grow. As long as the perturbations are within a linearizable regime, the spatially structured mode with  $k \neq 0$  grows independently with its own speed. The growth rates of the homogeneously oscillating state and the spatially periodic structure are investigated in the Fig. 8.9.

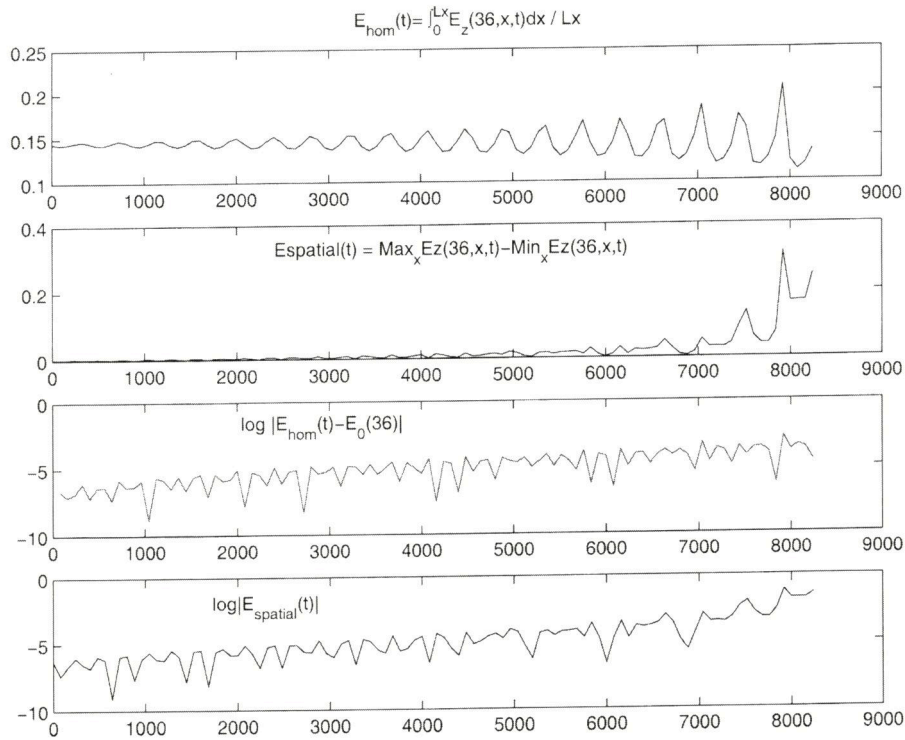


Figure 8.9: Analysis of the growth rates of homogeneous and pattern forming modes as described in the text for  $\mathcal{R}_s = 2 \cdot 10^6$  and  $u_t = 46.4$ . Time  $t$  is on the horizontal axis.

The analysis is done for  $U_t = 46.4$ . For this value, the stability analysis gives the leading mode for  $k = 0.0267$  and complex eigenvalue  $\lambda(k) = 4.615 \cdot 10^{-4} + 0.0119 i$ . Accordingly, the period of temporal oscillations is  $2\pi/\text{Im}(\lambda) = 527.55$ . The oscillation period in the computations is practically the same (approximately around 500). According to the stability analysis, the spatially structured oscillating mode grows at a quicker rate than the homogeneously oscillating mode ( $\text{Re}[\lambda(k)] > \text{Re}[\lambda(0)]$ ), which has to be tested on the

full pde simulation. Therefore two functions of the field  $\mathcal{E}_z(x, L, t)$  on the gas semiconductor interface are studied: the transversally averaged field

$$\mathcal{E}_{hom}(t) = \int_0^{L_x} \frac{dx}{L_x} \mathcal{E}_z(L, x, t), \quad (8.48)$$

and the spatial modulation of the field

$$\mathcal{E}_{spatial}(t) = (\max_x \mathcal{E}_z(L, x, t) - \min_x \mathcal{E}_z(L, x, t)). \quad (8.49)$$

Plots of these functions can be seen in the upper two panels of Fig. 8.9. In the lower two panels of the figure, the evolution of  $\log |\mathcal{E}_{hom}(t) - \mathcal{E}_0(L)|$  and  $\log |\mathcal{E}_{spatial}(t)|$  is plotted. The line through the maxima of the logarithms is approximately a straight line, which means that the growth is exponential. The slope of the line through  $\log |\mathcal{E}_{spatial}(t)|$  is slightly steeper which implies that dominant mode has non-vanishing wave length. Therefore  $\text{Re}[\lambda(k)] > \text{Re}[\lambda(0)]$  is confirmed. Of course, this is only a first indication that numerical results behave as stability analysis predicts.

### 8.3.4 Spatio-temporal patterns

Further investigation of the results in Fig. 8.8 shows that for some lower values of the applied voltage, temporal oscillations seemed to reach a limit cycle, and fully developed spatio-temporal structures can be observed. A closer look into the spatial structure for one of those parameters ( $u_t = 40$ ) is represented in Fig. 8.10.

The result of the stability analysis is that at  $k = 0.03$  there is a maximum value of the real part of the eigenvalue. Consequently, the characteristic length scale is  $2\pi/k \approx 200$  and indeed one can see that there are three peaks equally distributed over the length 600. Actually, initially we started with the small perturbation of that wave length. But the perturbation is not smeared out. On the contrary, the amplitude is growing (Fig. 8.11). In Fig. 8.10a) only one instant of time ( $t=19840$ ) is shown, though that mode is selected from the beginning and preserved until the time of approximately 20000. Let us first focus on the regular structure of these three localized peaks.

Fig. 8.11 shows the evolution of temporal oscillations with the small spatial perturbation. Both temporal oscillations and the amplitude of the spatial modulation are growing as can be seen in the first part of that figure (Fig. 8.11a) which shows evolution until the time 6000. The second part of the figure shows evolution from time 7600 up to 12000. There, one can notice that temporal oscillations are still growing but at a slower rate, while on top of them there is a periodic spatial modulation, which seems to persist with the same amplitude during these few periods. The spatial amplitudes of ion densities always remain the same and profiles behave as a standing wave. There are three maxima and at some other instant of time, there are three minima at the same points of space. To see that more clearly, it is instructive to plot the evolution of the ion density within a larger time interval. That has been done in Fig. 8.12a) for the

time interval 14000-26000, which is a continuation of the previously shown time evolution in Fig. 8.11. Fig. 8.12a) shows that there is indeed analogy with the standing wave with the only difference that the amplitudes corresponding to minima and maxima of ion density concentrations are increasing with the time. Furthermore, one can notice that disturbance of this regular structure starts to appear around time 2000. Then non-linear effects lead to the selection of two times bigger  $k$ -mode (see e.g. Fig. 8.10b). Different view point of Fig. 8.12a), given in Fig. 8.12b) shows clearly that behavior, as well.

From what has been said above, one can conclude that there are temporal oscillations with small spatial distribution. But for the ion density at some later stage this is not correct anymore, since then the homogeneous mode stops being dominant. Fig. 8.12b) shows that the temporal oscillations of  $\rho$  approach a limit cycle while the amplitude of spatial modulation grows until it becomes of the same order of magnitude as the amplitude of temporal oscillations. At this point the wave length of the spatial mode tends to double. Unfortunately, due to the above mentioned limitation of the numerical code, the further evolution of the spatio-temporal structure is not studied.

Nevertheless, the program was successful for a sufficiently long time to observe the formation of some spatial structures. This pattern Fig. 8.12a) is periodic in both time and space. The amplitude of spatial oscillation seems to grow, while temporal oscillations reached a limit cycle according to Fig. 8.8.

To summarize, what we have observed in this (Figs. 8.10-8.12) and a number of other simulations is that the wave number of the dominant mode is very small  $k_{max} \ll 1$ , so that the growth rate of this mode is similar to the growth rate of the homogeneous mode  $k = 0$ . That implies that the  $k = 0$  mode can easily be excited, as well. Due to the imperfect initial condition, that is exactly what happens. On top of the homogeneous oscillations there is a spatial modulation and with the time the amplitude of the spatial structure becomes comparable with the amplitude of the temporal oscillations. As an initial condition we use a stationary state obtained as a solution of ODE's and then we import this data file into the program solving full PDE's. Doing that we are bound to insert a numerical noise sufficient to excite the homogeneous mode. Initially, for the small amplitudes, results are in agreement with the stability analysis predictions, while for larger amplitudes, results are showing new and interesting features.

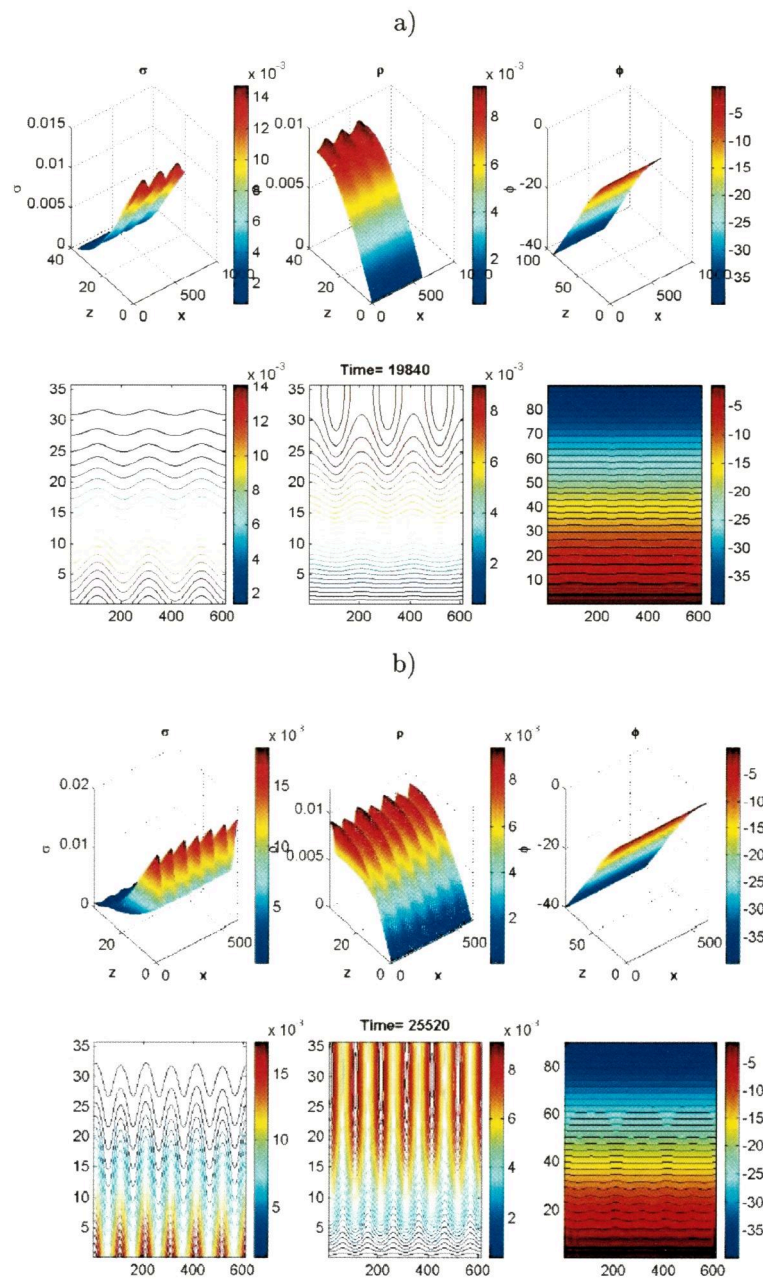


Figure 8.10: Profiles of the electron and ion densities in the discharge region and the potential in the whole system at two instants of time for the previously investigated parameters  $\mathcal{R}_s = 2 \cdot 10^6$  and  $u_t = 40$ . Shown are 3D plots above with the corresponding contour lines in the  $xz$  plane below. The transversal dimension is  $L_x = 600$ .

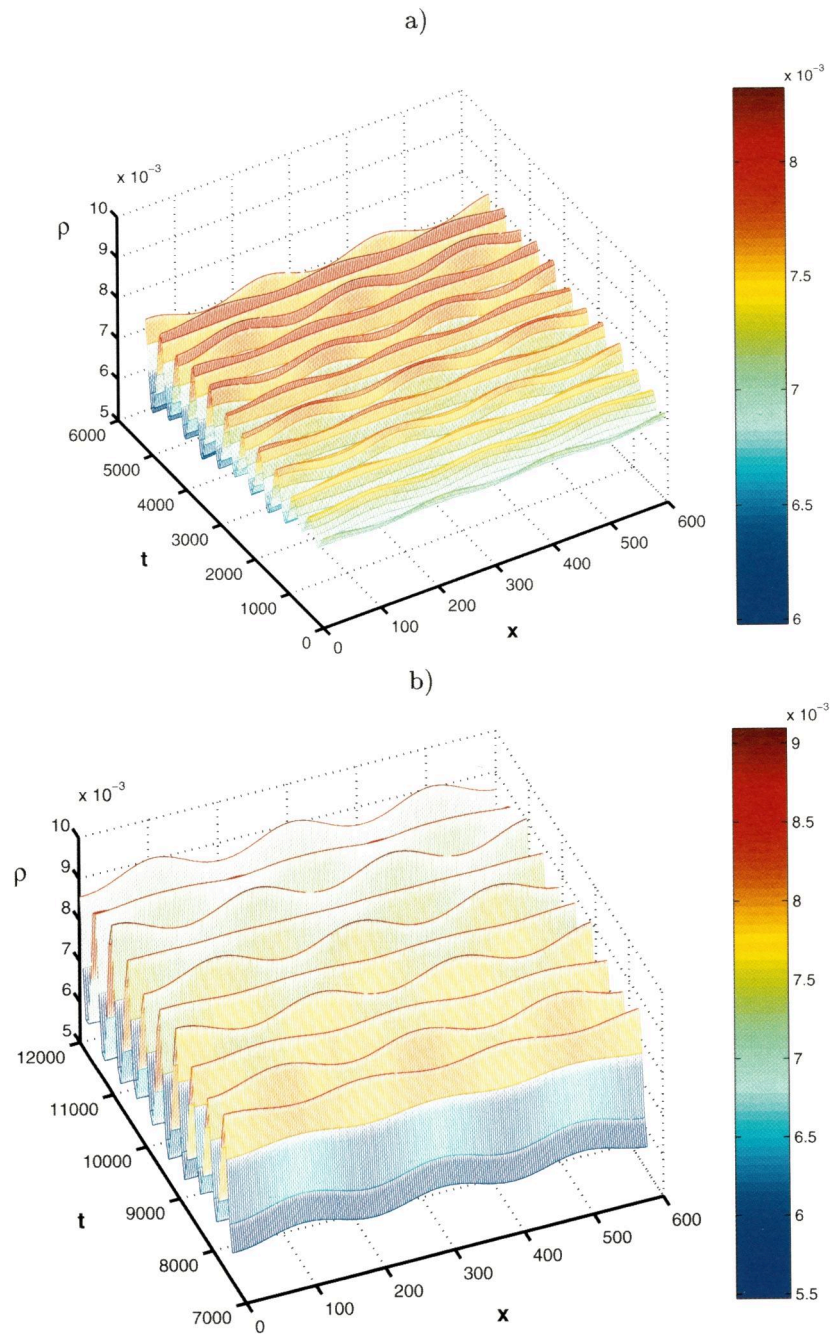


Figure 8.11: 3D visualization of the evolution of ion density. a) From the beginning, with the initial spatial modulation of the same wave length as the leading mode. b) Few periods of time at some later stage.

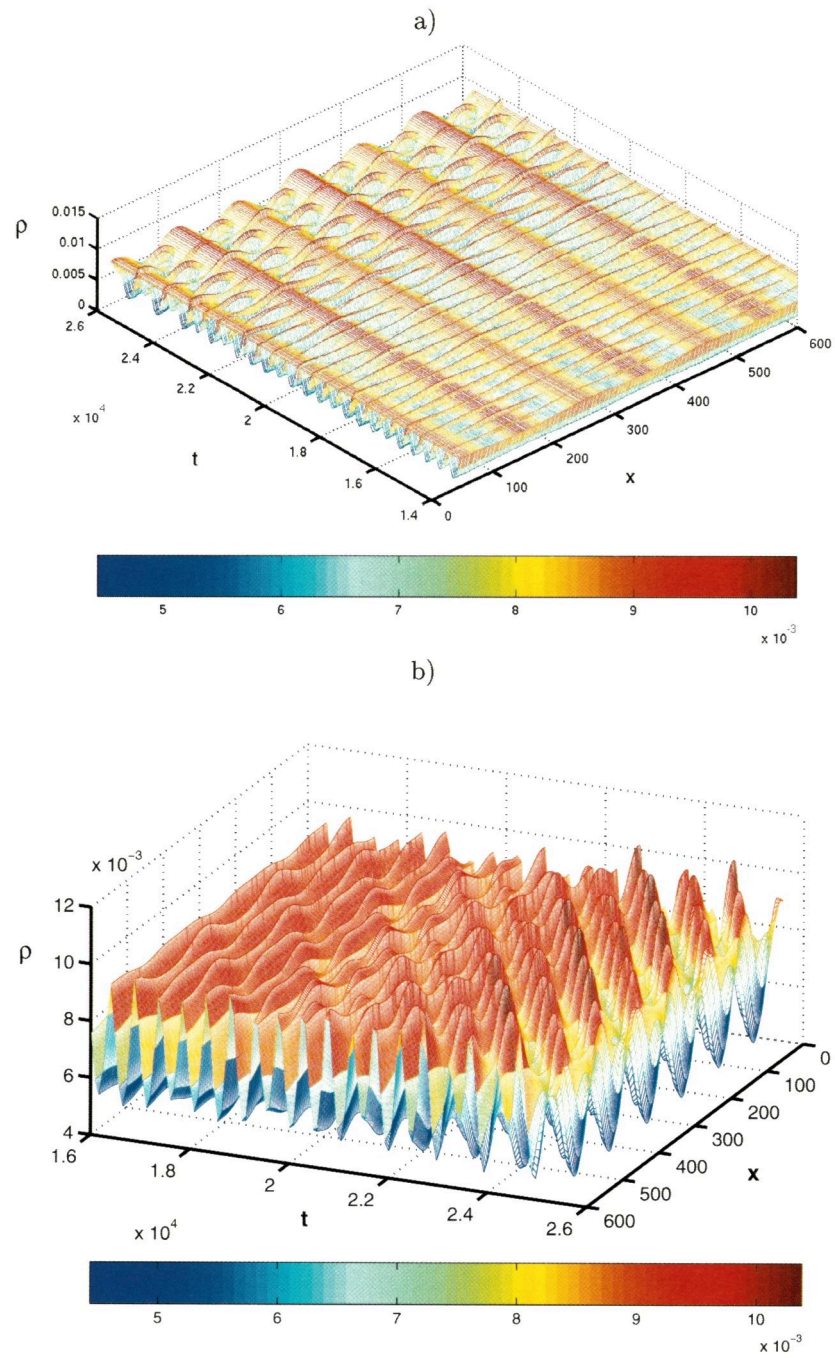


Figure 8.12: Two different plots of the same evolution of the ion density in two slightly different time intervals. a) Formation of the spatio-temporal pattern. b) Increase of the spatial amplitude of ion density distribution.

### 8.3.5 Outlook

The numerical example of spatio-temporal structure discussed in Figs. 8.10-8.12 can be related to experimentally observed blinking filaments (see Chapter 3, Fig. 3.3). The spatio-temporal dynamics of these filaments is rather complicated and not very well studied. The characteristic wave length of these filaments [70] is found to be much smaller than the wave length of our numerically observed structure. However, in Fig. 5.2(a) and (b) of the thesis [12], a spatio-temporal structure called ‘band structure’ has been observed as some transient structure towards smaller blinking filaments. The wave length of this ‘band structure’ turns out to be of the same order of magnitude ( $\approx 300$ ) as our numerically observed structure ( $\approx 200$ ). This agreement shows once again, that our simple model captures all relevant physics and is able to explain (qualitatively and to some extent even quantitatively) complicated spatio-temporal dynamics of experimentally observed structures.

Furthermore, it should be noted that the parameters used in these simulations were not suited for the investigation of stationary spatial patterns. Actually, stationary stripe patterns [57] were found experimentally in the completely different parameter range than the one investigated here. Anyhow, logical continuation of the research done in this thesis, includes investigation of these parameters in two dimensions, as well; and indeed, spatio-temporal structure corresponding to experimental ‘band’ structure i.e., blinking filaments has been found and discussed.

The main point is that within our parameters we have competition between purely Hopf and Hopf-Turing bifurcation. The best would be to have purely Turing bifurcation from the base homogeneous stationary state and then the stationary spatial structure could be expected. A way how to find Turing bifurcation might be in more extensive investigation of the previous parameters space (Subsection 8.1.4), so as to find a combination such that the branch of the purely real eigenvalues would first become unstable.

Another way is to follow experimental observations. An experimental indication where to search for stationary stripe pattern is:  $L = 86 - 90$ ,  $L_s = 108$ ,  $\mathcal{R}_s = 10^7 - 10^9$ ,  $C_s = 0.1$ ,  $\epsilon_s = 11 - 12$  and for the applied voltage approximately around  $u_t = 65$ . Stationary hexagon structures should be searched for in the similar range of parameters. For the simulation, these parameters are computationally more expensive. Anyhow, the next step is certainly to explore the wide range around these parameters and to obtain the bifurcation diagram. Furthermore, to really see hexagons or stripes numerically, the third spatial dimension has to be included as well.

# Bibliography

- [1] B. Bruhn, B.-P. Koch, and P. Jonas. *Phys. Rev. E* **58**, 3793–3805 (1998).
- [2] B. Bruhn and B.-P. Koch. *Phys. Rev. E* **3078-3092**, 2000 (61).
- [3] Yu.B. Golubovski, V.A. Maiorov, V.O. Nekutchayev, J. Behnke, and J.F. Behnke. *Phys. Rev. E* **63**, 036409 (2001).
- [4] W. Breazeal, K.M. Flynn, and E.G. Gwinn. *Phys. Rev. E* **52**, 1503 (1995).
- [5] R.Sh. Islamov. *Phys. Rev. E* **64**, 046405 (2001).
- [6] L. Dong *et al.* *Thin Solid Films* **435**, 120 (2003).
- [7] S. Nasuno. *Chaos* **13**, 1010 (2003).
- [8] Yu.A. Astrov, E. Ammelt, and H.-G. Purwins. *Phys. Rev. Lett.* **78**, 3129 (1997).
- [9] Yu.A. Astrov and Y.A. Logvin. *Phys. Rev. Lett.* **79**, 2983–2986 (1997).
- [10] E. Ammelt, Yu.A. Astrov, and H.-G. Purwins. *Phys. Rev. E* **55**, 6731 (1997).
- [11] C. Strümpel, Y.A. Astrov, and H.-G. Purwins. *Phys. Rev. E* **62**, 4889–4897 (2000).
- [12] C. Strümpel. PhD thesis, Univ. Münster, (2001). in German.
- [13] A. von Engel and M. Steenbeck. *Elektrische Gasentladungen*, volume II. Springer, Berlin, (1934).
- [14] H.-G. Purwins, C. Radehaus, T. Dirksmeyer, R. Dohmen, R. Schmeling, and H. Willebrand. *Phys. Lett. A* **136**, 480 (1989).
- [15] C. Radehaus, R. Dohmen, H. Willebrand, and F.-J. Niedernostheide. *Phys. Rev. A* **42**, 7426 (1990).
- [16] Z.Lj. Petrović and A.V. Phelps. *Phys. Rev. E* **47**, 2806–2814 (1993).
- [17] B.M. Jelenkovic, K. Rózsa, and A.V. Phelps. *Phys. Rev. E* **47**, 2816–2824 (1993).



- [18] A.V. Phelps, Z.Lj. Petrović, and B.M. Jelenković. *Phys. Rev. E* **47**, 2825–2838 (1993.).
- [19] Z.Lj. Petrović, I. Stefanović, S. Vrhovac, and J. Živković. *J. Phys. IV France, Colloque C4* **7**, 341–352 (1997).
- [20] E. Scholl. *Nonequilibrium Phase Transitions in Semiconductors*. Springer-Verlag, Berlin Heidelberg, (1987).
- [21] Z.Lj. Petrović and A.V. Phelps. *Phys. Rev. E* **56**, 5920 (1997).
- [22] V.I. Kolobov and A. Fiala. *Phys. Rev. E* **50**, 3018–3032 (1994.).
- [23] I. Pérès and L.C. Pitchford. *J. Appl. Phys.* **78**, 774 (1995.).
- [24] L.M. Portsel, Y.A. Astrov, I. Reimann, and H.-G. Purwins. *J. Appl. Phys.* **81**, 1077 (1997.).
- [25] R.R. Arslanbekov and V.I. Kolobov. *J. Phys. D* **36**, 2986 (2003).
- [26] K.G. Müller. *Phys. Rev. A* **37**, 4836 (1988).
- [27] H.-G. Purwins, C. Radehaus, T. Dirksmeyer, R. Dohmen, R. Schmeling, and H. Willebrand. *Phys. Lett. A* **136**, 480 (1989.).
- [28] C. Radehaus, R. Dohmen, H. Willebrand, and F.-J. Niedernostheide. *Phys. Rev. A* **45**, 2546 (1992).
- [29] Yu.P. Raizer. *Gas Discharge Physics*. Springer, Berlin, 2nd corrected printing edition, (1997).
- [30] Y.B. Golubovskii, V.A. Maiorov, J. Behnke, and J.F. Behnke. *J. Phys. D - Applied Physics* **35**, 751–761 (2002).
- [31] Henry Greenside and Michael Cross. *Pattern Formation and Dynamics in Nonequilibrium Systems*. preprint of the book; to appear 2004/2005.
- [32] H. Nishimori and N. Ouchi. *Phys. Rev. Lett.* **71**, 197 (1993).
- [33] R. Kapral and K. Showalter, editors. *Chemical Waves and Patterns*. Kluwer Academic Publishers, Dordrecht, (1995).
- [34] D. Walgraef. *Spatio-Temporal Pattern Formation*. Springer, New York, (1997).
- [35] F.H. Busse and L. Kramer. *Nonlinear Evolution of Spatio-Temporal Structures in Dissipative Continuous Systems*. Plenum Press, New York, (1990).
- [36] Y.J. Li, J. Oslonovitch, N. Mazouz, F. Plenge, K. Krischer, and G. Ertl. *Science* **291**, 2395 (2001).

- [37] H. Engel, F. Niedernostheide, H. Purwins, and E. Scholl, editors. *Self-organization in activator-inhibitor-systems: semiconductors, gas-discharge and chemical active media*. Wissenschaft und Technik, Berlin, (1996).
- [38] T. Ackemann and W. Lange. *Appl. Phys. B* **72**, 21 (2001).
- [39] A.T. Winfree. *J. Biosci.* **27**, 465 (2002).
- [40] A.V. Holden. *Physics World* **November 1998**, 29 (1998).
- [41] H. Haken. *Brain Dynamics*. Springer, Berlin, (2002).
- [42] J.D. Murray. *Mathematical Biology*. Springer, Berlin, (1989).
- [43] A. Goldbeter. *Biochemical Oscillations and Cellular Rhythms*. Cambridge University Press, Cambridge, (1996).
- [44] P. Ball. *The Self-Made Tapestry: Pattern Formation in Nature*. Oxford University Press, Oxford, (1999).
- [45] J. Lechleiter, S. Girard, E. Perlatá, and D. Clapham. *Science* **252**, 123 (1991).
- [46] B. Blasius, A. Huppert, and L. Stone. *Nature* **399**, 354 (1999).
- [47] S.H. Stogatz. *Nonlinear Dynamics and Chaos*. Addison-Wesley, Reading, Massachusetts, (1994).
- [48] P. Glendinning. *Stability, Instability and Chaos: an introduction to the theory of nonlinear differential equations*. Cambridge University Press, Cambridge, (1994).
- [49] J.J. Tyson, K.A. Alexander, V.S. Manoranjan, and J.D. Murray. *Physica D* **34**, 193 (1989).
- [50] H.G. Schuster. *Deterministic Chaos*. Physik-Verlag, Weinheim, (1984).
- [51] J. Guckenheimer and P.J. Holmes. *Nonlinear Oscillations, Dynamical Systems and Bifurcations of Vector Fields*. Springer, New York, (1983).
- [52] J.H. Poincaré. *Les Methodes Nouvelles de la Mécanique Celeste*. Gauthier-Villars, Paris, (1892-1899).
- [53] D.W. Jordan and P. Smith. *Nonlinear Ordinary Differential Equations*. Oxford University Press, Oxford, (1987).
- [54] Gérard Iooss and Daniel D. Joseph. *Elementary Stability and Bifurcation Theory*. Springer-Verlag, New York, (1980).
- [55] Y.A. Kuznetsov. *Elements of Applied Bifurcation Theory*. Springer, New York, (1995).

- [56] M.C. Cross and P.C. Hohenberg. *Rev. Mod. Phys.* **65**, 851 (1993).
- [57] Yu.A. Astrov, E. Ammelt, S. Teperick, and H.-G. Purwins. *Phys. Lett. A* **211**, 184 (1996.).
- [58] M. van Hecke, P.C. Hohenberg, and W. van Saarloos. Amplitude equations for pattern forming systems. In *Fundamental Problems in Statistical Mechanics VIII*, H. van Beijeren and M.H. Ernst, editors, 245–278. North-Holland, Amsterdam (1994).
- [59] U. Kogelschatz. *Plasma Chem. Pl. P.* **23**, 1–46 (2003).
- [60] Piet Jonas. PhD thesis, Greifswald, <http://www.physik.uni-greifswald.de/~jonas/Thesis/index.html>, (1998). in German.
- [61] T. Braun *et al.* *Phys. Rev. Lett.* **59**(6), 613 (1987.).
- [62] J. Qin, L. Wang, D.P. Yuan, P. Gao, and B.Z. Zhang. *Phys. Rev. Lett.* **63**(2), 163 (1989.).
- [63] P.Y. Cheung, S. Donovan, and A.Y. Wong. *Phys. Rev. Lett.* **61**(12), 1360 (1988).
- [64] V.O. Papanyan and Yu.I. Grigoryan. *Physics Letters A* **164**, 43–48 (1992).
- [65] Ranjit Singh, P.S.R. Prasad, J.K. Bhattacharjee, and R.K. Thareja. *Physics Letters A* **178**, 284–288 (1993).
- [66] P.R. Sasi Kumar, V.P.N. Nampoori, and C.P.G. Vallabhan. *Physics Letters A* **196**, 191–194 (1994).
- [67] Y.A. Astrov, I. Müller, E. Ammelt, and H.-G. Purwins. *Phys. Rev. Lett.* **80**, 5341 (1998.).
- [68] E. Ammelt, Yu.A. Astrov, and H.-G. Purwins. *Phys. Rev. E* **58**, 7109 (1998.).
- [69] C. Strümpel, Y.A. Astrov, E. Ammelt, and H.-G. Purwins. *Phys. Rev. E* **61**, 4899 (2000.).
- [70] C. Strümpel, H.-G. Purwins, and Y.A. Astrov. *Phys. Rev. E* **63**, 026409 (2001.).
- [71] Y.A. Astrov and H.-G. Purwins. *Phys. Lett. A* **283**, 349 (2001.).
- [72] C. Strümpel, H.-G. Purwins, and Y.A. Astrov. *Phys. Rev. E* **65**, 066210 (2002.).
- [73] E.L. Gurevich, A.S. Moskalenko, A.L. Zanin, Y.A. Astrov, and H.-G. Purwins. *Phys. Lett. A* **307**, 299 (2003.).

- [74] Aliaksei L. Zanin. *Experimental investigation on pattern formation in planar barrier gas discharge*. PhD thesis, Univ. Münster, (2003).
- [75] M.J. Druyvesteyn and F.M. Penning. *Rev. Mod. Phys.* **12**, 87–174 (1940).
- [76] R.W. Crowe, J.K. Bragg, and V.G. Thomas. *Phys. Rev.* **96**, 10–14 (1954.).
- [77] A.L. Ward and E. Jones. *Phys. Rev.* **122**, 376–380 (1961.).
- [78] A.L. Ward. *J. Appl. Phys.* **33**, 2789–2794 (1962.).
- [79] J.M. Meek and J.D. Craggs. *Electrical Breakdown of Gases*. John Wiley and Sons, (1978).
- [80] B.N. Klyarfeld, L.G. Guseva, and A.S. Pokrovskaya-Soboleva. *Sov. Phys. Tech. Phys.* **11**, 520 (1966.).
- [81] A.S. Pokrovskaya-Soboleva and B.N. Klyarfeld. *Sov. Phys. JETP* **5**, 812–818 (1957.).
- [82] G.W. McClure. *Phys. Rev.* **124**, 969–982 (1961.).
- [83] J.-P. Boeuf. *J. Appl. Phys.* **63**, 1342–1349 (1988.).
- [84] A. Fiala, L.C. Pitchford, and J.-P. Boeuf. *Phys. Rev. E* **49**, 5607–5622 (1994.).
- [85] D.D. Šijačić and U. Ebert. *Phys. Rev. E* **66**, 066410 (2002.).
- [86] We thank dr. Manuel Arrayás for this suggestion.
- [87] Han.S. Uhm, Eun.H. Choi, and Guang.S. Cho. *Appl. Phys. Lett.* **78**, 592 (2001.).
- [88] G. Auday, Ph. Guillot, J. Galy, and H. Brunet. *J. Appl. Phys.* **83**, 5917–5921 (1998.).
- [89] Yu.P. Raizer, U. Ebert, and D.D. Šijačić. *Phys. Rev. E* **70**, 017401 (2004).
- [90] M. Surendra, D.B. Graves, and L.S. Plano. *J. Appl. Phys.* **71**, 5189 (1992).
- [91] D.D. Šijačić, U. Ebert, and I. Rafatov. *Phys. Rev. E* **70**, to appear (2004).
- [92] E.L. Gurevich, A.W. Liehr, Sh. Amiranashvili, and H.-G. Purwins. *Phys. Rev. E* **69**, 036211 (2004).
- [93] S. Godunov. *Uspehi Mat. Nauk.* **16**, 243–255 (1961).
- [94] S.D. Conte. *SIAM Review* **8**(3), 309–321 (1966).
- [95] private communication with dr. Alexander Morozov, Instituut Lorentz , Leiden University.

- 
- [96] W. Hundsdorfer and J.G. Verwer. *Numerical solution of time-dependent advection-diffusion-reaction equations*. Springer Series in Computational mathematics 33, Springer-Verlag, Berlin, (2003).
- [97] P. Wesseling. *Principles of computational fluid dynamics*. Springer Series in Computational mathematics 29, Springer-Verlag, Berlin, (2001).
- [98] J.W. Thomas. *Numerical Partial Differential Equations: Conservation Laws and Elliptic Equations*, 343. Texts in Applied Mathematics 33, Springer-Verlag (1999).
- [99] D.D. Šijačić, U. Ebert, and I. Rafatov. *submitted to Phys. Rev. E* .

# Summary

## **Experimental observations and theoretical problem setting:**

A layered planar structure of a short gas discharge gap and a high ohmic semiconductor cathode exposed to a DC voltage can spontaneously generate a wealth of spatio-temporal patterns. Such a system with a wide lateral aspect ratio has been investigated extensively in the past years in the group of prof. H.-G. Purwins at the University Münster, Germany, in collaboration with scientists from St. Petersburg and Moscow. Next to detailed experimental studies, their theoretical investigations concentrated mainly on phenomenological models of reaction-diffusion type for the two transversal directions of the system. Such models are not derived systematically from the underlying gas discharge physics, but are inspired from the investigation of similar structures in chemical, biological, and semiconductor systems. With appropriately adjusted parameters, they qualitatively describe the observed patterns. In contrast, the subject of this thesis is to understand these patterns starting from the underlying gas discharge physics, and to examine to what extent phenomenological reaction diffusion models are applicable. The thesis contains numerical and analytical results on the stationary, homogeneously oscillating, and pattern forming solutions of the system and comparison with the experiment.

## **Model:**

The gas discharge system operates at the transition from Townsend to glow discharge. We describe it by the classical minimal continuum approximation that takes drift and space charge effects of electrons and positive ions into account, as well as impact ionization in the gap and secondary emission from the cathode. The semiconductor layer is treated in linear approximation. All details of the model are given in Chapter 4.

## **Stationary solutions:**

Parameter reduction by dimensional analysis allows studies of the full parameter space of 1D stationary solutions on the transition from Townsend discharge to the space charge dominated glow discharge regime. In Chapter 5, we present the full numerical results as well as a systematic small current expansion about the Townsend limit up to third order in the current, thereby revising previous

results. For large  $pd$  (pressure of the gas times distance between the electrodes), the current-voltage characteristics shows a textbook subcritical behavior. For smaller  $pd$ , it does not immediately reach a supercritical characteristics, but for any value of the secondary emission coefficient  $\gamma$  first exhibits an unexpected 'mixed' behavior. Furthermore, we state that the transition from Townsend to glow discharge strongly depends on  $\gamma$ , and we show that the earlier result of Von Engel and Raizer on the small current expansion about the Townsend limit actually is the limit of small  $\gamma$  of our new systematic expression. The chapter is based on the publications [85, 89].

#### **Oscillatory solutions:**

The gas-discharge-semiconductor system exposed to a stationary voltage can spontaneously attain a mode of temporal oscillations while staying spatially homogeneous. In Chapter 6, this behavior is reproduced by our numerical solutions, including the coexistence of stationary and oscillating solutions in certain parameter regimes. Furthermore, we have investigated the linear stability of the stationary state. The obtained results of the analysis are in agreement with the numerical solutions of the full model. Therefore, they have been used to determine bifurcation diagrams for the transition from stationary to oscillating solutions. Despite the minimal model and uncertainty about the precise internal parameters, the results qualitatively (and to some extent even quantitatively) reproduce experiments. This chapter is based on the paper [99].

#### **Period doubling cascade and relation to reaction-diffusion models:**

Investigating the parameter space of temporal oscillations numerically, we found a cascade of period doubling events. This shows that the inner structure of the discharge is more complex than can be described by a two-component reaction-diffusion model with negative differential conductivity: The main point is that a system with global negative differential conductivity due to space charge effects in the gas gap cannot be treated as a system with local negative differential conductivity. We also derived an alternative reduced model. Furthermore, we have found an example where oscillations coexist with global positive differential conductivity of the current-voltage characteristics (Chapter 7) while any reaction-diffusion model would require negative differential conductivity. These results on spatially homogeneous and temporally oscillating solutions apply to any gas discharge operated in sequence with a resistor with capacitance. The results of this chapter appear in [91], except for the one on oscillations coexisting with global positive differential conductivity that will be submitted elsewhere.

#### **Spatio-temporal patterns:**

The system is investigated in two spatial dimensions i.e, one transversal spatial dimension is added next to the previously investigated longitudinal direction. Therefore, the stability analysis of the stationary state is extended to Fourier

---

modes with a transversal wave vector  $k$ . The resulting dispersion curve determines whether a spatially homogeneous or a spatially structured pattern can be expected to emerge from a perturbation of the homogeneous stationary state. Staying within the same parameter regime as in all previous chapters, it is found that either purely Hopf bifurcation or Turing-Hopf bifurcation takes place. One example of Turing-Hopf bifurcation has been investigated in more detail. In parallel, the two-dimensional dynamical gas-discharge-semiconductor system is solved numerically using a finite difference technique. Some preliminary results are presented and within their linear growth phase, they are in agreement with stability analysis results. Further development of the spatio-temporal structure exhibits new dynamical features. Our numerical results can be related to the experimentally observed blinking filaments regime. Furthermore, it is found that the wave length of the spatial structure directly corresponds to the wave length of the experimental ‘band’ structure [12]. The paper based on this last chapter is in preparation.





# Samenvatting

## **Experimentele waarnemingen en formulering van het theoretische probleem**

Ons systeem bestaat uit twee smalle parallele lagen; een laag waarin de gasontlading plaatsvindt en een halfgeleider met een grote weerstand. Wanneer men over deze structuur een gelijkspanning aanlegt, kan een gasontlading plaatsvinden en een grote variëteit aan patronen spontaan optreden. Een dergelijk systeem, dat veel breder is dan hoog, is de afgelopen jaren intensief bestudeerd in de groep van prof. H.-G. Purwins in de Universiteit van Münster, Duitsland in samenwerking met wetenschappers uit St. Petersburg en Moskou. Naast gedetailleerde experimenten richtte hun theoretische onderzoek zich vooral op fenomenologische reactie-diffusie modellen voor de beide transversale richtingen van het systeem. Dergelijke modellen zijn niet systematisch afgeleid uit de onderliggende gasontladingsfysica, maar worden veel meer geïnspireerd door het onderzoek aan gelijksoortige structuren in biologische, chemische en halfgeleider systemen. Deze methodes beschrijven de geobserveerde patronen kwalitatief, als men de parameters juist kiest. Het onderwerp van dit proefschrift is daarentegen, de patronen te begrijpen startend vanuit de onderliggende gasontladingsfysica. Ook willen wij onderzoeken in hoeverre fenomenologische reactie-diffusie modellen toepasbaar zijn. Het proefschrift bevat numerieke en analytische resultaten over de oplossingen van het systeem. Deze kunnen naast stationaire en homogeen oscillerende patronen ook patronen vormen die in ruimte en tijd oscilleren. Daarnaast zullen we de resultaten vergelijken met de experimenten.

## **Het model**

We bekijken een gasontladingssysteem dat zich bevindt in de overgang van de Townsend ontlading naar de glimontlading. We beschrijven het met een klassieke minimale continuum benadering, waarin rekening gehouden wordt met drift en ruimteladingseffecten van de elektronen en positieve ionen. Ook nemen wij botsingsionisatie en secundaire emissie van elektronen van de kathode in het model mee. Alle details van het model worden gegeven in hoofdstuk 4.

### Stationaire oplossingen

Reductie van de parameters door dimensionele analyse maakt het mogelijk het volledige parameter regime van 1-dimensionale oplossingen van de overgang van de Townsend ontlading naar het door de ruimtelading gedomineerde glimontlading regime te bestuderen. In hoofdstuk 5 presenteren we zowel de volledige numerieke resultaten als een systematische expansie in kleine stroom rond de Townsend limiet tot derde orde in de stroom. Hierin herzien en commentarieren we oude resultaten. Als de parameter  $pd$  groot is, heeft de stroomspanningskarakteristiek het subkritische gedrag dat bekend is uit de leerboeken. Voor kleinere waarden van  $pd$  bereikt het niet onmiddellijk superkritisch gedrag, maar vertoont voor elke waarde van de secundaire emissie coefficient  $\gamma$  eerst een onverwacht gemengd gedrag. Verder tonen wij aan dat de overgang van Townsend- naar glimontlading sterk afhangt van  $\gamma$ , en dat het eerdere resultaat van Von Engel en Raizer van de expansie voor kleine stroom rond de Townsend limiet eigenlijk de limiet is van onze systematische expansie voor kleine  $\gamma$ . Het hoofdstuk is gebaseerd op de artikelen [85, 89].

### Oscillerende oplossingen

Het systeem dat bestaat uit een gasontlading die gekoppeld is aan een halfgeleider kan spontaan een toestand met oscillaties in de tijd aannemen, wanneer het wordt blootgesteld aan een stationaire spanning, terwijl het homogeen in de ruimte blijft. In hoofdstuk 6 wordt dit gedrag gereproduceerd door onze numerieke oplossingen. Ook zien wij bepaalde regimes van de parameters waar beide toestanden (stationair en oscillerend) tegelijk optreden. Wij hebben ook een lineaire stabiliteitsanalyse van de stationaire toestand uitgevoerd. De resultaten hiervan tonen overeenstemming met de numerieke simulaties van het volledige model. Daarom kunnen deze resultaten gebruikt worden om het bifurcatiediagram van de overgang van stationaire naar oscillerende oplossingen te bepalen. Ondanks het gebruik van een minimaal model en onzekerheid over de interne parameters reproduceren de resultaten de experimenten kwalitatief en tot op zekere hoogte kwantitatief. Dit hoofdstuk is gebaseerd op artikel [99].

### Een cascade van verdubbelingen van de periodes en de relatie met reactie-diffusie modellen

Na het numeriek onderzoek van de parameterruimte van tijdelijke oscillaties vonden we een cascade van verdubbelingen van de periodes. Dit toont aan dat de structuur binnenin de ontlading complexer is dan een systeem dat beschreven kan worden door een reactie-diffusie model met twee componenten met negatieve differentiele geleiding. Het belangrijkste punt is dat een systeem waarin een globale negatieve differentiele geleiding ontstaat door effecten van de ruimtelading, niet behandeld kan worden als een systeem met locale negatieve differentiele geleiding. We hebben ook een alternatief gereduceerd model afgeleid. Verder hebben we ook een numeriek voorbeeld gevonden van de oscillaties wanneer de stroom-spanningskarakteristiek een positieve differentiele geleiding heeft

(hoofdstuk 7). Aangezien elk reactie-diffusie systeem voor een stabiele oscillatie negatieve differentiele geleiding vereist, kan het ons systeem niet beschrijven. Deze resultaten over oplossingen, die homogeen zijn in de ruimte en oscillaties vertonen in de tijd, beperken zich niet tot ons systeem, maar zijn eveneens toepasbaar op elk gasontladingssysteem dat in serie werkt met een weerstand en een condensator, die parallel aan elkaar geschakeld zijn. De resultaten zijn grotendeels te vinden in [91], een artikel over oscillaties in het geval van positieve differentiele geleiding is in voorbereiding.

### **Patronen variërend in ruimte en tijd**

Om ruimtelijke patronen te begrijpen, doen we de stabiliteitsanalyse van de stationaire toestand met Fourier modes met transversale golfvector  $k$ . De dispersiecurve die we hieruit verkrijgen, bepaalt of een patroon met ruimtelijke structuur kan ontstaan door een verstoring van de homogene stationaire toestand. We blijven in hetzelfde parameterregime als in alle voorgaande hoofdstukken en vinden dat ofwel pure Hopf-bifurcaties ofwel Turing-Hopf bifurcaties plaatsvinden. Een voorbeeld van een Turing-Hopf bifurcatie is tot in meer detail bestudeerd. Parallel hieraan is het tweedimensionale dynamische gasontladingshalfgeleider systeem numeriek opgelost met behulp van een eindige-differentie methode. Enkele voorlopige resultaten worden getoond en zijn in overeenstemming met de analytische resultaten van de lineaire stabiliteitsanalyse binnen het gebied waar deze geldig is, de fase van lineaire groei. Verdere ontwikkeling van de structuren, die ruimte- en tijdafhankelijk zijn, toont nieuwe dynamische eigenschappen. Onze numerieke resultaten kunnen gerelateerd worden aan het experimenteel geobserveerde regime met flikkerende filamenten. Verder vonden wij dat de golflengte van de ruimtelijke structuur correspondeert met de golflengte van de experimentele bandstructuur [12]. Het artikel gebaseerd op het laatste hoofdstuk is in voorbereiding.



# Rezime

## **Eksperimentalna postavka i teoretski model**

Slojevita struktura sačinjena od gasnog sloja i visokoomskog poluprovodnika, tretirana jednosmernim naponom, može generisati raznolika prostorno-vremenski zavisna električna pražnjenja, praćena pojavom svetlosti. Slična struktura, sa dominantnim planarnim karakteristikama, se već duže vreme intenzivno istražuje u grupi prof. H.-G. Purwins-a sa univerziteta Munster u Nemačkoj u saradnji sa naučnicima iz St. Petersburg-a i Moskve. Usporedno sa eksperimentima, njihova teoretska razmatranja se uglavnom fokusiraju na fenomenološkom modelu reakciono-difuzionog tipa po transverzalnim pravcima strukture. U biti, taj model ne proizilazi iz bazne fizike gasnih pražnjenja, već se više oslanja na rezultate dobijene u fenomenološki sličnim i dobro proučenim strukturama, ali hemijskim i biološkim, u kojima se, posle pažljivog uskladjivanja parametara, mogu dobiti kvantitativni rezultati koji odgovaraju eksperimentalnim. U ovoj tezi će se, nasuprot izloženom modelu, krenuti od osnovnih mikroskopskih procesa fizike gasnih pražnjenja ka objašnjenju i kvantitativnom opisu posmatranih fenomena, tokom kojeg će se dobiti rezultati porediti sa rezultatima reakciono-difuzionog modela. Ova teza se sastoji od numeričkih i analitičkih rezultata dobijenih za stacionarno i homogeno-oscilatorno stanje sistema (kao i za stanje sistema koje je periodično i u vremenu i u prostoru), koji su analizirani i upoređeni sa eksperimentalno dobijenim rezultatima.

## **Model**

Gasni deo sistema će se posmatrati u režimu prelaza sa Townsend pražnjenja ka pražnjenju praćenom svetlošću. Opisan je minimalnim modelom sa kontinualnom (fluidnom) aproksimacijom. U model su uključeni efekti površinskog i prostornog naelektrisanja, koje potiče od elektrona i pozitivnih jona, kao i efekti udarne jonizacije u gasnom prostoru ( $\alpha$  proces) i sekundarne emisije elektrona sa katode ( $\gamma$  proces). Poluprovodnički deo sistema se opisuje linearnom aproksimacijom. Više o samom modelu se može naći u Poglavlju 4.

## **Stacionarna rešenja**

Redukcija parametara u dimenzionalnoj analizi omogućava proučavanje celog parametarskog faznog prostora u jedno-dimenzionalnom stacionarnom rešenju,

koje je u prelazu sa Townsend pražnjenja ka dominantno svetlosnom pražnjenju. U Poglavlju 5 prikazani su potpuni numerički rezultati kao i sistematski razvoj slabe struje u okolini Townsend limita, trećeg reda, koji su doveli do revizije prethodnih rezultata. Jedni od parametara faznog prostora su pritisak pod kojim se gas nalazi u kapsuli (predstavljen sa  $p$ ) i udaljenost elektroda na krajevima kapsule (predstavljen sa  $d$ ). Za dovoljno veliki proizvod  $pd$ , strujno-naponska karakteristika pokazuje karakteristično subkritično ponašanje, dok se za dovoljno mali proizvod  $pd$  ne dostiže odmah superkritično ponašanje, već se za bilo koju vrednost koeficijenta sekundarne emisije  $\gamma$  prvo ulazi u neočekivano 'miksovano' ponašanje. Dalje se pokazuje da prelaz sa Townsend pražnjenja ka svetlosnom pražnjenju snažno zavisi od  $\gamma$ , i da prethodni rezultati, dobijeni od strane Von Engel-a i Raizer-a o razvoju male struje u okolini Townsend limita, u stvari predstavljaju limit od malog  $\gamma$  u našem novom sistematskom prikazu. Rezultati Poglavlja 5 su objavljeni u radovima [85, 89].

### Oscilatorna rešenja

Gasno-poluprovodnički sistem pod konstantnim naponom može spontano dobiti vremenski oscilatorna pražnjenja praćena luminiscencijom koja su prostorno homogena. U Poglavlju 6 se takvo ponašanje reprodukuje u numeričkom rešenju i proširuje sa dodatnim stanjem u kojem koegzistiraju stacionarno i oscilatorno rešenje u odgovarajućem režimu parametara. Prikazana je takodje i analiza linearne stabilnosti stacionarnog stanja. Dobijeni rezultati su u potpunoj saglasnosti sa numeričkim rezultatima i stoga se mogu koristiti za određivanje faznog dijagrama prelaza iz stacionarnog ka oscilatornom režimu. Uprkos minimalnom modelu i neodređenosti koja je uneta usled prirode internih parametara, dobijeni rezultati kvalitativno i do neke mere čak i kvantitativno odlikavaju eksperimentalno dobijene podatke. Poglavlje 6 se bazira na publikaciji [99].

### Odnos bifurkacije sa udvostručenjem perioda i reakciono-difuzionog modela

Numeričko istraživanje parametarskog prostora vremenski zavisnih oscilacija je otkrilo pojavu umnožavanja perioda oscilacija. Uvažavajući činjenicu da u dvo-komponentnom reakciono-difuzionom modelu to nije moguće, zaključeno je da je unutrašnja struktura pražnjenja mnogo kompleksnija nego što se to do sada mislilo. Fizičko objašnjenje leži u činjenici da se sistem sa globalnom negativno-diferencijalnom provodljivošću, usled efekata prostornog naelektrisanja u gasnom delu sistema, ne može predstaviti kao sistem sa lokalnom negativno-diferencijalnom provodljivošću. Longitudinalna dimenzija sistema igra važnu ulogu i efektivni 2D modeli nisu adekvatni za naš sistem. To je nametnulo potrebu da se sistematski izvede i alternativni, redukovani model sistema. Pronadjen je primer u kome su oscilacije prisutne čak i sa pozitivno-diferencijalnom provodljivošću strujno-naponske karakteristike (Poglavlje 7), što je u potpunoj suprotnosti sa reakciono-difuzionim modelom koji zahteva negativno-diferencijalnu provodljivost. Takvi rezultati, za prostorno homogena

i vremenski oscilatorna rešenja, se mogu primeniti za bilo koja gasna pražnjenja koja funkcionišu u rednoj vezi otpornika sa paralelnim kondenzatorom. Rezultati prikazani u Poglavlju 7 su bazirani na [91], izuzev dela koji se odnosi na postojanje oscilacija pri globalnoj pozitivno-diferencijalnoj provodljivosti, koji još nisu objavljeni.

### **Prostorno-vremenski oblici luminiscencija**

Prethodni sistem se sada istražuje u dve prostorne dimenzije, tako da se jedna transverzalna prostorna dimenzija dodaje na prethodno istraživani longitudinalni pravac. Stoga se analiza stabilnosti stacionarnog stanja proširuje Fourierovim modom sa transverzalnim talasnim vektorom  $k$ . Rezultirajuća disperziona kriva određuje da li će se, posle promena iz homogenog i stacionarnog stanja, formirati prostorno homogeni ili prostorno strukturirani oblici. Zadržavajući isti režim parametara, kao i u prethodnim istraživanjima, pronadjeno je da se mogu očekivati jedino čista Hopf bifurkacija (razdvajanje) ili Turing-Hopf bifurkacija. Jedan od primera Turing-Hopf bifurkacija je detaljno istražen. Paralelno sa tim istraživanjem, numerički je rešen gasno-poluprovodnički sistem u dve dimenzije, uz korišćenje diskretizacione metode konačnih zapremina. Deo preliminarnih rezultata je predstavljen i oni se slažu sa rezultatima analize stabilnosti u okviru njene validnosti. Dalji razvoj prostorno-vremenskih struktura je doveo do novih dinamičkih svojstava. Interesantno je da se numerička rešenja mogu povezati sa eksperimentalno uočenom pojavom trepćućih filamenata u gasu. Povrh svega, pronadjeno je da je talasna dužina takvih prostornih struktura direktno proporcionalna talasnoj dužini eksperimentalne 'trakaste' strukture [12]. Izloženi rezultati se nalaze u Poglavlju 8 i u pripremi su za publikovanje.





# Acknowledgments

I am indebted to many people who helped me in one way or another during these four and a half years, and made the completion of this thesis possible.

Let's start from the very beginning of this journey.

First of all, I would like to thank my supervisor Ute Ebert for offering me this position and for helping me with all administration and difficulties I encountered at the very beginning. On a more scientific level, I thank Ute for introducing me to a completely different field of physics, for a close guidance and for all the time she devoted to me. It was an honor for me to be her first Ph.D student, and an experience for both of us.

Dr. Ismail Rafatov also deserves my deepest gratitude, since without him I most probably wouldn't have any of these nice color figures (i.e., any numerical results) in the last chapter. I really appreciate all his experience in programming and commitment to work.

Furthermore, I would like to thank prof.dr. H.-G. Purwins for giving us the opportunity to see all experiments and to dr. C. Strümpel for giving us all experimental parameters and his thesis as a valuable source of information.

Due to the effort of the reading committee, this thesis has been greatly improved. I am really grateful for all advices and constructive comments I've got from Joost van der Mullen, Wim van Saarloos, Willem Hundsdorfer and Willem van de Water. I am sorry if some of their suggestions were not entirely incorporated.

It was a great honor and pleasure to meet and work with prof.dr. Yu.P. Raizer and I am grateful he accepted to be a member of the thesis committee.

Furthermore, I would like to thank Wouter Brok from TUE for all the help, technical tips and careful reading of my thesis.

Also, I am deeply in debt to dr. Alexander Morozov (from Leiden University) for helping me to 'shoot' for the missing branch of eigenvalues.

This research has been carried out at CWI, and I would like to thank all my CWI colleagues for creating a nice and friendly working environment. I enjoyed all lunches, coffee/cookie breaks and discussions we had. To name just Bob, Daniel, Mervyn, Manuel, Willem, Mark, Andrea, Bernard, Natalia, Simona, Nebojša, Rachael, Carolynne, Carlota, Bernadet, Dorina, Macek . . .

Especially, I would like to thank Bernard for being such a great officemate during all this time and for translating the samenvatting for me. Sharing office with Andrea and Bernard at the same time was a unique experience, and I will

never forget our long discussions not just about physics, but about life, universe and everything!

Furthermore, I would like to express my gratitude to:

- Simona, for helping me with Photo Shop 7, i.e., for making the cover.
- FOM for financial support, extension of my contract and opportunity to follow some really interesting courses (e.g., Aspects of Management in Nijenrode).
- My physiotherapist, who literally made the writing of this thesis less painful and therefore possible.
- Francien, for all yoga lessons.
- Lieke Schultze, for correcting my English and advise me about the use of 'the' articles in this thesis.
- My Dejan, for being so patient and supportive during my 'writing' phase and, more concretely, for translating the summary into Serbian.
- Then, my many friends with whom I shared all the good times but also bad times, all the cozy evenings, dinners, crazy parties, movies, concerts, skating or other sport events . . . To Ana, Ksenija, Jorge, Juan, Manuel, Danijela & Dennis, Olja & Hans, Ruben, Chiara, Sunčica, Alex & Andrea, Srdjan, Daan, Misja, Thijs, . . . To everyone who made this four years of my life a rich and colorful experience. And to all my friends who left Amsterdam and then made me sad and made me miss them. Gracias!

Finally, I want to thank my parents and my sister for all their unselfish love and support throughout my whole life, for encouraging me to stay here and finish what I've started even when they really needed me and when all I wanted was to be with them.

Thank you all!

Amsterdam, October 2004.